THREE-DIMENSIONAL STRUCTURES OF FLOWS IN A RIVER BEND: OPEN SURFACE AND ICE-COVERED CONDITION

A Dissertation
Submitted to the Graduate Faculty
of the
North Dakota State University
of Agriculture and Applied Science

By

Berkay Koyuncu

In Partial Fulfillment of the Requirements
for the Degree of
DOCTOR OF PHILOSOPHY

Major Program:
Environmental and Conservation Science

April 2024

Fargo, North Dakota

North Dakota State University

Graduate School

Title

THREE-DIMENSIONAL STRUCTURES OF FLOWS IN A RIVER BEND:
OPEN SURFACE AND ICE-COVERED CONDITION

By

Berkay Koyuncu

The Supervisory Committee certifies that this dissertation complies with North Dakota State University's regulations and meets the accepted standards for the degree of

DOCTOR OF PHILOSOPHY

SUPERVISORY COMMITTEE:

Dr. Trung Le
Chair

Dr. Xuefeng Chu

Dr. Stephanie Day

Dr. Mingao Yuan

Dr. Karen Ryberg

Approved:

04/08/2024
Date

Dr. Craig Stockwell
Department Chair

ABSTRACT

The existence of river ice has a significant role in flow characteristics during the winter and spring seasons. From the onset of freeze-up until the ice cover melts, river ice alters the flow structures, resulting in severe consequences such as ice jams, ice dams, and flash floods in spring. Nonetheless, the hydraulic and hydrologic mechanisms of river ice remain largely unknown due to difficulties of the field scale studies in severe winter seasons. In this work, the impacts of the ice cover on the vertical and cross-sectional velocity profile, secondary flow patterns, and shear velocity are investigated using analytical methods and fieldwork observations as well as the state-of-the-art computational fluid dynamics (large-eddy simulation) model. Results show the presence of river ice alters the secondary flow patterns and may induce double circulation in the thalweg area of natural cross-sections or near vertical channel walls of artificial channels/flumes. Results also indicate that the lateral distribution of the shear velocity is differentiated from the open surface condition as the high shear velocity can be observed near the inner and outer banks in ice-covered conditions. In this work, a numerical method is also developed to estimate the depth-averaged velocity profile based on the cross-section geometry. Model results demonstrate that the numerical method can accurately capture the velocity profile in irregular cross-sections based on fieldwork observations. This method helps to minimize the fieldwork efforts during the winter seasons. The future work will focus on the combined impact of the ice cover and the channel curvature (river bend) on the three-dimensional flow structures under different scenarios including the transitional stage. This work provides insights into the transient dynamics of flows during the freeze-up and breakup periods.

ACKNOWLEDGEMENTS

I would like to thank my advisor, Dr. Trung Bao Le, for his continuous guidance and support since the beginning of my Ph.D. studies at North Dakota State University. I have always admired his dedication and passion regarding our research field.

I also want to thank Dr. Xuefeng Chu, Dr. Stephanie Day, Dr. Karen Ryberg, and Dr. Mingao Yuan for being on my thesis committee, reading through my research, and their willingness to provide useful feedback and suggestions.

I would like to express my gratitude to all faculty members of my program, Environmental and Conservation Science, and my home department, the Department of Civil, Construction, and Environmental Engineering, for their scientific advice and the great courses offered in the division. I also thank the staff of the department for their tremendous help in any paperwork and division activities.

I would like to acknowledge the funding support that made the research presented in this thesis possible: North Dakota Water Resources Research Institute (NDWRRI), ND EPSCOR project FAR0033393 and FAR0035235, and the Center for Computationally Assisted Science and Technology (CCAST) at North Dakota State for providing the computational resources used to perform our work. This work is supported by the NSF CAREER No. 2239799 an allocation (CTS200012) from the Extreme Science and Engineering Discovery Environment (XSEDE).

Last but certainly not least, I would like to express my deepest gratitude to my wife for her bravery in following me here with her unconditional support. I also thank my parents for always encouraging my decision to study in the USA.

DEDICATION

To my wife

and my parents.

TABLE OF CONTENTS

LIST OF TABLES

LIST OF FIGURES

LIST OF ABBREVIATIONS

ADCP	Acoustic Doppler Current Profiler
ADV	Acoustic Doppler Velocimeter
AE	Absolute error
AGU	American Geophysical Union
AR	Aspect ratio
CCAST	Computationally Assisted Science and Technology
CFD	Computational fluid dynamics
CURVIB	Curvilinear immersed boundary
DEM	Digital elevation model
DES	Detached-eddy simulation
DTM	Digital terrain model
FGMRES	Flexible Generalized Minimal Residual
FP	Floodplain of the trapezoidal flume
FV	Fixed vessel
GPS	Global positioning system
GSL	Geological Society, London
HVC	High-velocity core
LES	Large-eddy simulation
LiDAR	Light Detection and Ranging
MC	Main channel of the trapezoidal flume
MV	Moving vessel
NAVD88	North American Vertical Datum
NDSU	North Dakota State University
NDWRRI	North Dakota Water Resources Research Institute
PCHIP	Piecewise cubic Hermite interpolating polynomial

RANS	Reynolds-averaged Navier-Stokes
RMSE	Root mean square error
SAT	Surface air temperature
SKM	Shiono and Knight model
SNR	Signal-to-noise ratio
TKE	Turbulent kinetic energy
USGS	United States Geological Survey
UTM	Universal Transverse Mercator
VFS	Virtual flow simulator

LIST OF SYMBOLS

A	Area (m^2)
B	Channel width
b	Semi-width of the main channel
C	Speed of sound
C_1, C_2, C_3, C_4	Empirical coefficients
C_a	Heat transfer coefficient from snow to air (W/m^2)
C_f	Drag coefficient
C_w	Heat transfer coefficient from water to ice (W/m^2)
e	Euler's constant (2.718,281,828)
f_d	Comprehensive Darcy-Weisbach friction factor
f_s	Frequency of sound
f'	Doppler shift
g	Gravitational acceleration
H	Local flow depth (m)
H_o	Water depth under open surface condition (m)
H_c	Averaged water depth under ice-covered condition (m)
h_i	Ice layer thickness (m)
h_s	Snow thickness (m)
K	Secondary flow coefficient
K_s	Coefficient of the surface insulation
k_s	Roughness length (m)
k_{sb}	Bed roughness length (m)
k_{si}	Ice roughness length (m)
L	Length of the simulation domain (m)
L_0	Length of the laboratory flume (m)

ℓ	Distance from the left bank (m)
M	Number of the vertical line
m	Slope of the best-fit regression line
N	Number of the cross-section
n	Mixing turbulent intensity
n_i	Manning roughness coefficient of the ice cover
n_b	Manning roughness coefficient of the channel bed
P	Wetted perimeter
Q	Flow rate (m^3/s)
R	Hydraulic radius (m)
R^2	Coefficient of determination
Re	Reynolds number
Re_τ	Friction Reynolds number
S_0	Channel bed slope
S_f	Total number of freezing days
T	Total measurement duration (s)
t	Time (s)
t_i	Ice thickness with slush ice deposits (m)
T_0	Flow-through time (s)
T_a	Air temperature ($^\circ C$)
T_m	Basal ice temperature ($^\circ C$)
T_w	Water temperature ($^\circ C$)
U	Streamwise time-averaged velocity component ($\mathrm{m\,s^{-1}}$)
U_∞	Long-term depth-averaged velocity ($\mathrm{m\,s^{-1}}$)
U_d	Local depth-averaged velocity ($\mathrm{m\,s^{-1}}$)
u	Local time-averaged velocity ($\mathrm{m\,s^{-1}}$)
u_1	Lateral velocity component of time-averaged velocity ($\mathrm{m\,s^{-1}}$)

u_1	Streamwise velocity component of time-averaged velocity ($\mathrm{m\,s^{-1}}$)
u_3	Vertical velocity component of time-averaged velocity ($\mathrm{m\,s^{-1}}$)
u^+	Dimensionless velocity in wall units
u_∞	Long-term time-averaged velocity ($\mathrm{m\,s^{-1}}$)
u_E	East velocity component ($\mathrm{m\,s^{-1}}$)
u_{max}	Maximum time-averaged velocity along the depth ($\mathrm{m\,s^{-1}}$)
u_N	North velocity component ($\mathrm{m\,s^{-1}}$)
u_p	Primary flow velocity ($\mathrm{m\,s^{-1}}$)
u_s	Secondary flow velocity ($\mathrm{m\,s^{-1}}$)
u_{up}	Vertical velocity component ($\mathrm{m\,s^{-1}}$)
$u^\star$	Shear velocity ($\mathrm{m\,s^{-1}}$)
$u_b^\star$	Bed shear velocity ($\mathrm{m\,s^{-1}}$)
$u_i^\star$	Ice shear velocity ($\mathrm{m\,s^{-1}}$)
$\overline{U}$	Bulk velocity ($\mathrm{m\,s^{-1}}$)
V	Lateral time-averaged velocity component
V_r	Relative velocity
v	Velocity ($\mathrm{m\,s^{-1}}$)
W	Vertical time-averaged velocity component
x	Streamwise direction coordinate
y	Lateral direction coordinate
z	Vertical direction coordinate
z_0	Estimated roughness length based on logarithmic law of the wall (m)
z_b	Bed elevation (m)
z_{max}	Location of the maximum time-averaged velocity along the depth (m)
α	Interim parameter in quartic solution

χ_b	Dimensionless wetted perimeter of the bed
χ_d	Total dimensionless wetted perimeter
χ_i	Dimensionless wetted perimeter of the ice
Δ	Grid spacing
δ_b	Measured thickness of the logarithmic layer near the bed
δ_i	Measured thickness of the logarithmic layer near the ice
δ_{theory}	Theoretical thickness of the logarithmic layer
γ	Intercept of the best-fit regression line
$\overline{\epsilon_{yx}}$	The depth-averaged eddy viscosity
ρ_i	Density of the ice (kg/m^3)
ρ	Water density (kg/m^3)
λ	Dimensionless parameter in quartic solution ($\frac{u_i^\star}{u_b^\star}$)
λ_d	Dimensionless eddy viscosity
λ_i	Latent heat of the ice (J kg^{-1})
λ_w	Wavelength
κ	Von Karman constant
η	Scaled relative distance
η_c	Zero shear stress plane location along the scaled relative distance
η_{max}	Maximum local velocity location along the scaled relative distance
ν	Fluid viscosity
ω	The angle between U and x-axis
τ	Shear stress
τ_b	Bed shear stress
τ_d	Bed Reynolds shear stress
τ_i	Ice shear stress
τ_{yx}	Reynolds shear stress with respect to horizontal plane

τ_{zx}	Reynolds shear stress with respect to vertical plane
$\overline{\tau_{yx}}$	Depth-averaged transverse Reynolds shear stress
Φ	Angle between the relative velocity vector ADV-scatterer line
$\phi(,\lambda)$	Velocity profile function
θ	The angle between u and x-axis
ξ	Local flow depth on the side slope of the trapezoidal channel

1. INTRODUCTION

1.1. Overview of river ice

The existence of river ice with the decreasing air temperatures is the most obvious sign of the coming winter in northern regions. At first, the transition of the river surface from open water to the ice-covered condition may seem relatively trivial; however, river ice has impacts in many aspects including societal and financial. Most of the societal implications can be considered as positive consequences. For instance, smooth and competent ice cover provides outdoor activities (i.e. skating, fishing), natural ice roads on the rivers contribute to more efficient transportation, and a strong ice cover can even serve as a platform for off-shore construction sites (Wazney, 2019). Despite the many positive aspects, some several drawbacks regarding the river ice must be mentioned. Ice covers can make ship transportation impossible without the use of icebreakers. Ice also can cause damage stress on hydraulic structures such as culverts, piers, and dams. In addition, it is known that the river ice negatively impacts hydroelectric operations and limits electricity generation by reducing the channel conveyance. However, the most significant consequence of river ice is the occurrence of ice jams which may cause severe floods by rapidly raising the water elevation during the melting season. Financially, damages from spring floods can be quite costly. According to Yang et al. (2020), the cost of total damage was about 300 million USD in 2017 in only North America. The situation is similar in the Red River of the North (Red River of North Dakota and Minnesota). The most common disaster in this area is the spring flooding due to frequent ice jams and a high amount of snowmelt. One of the most severe events in near history occurred in 1997, which caused approximately 2 billion USD damage (PIELKE JR,

1999) in North Dakota and Minnesota. Under changing climatic conditions (Serinaldi & Kilsby, 2015), more frequent flood events are expected to appear in the future. Therefore, flood modeling and detailed analysis must be carried out to understand the potential damage in this type of region. On the other hand, ice coverage is a factor that can complicate the investigation of the flood in the area. Since the breakup of the ice cover may lead to ice jams and ice dam formations and could cause flooding events, monitoring the river surface becomes essential in river management and disaster mitigation studies. Although spring floods are disruptive to humans, their ecologically beneficial role in the sense of fresh water, sediment, and nutrition distribution to the riparian system should not be neglected. Accordingly, understanding the formation and the dynamics of river ice becomes essential to predict and mitigate the negative consequences.

Apart from the safety issues, it is known that the ice cover alters the local flow structures (Beltaos, 2000). The existence of an ice cover on a natural stream regulates many features of the river flow. For example, velocity distribution along the vertical and horizontal profiles, secondary flow patterns, and shear velocity distributions may drastically differ under the ice cover in comparison to the open surface case condition (Yang et al., 2020). Moreover, further hydraulic processes such as sediment transport, river morphology, biochemical exchanges, and aquatic diversity will be affected (Beltaos & Prowse, 2009). Hence, any change in duration or formation of river ice will have a potential impact on not only the financial aspect but also on environmental sustainability. Consequently, many discussions have risen on international arenas such as "Intergovernmental Panel on Climate Change" (Anisimov, 2007; Anisimov et al., 2001; Salinger et al., 1995), and "Arctic Climate Impact Assessment" (Walsh et al., 2011; Wrona et al., 2006) to express the related concerns.

Some early reviews regarding the potential impact of climate change and global warming in cold regions are that the conditions will not simply improve, furthermore, they will even worsen. Warmer climatic conditions, therefore, a shorter period of river ice, may reduce the financial damages caused by spring floods; however, aquatic life may suffer in such cases (Beltaos & Prowse, 2009).

The duration of the river ice depends on many factors and plays a significant role in the severity of the possible spring floods. Many studies have been conducted during the last four decades to investigate the impact of global warming on this matter (Arnell, 1999; Beltaos & Prowse, 2001; Jones, 1999; Němec & Schaake, 1982; Yang et al., 2020). Generally, the main focus of the related research is the seasonality of the flow and river flow regimes under the impact of different climatic conditions, except for Yang et al. (2020). The main reason behind this is the extremely limited knowledge of the global extent and the change of river ice, despite its wide-ranging importance. A study on the river history in the Northern Hemisphere showed that 56% of all rivers are affected by the river ice using $0°C$ surface air temperature (SAT) isotherm as a proxy (Bennett & Prowse, 2010). Other researchers focused on the duration of the river ice and found that the freeze-up stage occurs 5.7 days later per 100 years and breakup happens 6.3 days earlier per 100 years (Magnuson et al., 2000). Providing consistent data is challenging in global scale studies due to instrument differences, definitions of phenological dates, and analysis periods. Accordingly, most of the prediction studies of river ice are based on ice-SAT relationships derived from in situ records at the regional scale (Yang et al., 2020).

Many factors influence river transitions from open surface to an ice-covered condition. Meteorological conditions determine the temperature change of water, moreover, together with hydraulic conditions, cause and define the ice formation. In the following sections, major processes of the river ice occurrence, their various impacts on flow dynamics, and the main objectives of this study are summarized.

1.1.1. Mechanism of ice formation and ice types

Typically, river ice season in cold regions is defined as freeze-up during the fall and breakup during the spring seasons (Beltaos & Prowse, 2009). The formation of wide-scale river ice initiates once the water temperature is below the freezing point. Shallow streams generally begin to freeze before deeper and larger rivers (Beltaos & Prowse, 2009). However, there are many other ice formation processes such as the anchor ice (see Figure 1.2), which is usually formed under the currents or stream flow when super-cooled pieces of frazil ice stick together and stick to the bottom forming a bottom layer of ice. This type of ice is frequently formed in streams and rivers when water is supercooled, moreover, it can also be seen in lakes (E. W. Kempema et al., 2001). However, ice-cover formation, presence, and breakup in alluvial channels are generally not well understood and not well documented. Beginning from the formation of ice, during the frozen surface, transitional stage, and until the meltdown is complete, river ice has various unknown impacts on flow structures, such as channel-thalweg adjustment, which is a barely recognized concept. Comprehending the details of the impacts mentioned above is crucial to forecast potential consequences on residential areas, aquatic habitats, and morphological changes.

1.1.1.1. Freeze-up

The process of the formation, development, and deterioration of ice in a river is different from that of lakes. The main reason behind this difference is the non-negligible flow velocity and high fluid turbulence of the rivers. The decrease in water temperature is the first stimulation for ice formation. Except for the slow-moving and shallow parts of the flow, fluid turbulence, accordingly, water temperature, is well mixed throughout the depth. When the water temperature super-cools to a few one-hundredths of a degree below $0°C$, tiny ice particles, termed "frazil ice", start to form. The shape of the frazil ice is categorized as small discs; however, needle shapes are documented in the literature as well. Since they are small (a few mm in diameter), they can easily be kept in suspension by strong fluid turbulence. On the other hand, the river ice formation may differ according to the features of the channel geometry. Near the banks and islands, where the flow depth is quite shallow and the velocity is usually less than $0.1m/s$, ice particles form a continuous layer of skim ice on the water surface. This type of ice cover is termed "border ice". The border ice isolates the water underneath and prevents/decelerates further super-cooling of the flow.

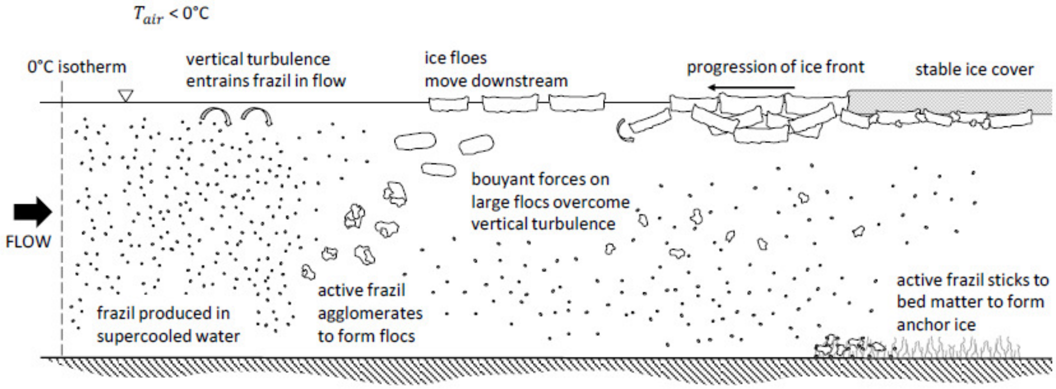

Figure 1.1. Formation of the river ice during the freeze-up stage and visualization of effective buoyant forces (Wazney, 2019).

Afterward, frazil ice particles start to accumulate and flocculate by their adhesive nature to create "frazil slush". As this slush can be shredded by the turbulence, it also can float to the water surface in case buoyant forces overcome the fluid turbulence that keeps them in suspension (see Figure 1.1). Frazil slush starts to accumulate on the surface and forms a surface crust called "frazil pans". Naturally, floating frazil pans may freeze with each other or border ice while moving downstream with the flow. This process continues until the surface concentration reaches $80 - 90\%$.

The ice cover has two boundaries: (1) ice-atmosphere, and (2) ice-water boundaries. Ice growth rate depends on the heat exchange at both boundaries as follows:

$$\frac{dh_i}{dt}\rho_i\lambda_i p_i = \left(\frac{T_m - T_a}{\frac{h_i}{k_i} + \frac{h_s}{k_s} + \frac{1}{C_a}}\right) - C_w(T_w - T_m) \tag{1.1}$$

where, t is time, h_i is ice thickness; h_s is snow thickness (m); ρ_i is the density of the ice (kg/m^3); λ_i is the latent heat of the ice (J/kg); k_i and k_s are the thermal conductivities of ice and snow; T_a, T_m and T_w are water, basal ice ($T_m = 0°C$), and water temperatures; and finally, C_a (snow to air) and C_w (water to ice) are the heat transfer coefficients (W/m^2). It is possible to predict ice thickness using Stefan formula (Beltaos & Prowse, 2009):

$$h_i = K_s\sqrt{S_F} \tag{1.2}$$

where S_F total number of freezing days with below $0°C$ and K_s is a coefficient describing the surface insulation.

At this point, ice formation takes the shape of a bridge between both banks (bridging stage), and accumulates incoming smaller ice floes. On the other hand, if the flow velocity is high enough, incoming ice pieces may swipe and stick to the underside of the ice cover (hydraulic thickening). This phenomenon continues until the accumulated ice sufficiently thickens to cause a backwater effect, increase the upstream water level and decrease the flow velocity (Hicks, 2009). As many other ice types may occur during the freeze-up stage based on the geological features of the river (i.e. aufeis where groundwater emerges at the surface or ice disks where centrifugal forces are applied), it is still quite difficult to follow and examine the procedure due to extremely dangerous field conditions.

The water level is significant in addressing the impact of river ice accurately. The flow velocity is lower under the existence of ice cover due to additional hydraulic resistance the ice cover implements. According to this relationship:

$$\frac{H_c}{H_o} = [1 + (\frac{n_i}{n_b})^{3/2}]^{2/5} + 0.92\frac{t_i}{H_o} \tag{1.3}$$

where, n_i and n_b are Manning roughness coefficients of the ice cover underside and channel bed, respectively; t_i is the ice thickness (different than h_i when there are slush ice deposits); H_o is the water depth (obtained under open surface condition according to the flow rate); H_c is the average water depth under the ice-covered condition. The case $n_i = 0$ and $t_i = 0$ stands for open surface condition, where $H_c > H_o$. The difference $H_c - H_o$ is defined as *backwater* and it can be large depending on the ice type.

1.1.1.2. Breakup

The nature of breakup on a reach can vary from one in which the ice gradually deteriorates and more-or-less melts in place, to one in which breakup occurs suddenly due to the passage of a dynamic breakup front while the ice is still strong. The breakup period is a force balance-based procedure driven by many factors such as air temperature, flow rate, and channel morphology. To start the river-ice breakup, driving forces must dominate the resisting forces. Dramatic changes in both forces may occur during the breakup that can affect the final breakup. The most significant boost in driving forces is the increase in river discharge due to the snowmelt. Although the breakup is a spring event, the exact time of it remains undetectable due to a complex suite of hydrometeorological conditions. These conditions are categorized as (1) thermal (overmature), and (2) dynamic (premature) (Beltaos & Prowse, 2009).

Thermal breakup is defined as gradual melting in place due to temperature warming. On the other hand, the dynamic breakup is explained as a sudden cracking while the ice is still strong. While the thermal breakup slightly increases the water level, dynamic breakup tends to cause spring floods with extreme water level increases. Initiation of the dynamic breakup is associated with snowmelt, accordingly, the water level increases. Increased water level creates stress on the underside of the ice cover and leads to cracks which will release the ice from the shorelines. Freed ice body starts flowing downstream which is known as "ice clearing". Naturally, ice bodies are massive in the beginning and willing to be stuck if they encounter a new geometric constraint or a still-fixed ice formation. This phenomenon is called "ice jams". Hence, ice jams may occur during both freeze-up and breakup transitional stages. Depending on the case, ice jams often extend up to many kilometers along the stream and can reach several meters in thickness. Accordingly, accumulated water starts to rise behind the jam and results in flooding in the area (Hicks, 2009). Ice jam floods are often considered the greatest danger of river ice (Ashton, 1986). Prowse and Beltaos (Prowse, 2001b) cited several extreme spring flood events caused by ice jams and indicated that their recurrence intervals are higher than open-water floods.

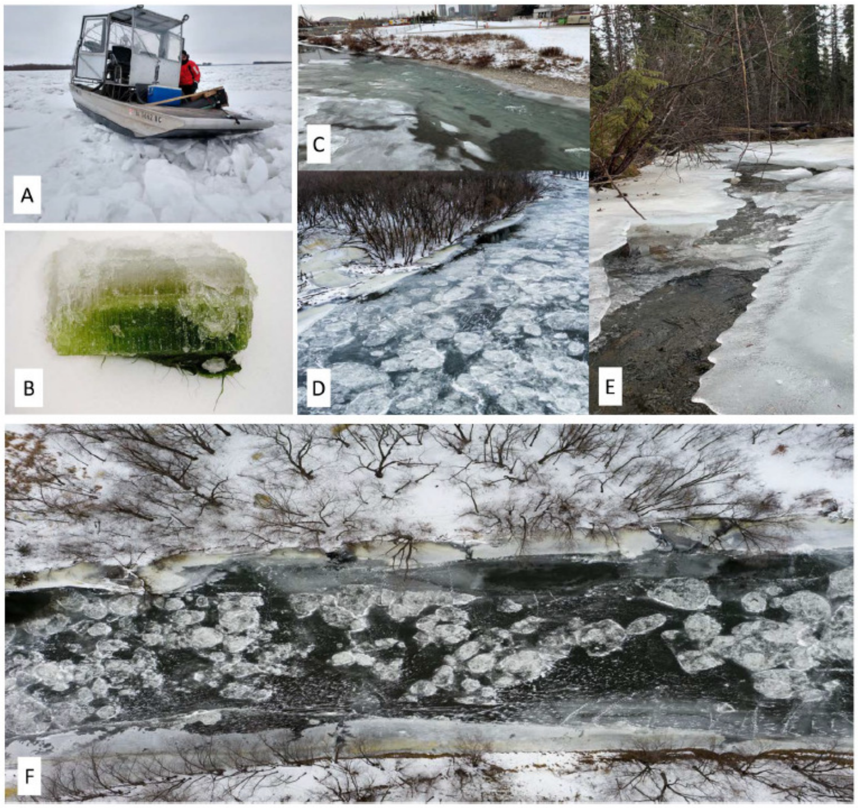

Figure 1.2. Common river ice formations. (A) Ice jam (Upper Mississippi River near Bellevue, Iowa), (B) surface ice covered with algae (Upper Mississippi River, La Crosse, Wisconsin, (C) anchor ice (Elbow River, Calgary, Alberta, Canada), (D) frazil ice merging with surface ice (Rum River, Anoka, Minnesota, (E) suspended ice (Plante Creek, Obed, Alberta, Canada), (F) planform view of lateral variation in Rum River (Thellman et al., 2021).

1.1.2. Flow measurement techniques under ice-covered and open surface conditions

Flow measurements are usually conducted by two types of instruments: (1) Acoustic Doppler Velocimeter (ADV), and (2) Acoustic Doppler Current Profiler (ADCP). ADV is an instrument based on the Doppler effect. As the concept works based on the number of sound waves passing at a point in time, t, the Doppler shift is defined as follows:

$$f' = f_s(V_r/C) \tag{1.4}$$

where f' is the Doppler shift, f_s is the frequency of sound (source and receiver are both stationary), V_r is the relative velocity between source and receiver, and C is the speed of sound, given as:

$$C = f\lambda_w \tag{1.5}$$

where f is frequency and λ_w is the wavelength. ADV works with the same principle. The transducer sends sound at a fixed frequency and receives the echoes which are reflected to the instrument. The ADV relies on the assumption that these scatterers (any kind of obstacle such as particles or plankton) move at the same velocity as the water. Since the ADV transmits and receives the sound waves, the Doppler shift is doubled as follows:

$$f' = 2f_s(V_r/C) \tag{1.6}$$

Despite the angular motion change, the distance between the source and transducer remains same during the measurement; therefore, the equation 1.10 becomes:

$$f' = 2f_s(V_r/C)\cos\Phi \tag{1.7}$$

where Φ is the angle between the relative velocity vector and the line between the ADV and scatterers.

As displayed in Figure 1.3, reflected sound waves are measured by the receiving probes. An ADV estimates the three velocity components (in x, y, and z direction) using the changes in the frequency of the reflected signals. Based on the current speed, different ADVs are designed with various signal frequencies. ADVs are popular, especially in laboratory flume studies, and are particularly useful when characterizing turbulence. However, due to the installment problems, ADVs tend to be deployed in shallow streams.

Figure 1.3. 10 MHz Sontek ADV (Neill & Hashemi, 2018).

An ADCP emits sound waves of a known frequency that reflect off suspended, moving particles in the water column and return to the ADCP. The ADCP measures the shift in frequency caused by the Doppler effect to calculate how fast the particle and, therefore, the water is moving.

Similar to the ADV, an ADCP emits sound waves of a known frequency that reflect off a scatterer in the water column. The ADCP, then, receives the returned signals and uses the Doppler effect to calculate how fast the particle, therefore, water moves. ADCPs are more advantageous in deeper flows and functional even in oceans. They are usually deployed hull-mounted to look downwards through the water column. Since the ADCP is specifically designed to record instantaneous location, the ship's movement can be corrected using the bottom tracking (or the ship's GPS). In more detail, the main advantage of deploying an

ADCP is its ability to build a transect or a series of transects over time. On the other hand, the form of data collection is not reliable for either (a) estimation of vertical velocity component (unless it is significant), or (b) estimating turbulence properties. Hence, standard error analysis methods are not suggested for ADCP observations since they can tolerate the turbulence impact (Petrie et al., 2013).

Figure 1.4. Hydroboard-mounted ADCP, Sontek M9, during the Fall measurements of 2020.

Typically, an ADCP uses 3 to 5 beams to calculate velocity throughout the water column (vertical profile) (Neill & Hashemi, 2018). In the case of keeping it stabilized, ADCP can be used in stationary deployment techniques as well. The measurement capabilities of ADCP instruments vary with frequency. For instance, while the devices with lower frequency can penetrate 100 s of meters, high-frequency devices are limited to only a couple of meters (Sontek M9 can penetrate up to 30m). The most significant limitation of the ADCP is the signal interference issue. Therefore, it is difficult to obtain observations near the boundaries, including the channel bed and ice cover.

Bathymetry and cross-sectional measurements require a moving technique to cover more area in less amount of time. In this matter, ADCP is more advantageous in comparison to the other measurement techniques due to its moving capability. The ADCP sensor is attached to the Hydroboard and/or motorboat to move in the interest area. Frequency and the bin size of the ADCP (i.e., $1MHz$ and $0.06m$ for Sontek M9) are significant parameters while moving the boat and processing the collected data. For instance, Sontek M9 collects data every second and this frequency can become an issue if the boat is moved quickly.

According to the purpose, ADCP can be used in the stationary mode under both open surfaces (see Figure 1.4) and ice-covered conditions (see Figure 1.5). The most significant detail is to keep the device stable if it is used under open surface conditions. To provide a stationary measurement, the motion of the boat must be tracked and the statistical insignificance of the movement must be proved statistically (Petrie et al., 2013). However, this issue becomes a problem if the boat cannot be stabilized by using land-fixed tools (rope, rod, etc.). In case of stabilization by a land-fixed tool, the motion should remain within 1 m^2 (unless the current is too strong), therefore, it can be considered as a station. On the other hand, ADV is a more accurate instrument while a stationary measurement is in progress. In the case of using ADV under open surface conditions, a land-fixed structure is required since it lacks a Hydroboard. Moreover, ADV requires more sensitive and longer position stabilization. A framework needs to be built between banks to provide sensitivity. On the other hand, there will not be any concern regarding the boat's motion in the ice-covered condition. In such a case, an ice hole must be opened and the sensor needs to be placed in the water. ADV can be used in the same manner as ADCP under ice-covered conditions.

Conducting a field survey during winter seasons tends to be difficult and dangerous. Since the frozen rivers are usually in severely cold regions, air temperature constitutes the most problematic obstacle for the team members and equipment. Low air temperature instantly freezes the equipment after taking it out of the water for the next ice hole. If the ice cannot be perfectly removed from the sensor surface, oscillation increases in the following station. Low air temperature also limits outdoor work hours despite the protective outfits. The other problem is the safety issue while working on ice. Usually, the ice thickness is sufficiently thick during the measurement period (typically January and February in North Dakota) and provides a safe working environment on the ice. According to our measurements, minimum ice thickness is observed as $0.75ft$ near the banks. Ausable River Association suggests at least $0.5ft$ ice thickness to work on ice with equipment. However, working on ice still requires attention and precaution since a thinner spot may occur at unexpected locations.

Figure 1.5. Stationary measurement technique with Trung Le (left) and Berkay Koyuncu (right) during the 2021 winter season (Feb/21).

1.1.3. Vertical velocity profile and shear velocity

Distribution of the velocity along the depth is one of the most basic and significant flow characteristics in alluvial channels. It has been known since the beginning of the 1880s, that maximum velocity in open channel flows occurs just below the water surface (Yan et al.,

2011) (Figure 1.6a). Many field-scale and laboratory experiments on velocity distribution validated the profile in Figure 1.6a and contributed to the development of discharge calculation techniques based on that profile such as the velocity-area method (Vyas et al., 2021). On the other hand, the profile under the ice-covered condition was discovered much later due to an inadequate laboratory environment and the unavailability of fieldwork equipment. With more opportunities in the 20^{th} century, comparing open surface and ice-covered flow with similar magnitude became possible in laboratory environment (Lau & Krishnappan, 1985; B. T. Smith & Ettema, 1995; Tsai & Ettema, 1996). Numerous experimental studies and a few field scale studies showed that the vertical velocity distribution provides a more symmetrical shape due to a greater wetted perimeter with the existence of ice cover resulting in increased friction and flow resistance. Hence, the flow velocities are slower in comparison to the open surface condition. However, some laboratory experiments showed that the maximum velocity can be higher under the ice-covered condition in cases where the ice cover is thick and fixed to the banks. Nevertheless, little or no empirical data exist on the turbulent and time-averaged properties of flow beneath a cover of ice in natural streams (A. Sukhodolov et al., 1999).

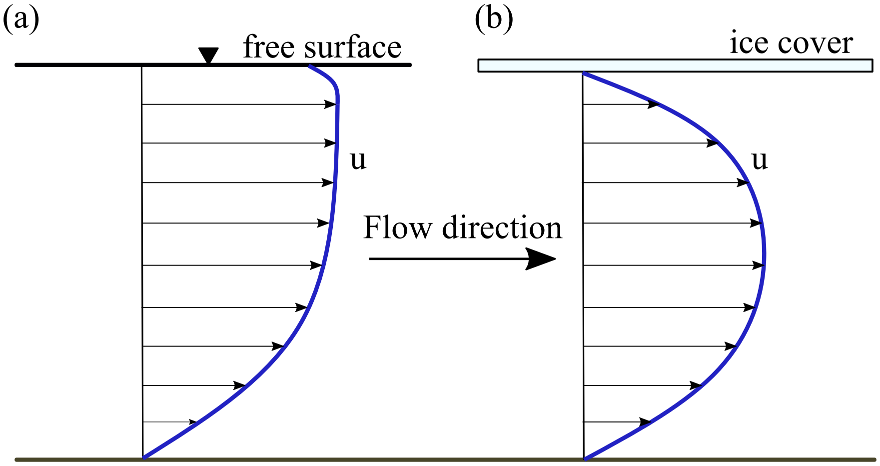

Figure 1.6. Distribution of the vertical velocity under (a) free surface condition, and (b) ice-covered condition.

Bed shear stress τ is a significant parameter in geophysical and environmental engineering applications. Since it relates to scour and morphological changes in alluvial channels, this fundamental variable needs to be categorized as a turbulence scaling parameter. As bed shear stress is a hydrodynamic force applied to channel sediment, determination of it is essential to estimate critical erosion and deposition thresholds, and erosion and deposition rates (Bagherimiyab & Lemmin, 2013). Thus, shear stress estimation strongly affects the accuracy of sediment transport rate calculations. Under the assumptions of two-dimensional and uniform flow, shear velocity can often be estimated as follows:

$$u^{\star} = \sqrt{gRS_0} \tag{1.8}$$

where g is the gravitational acceleration, R is the hydraulic radius, and S_0 is the bed slope. However, this method provides a rough estimation and is not sufficient to evaluate the flow characteristics.

In alluvial channels, a vertical velocity profile with elevation above the bed is often used to estimate bed shear stress; therefore bed shear velocity (Ashworth & Ferguson, 1986; P. M. Biron et al., 1998; J. S. Bridge & Jarvis, 1976; Petit, 1990). Using the von Karman-Prandtl vertical velocity distribution, also known as the "logarithmic law of the wall", velocity can be represented as a logarithm of height as follows:

$$u = \frac{u^{\star}}{\kappa} \ln \frac{z}{k_s} \tag{1.9}$$

where u is the point velocity (time-averaged velocity) in streamwise direction at the corresponding elevation from the channel bed, κ is von Karman's constant ($0.39 < K < 0.41$), and $u^{\star}$ is the shear velocity, and k_s is the roughness length of the channel bed. Accordingly, bed shear stress (τ_b) can be computed as follows:

$$\tau_b = \rho u^{\star 2} \tag{1.10}$$

Even though there are more recent methods to estimate shear velocity and shear stress based on the Reynolds shear stresses from turbulence measurements (P. Biron et al., 1993; Heathershaw, 1979; Williams et al., 1989), the logarithmic law of the wall allows for average shear stress near the boundaries without sophisticated high-frequency instruments (P. M. Biron et al., 1998). On the other hand, this method is considered problematic, particularly in shallow water environments. The main reason behind this issue is the signal interference issue, mentioned in section 1.3, related to the instrument limitations (Ferguson & Ashworth, 1992; Robert et al., 1992). Hence, it is challenging to obtain a sufficient number of velocity measurements in the logarithmic layer, the boundary layer where the logarithmic law of the wall applies. Many studies have investigated the thickness of the logarithmic layer. Results indicated that the thickness can extend from 15% (J. S. Bridge & Jarvis, 1977; J. Bridge & Jarvis, 1982) of the flow depth through 50% (Ferguson & Ashworth, 1992). Due to the fitting methodology and measurement height selection, the thickness of the logarithmic layer is difficult to generalize.

1.1.4. Secondary flow structures

The evolution of meandering rivers has still an incomplete understanding of long-term scale dynamics such as repeated changes of channel patterns in different environments. This is particularly the case where rivers are potentially ice-covered for some years (Lotsari et al., 2017). Investigations show that the river ice influences the relationship between flow and channel morphology, especially for channels that convey substantial sediment-transporting flow during winter. Studies to investigate the impact of ice are predominantly based on laboratory experiments since the beginning of the twentieth century (Lau & Krishnappan, 1985; B. T. Smith & Ettema, 1995; Tsai & Ettema, 1994a; Urroz & Ettema, 1994a). Many studies (Krishnappan, 1984; B. T. Smith & Ettema, 1995) have compared the open surface case with the ice-covered case using similar flow rates to comprehend the difference.

Secondary flow and helical patterns caused by meandering bends under open surface conditions. It is widely acknowledged that the secondary currents and helical flow patterns can be dominant with the curvature effect (Lotsari et al., 2017). With the channel curvature, flow gravitates towards the outer bank by centrifugal acceleration (Dietrich & Smith, 1984). This change also causes a water level difference between the outer bank (higher) and inner bank (lower) which leads to a pressure difference. Accordingly, flow is directed towards the inner bank due to this pressure difference, and single helical flow circulation occurs during the free surface condition (Tsai & Ettema, 1996).

The secondary flow is a more complicated and sensitive concept under ice-covered conditions. The existence of ice cover affects the vertical lateral variation of the flow during the frozen season, especially in curved bends. Unfortunately, studies conducted in ice-covered straight channels could not fully explain the flow in curved channels (Demers et al., 2011; Urroz & Ettema, 1994a). On the other hand, a double helical flow pattern is evident near the thalweg area. The first helical cell close to the river bed is similar to the one under open surface conditions; however, the second helical cell near the ice cover is different from the open surface case (Urroz & Ettema, 1994b). Nevertheless, the aforementioned findings are either from a laboratory experiment or conducted using outdated measurement equipment. Hence, there is a lack of field scale-based studies performed in subarctic river environments (Lotsari et al., 2017).

Only two recent studies have used the newest Acoustic Doppler Current Profiler (ADCP) for studying winter flow in a small natural meandering river (Demers et al., 2011; Demers et al., 2013). Demers et al. (2011) (Demers et al., 2011) studied the underneath ice flow characteristics in one meander bend of a sandy Canadian river by drilling 38 holes at 16 cross-sections for ADCP measurements during two consecutive winters. Demers et al. (2011) was the first to observe two stacked counter-rotating helical flow cells in a natural, i.e., outside the laboratory, ice-covered meander bend of a small river. Around the apex, the top and bottom-layer flows were directed in the opposite direction to the maximum velocities occurring in the middle-flow layers. This behavior was similar to results from flume studies (Urroz & Ettema, 1994a). Demers et al. (2011) stated that the high-speed flow occurring at mid-depths of the water column is deflected towards the outer bend by centrifugal acceleration, but that the flume studies had oversimplified the process. In addition, the two helical cells develop into one when progressing downstream owing to flow mixing and morphological nonuniformity (Demers et al., 2011). New monitoring approaches, such as the ADCP survey, were needed to enable this type of field study in ice-covered rivers. Despite their advanced study in ice-covered river conditions, Demers et al. (Demers et al., 2011) concluded that it would be important to study the wintertime flow from a larger number of measurement locations and consecutive meander bends of a small river.

1.1.5. Numerical simulation approach

The challenges in field measurements as well as the limitations of laboratory experiments have led to many efforts in studying river ice using simulations with one-dimensional (1D) unsteady flow models (H. T. Shen et al., 1995) and two-dimensional (2D) hydrodynamic simulations (Lotsari et al., 2019). While one (Lindenschmidt, 2017) and two-dimensional simulations (Brayall & Hicks, 2012; Kolerski, 2014) are computationally expedient and can incorporate large-scale hydro-climatic condition easily (H. T. Shen, 2010), they cannot provide secondary flow structure near bends (Lotsari et al., 2019). It is desirable to obtain the three-dimensional flow structures under ice coverage (Turcotte et al., 2011) since they have a close relationship with sediment transport processes. Advanced turbulent modeling such as Detached Eddy Simulation (DES) and large-Eddy Simulation (LES) has been widely used for river flows (Constantinescu et al., 2013; Constantinescu et al., 2011; Koken et al., 2013; Le et al., 2019).

With the integration of numerical simulation to river modeling, arbitrary complex bathymetry and embedded in-stream structures have arisen as a challenge (Kang et al., 2011). The numerical simulation models such as LES and RANS were able to solve the flow only over the simpler topographical conditions (Van Balen, Uijttewaal, & Blanckaert, 2010). Kang et al. (2011) have integrated the curvilinear immersed boundary (CURVIB) method, developed by Ge and Sotiropoulos (2007) (Ge & Sotiropoulos, 2007), to solve the three-dimensional flow structures near the boundaries. Hence, this development provided benefit to many studies on river modeling over complex topographies (Le et al., 2019) and sediment transport (Khosronejad & Sotiropoulos, 2014; Khosronejad et al., 2011, 2015). On the other hand, all the efforts so far were conducted by considering the free-surface condition. To our knowledge, there have been no attempts to use such advanced models to investigate the three-dimensional flow structure of icy flows in rivers.

The virtual flow simulator (VFS) is a significant open-source code and it uses the CURVIB method to reconstruct velocity boundary conditions (Le et al., 2019). Since the VFS is capable of simulating multi-physics/multi-phase flows with advanced turbulence models (LES) over complex terrains (https://safl-cfd-lab.github.io/VFS-Wind/), many laboratory experiments (Kang & Sotiropoulos, 2011, 2012a, 2012b; Kang et al., 2016; Khosronejad & Sotiropoulos, 2014; Khosronejad et al., 2011) have extensively validated it for both fixed and live bed.

1.1.6. Goals and objectives

The goal of this Ph.D. thesis is to study the impact of ice coverage on the three-dimensional flow characteristics of a river bend. The main objectives are explained below:

- **Objective 1: Depth-averaged velocity models under the ice cover**
  - *Task 1.1:* Perform large-eddy simulations for ice-covered conditions by adapting the laboratory conditions of F. Wang et al. (2020).

  - *Task 1.2:* Validate the LES results using the laboratory observations (F. Wang et al., 2020) and determine the mechanisms leading to the changes in the secondary flow structures under ice coverage.
  - *Task 1.3:* Compute the depth-averaged velocity profile using the analytical and numerically approximated SKM-based method for the straight laboratory channel.
  - *Task 1.4:* Utilize and test the numerically approximated SKM-based method for irregular cross-sections monitored during the field surveys on the Red River.
- **Objective 2: Morphological characteristics of a bend of the Red River**
  - *Task 2.1:* Conduct field surveys to measure the bathymetry of the Red River in downtown Fargo, North Dakota, United States.
  - *Task 2.2:* Perform data processing for bathymetry (river) and combine with high-resolution LiDAR data (land) to create a Digital Terrain Model (DTM) of the study area.
  - *Task 2.3:* Spatial analysis of the morphological change (cross-sections) along the river bend using the DTM with the help of software Tecplot and Paraview.
- **Objective 3: Field measurements of flow structures under ice-free condition**
  - *Task 3.1:* Conduct field surveys for depth-averaged velocity in the study area under ice-free condition.
  - *Task 3.2:* Investigate the cross-stream distribution of the vertical velocity profiles under open-surface condition. Examine the validity of the logarithmic law for ice-free condition.

  - *Task 3.3:* Examine the effect of flow discharge on the secondary flow pattern at the bend apex.
  - *Task 3.4:* Reexamine the available methodologies for computing bed shear stress. Evaluate the cross-stream distribution of bed shear stress.
- **Objective 4: Field measurements of icy flows under full coverage**
  - *Task 4.1:* Conduct field surveys to provide data under ice-covered conditions in 2020, 2021, 2022, and 2023.
  - *Task 4.2:* Examine the validity of the quartic profile (Guo, 2017; Guo et al., 2017) of the velocity distribution for ice-covered flows.
  - *Task 4.3:* Reconstruct the secondary flow pattern under different ice-covered conditions (2021, 2022).
  - *Task 4.4:* Reexamine the use of logarithmic law to derive the bed shear stress under ice-covered conditions. Test the accuracy of the quartic profile in estimating the bed shear stress.
- **Objective 5: Modeling shear stress distribution in ice-covered river flows**
  - *Task 5.1:* Develop a theoretical model based on the momentum balance and identify the parameters.
  - *Task 5.2:* Perform field measurements to validate the developed model
  - *Task 5.3:* Propose further applications of the developed model for estimating the bed shear stress under the ice cover.

In the first step, understanding the ice-covered flow dynamics is required to initiate an expectation based on the features of the channel. For example, according to the bend curvature, channel morphology, flow rate, and ice type, flow structures can be hypothesized if their impacts are well understood. To achieve this task, many measurements need to be conducted under ice-covered and open surface conditions. Second, channel flow needs to be modeled by replicating the actual conditions (i.e., bed roughness, ice roughness, channel bathymetry). Validation of the model is necessary to identify and discuss the three-dimensional flow structures such as secondary flow patterns, shear velocity, and high-velocity core. Eventually, a successful model validation increases the accuracy of prediction and mitigation of the consequences under different scenarios. Minimizing the threat to human life and reducing the financial cost of the damage are the ultimate benefits this study desires to present.

1.1.7. Organization of the thesis

Chapter 1 explains the significance of river ice, freeze-up and breakup processes, flow measurement methodologies, and impacts of ice cover on three-dimensional flow structures. Objectives and main goals are also explained in the first chapter.

Chapter 2 is focused on the computation of the lateral distribution of the depth-averaged velocity models under ice-covered conditions. I propose an SKM-based numerical method, perform large-eddy simulations, and validate the results with previously performed laboratory measurements. Validated simulation results are used to visualize secondary flow characteristics and turbulence statistics under the full-covered flow conditions. I finally utilize the proposed method for irregular cross-sections using our field surveys of the Red River in Fargo, ND.

Chapter 3 of this proposal presents the data monitoring and processing to understand the impact of ice on a field scale. Conventional logarithmic law of the wall method is employed to investigate velocity profile and shear velocity for the field scale ice-covered data for the first time, and results are compared with the recently developed experiment-based quartic solution method. Moreover, the classical rotation-based Rozovskii method is implemented to visualize secondary flow structures under the open surface and ice-covered conditions. This chapter is submitted to "Water Resources Research", a peer-reviewed scientific journal published by the American Geophysical Union (AGU), with the title "On the impacts of ice cover on flow profiles in a bend".

Chapter 4 proposes a new theoretical model to analyze shear velocity using cross-stream momentum under ice-covered conditions. The derivation of the model and its performance in comparison to the existing analytical methods are presented. This chapter is published in "Special Publications" of the Geological Society, London (GSL) with the title of "Modeling Shear Stress Distribution in Ice-Covered Streams".

2. ON THE DEPTH-AVERAGED MODELS OF ICE-COVERED FLOWS [1]

2.1. Abstract

The existence of ice cover in alluvial channels has a significant impact on regulating depth-averaged profiles and thus plays an important role in morphological processes. However, this impact is largely unknown under field conditions. In this work, a novel numerical method to compute depth-averaged profiles of ice-covered flows is proposed based on the Shiono-Knight approach. The proposed model is then validated with laboratory data, an analytical solution, and large-eddy simulation. Finally, the method is applied to infer depth-averaged profiles in the Red River. The proposed method demonstrates its robustness in replicating the measured profiles. The proposed method provides a reliable way to estimate the friction factor and secondary flow's strength for ice-covered flows in alluvial channels.

2.2. Introduction

2.2.1. Background

In regions with freezing temperatures, ice cover is periodically observed in natural and artificial channels (Kirillin et al., 2012; F. Wang, Huai, Guo, & Liu, 2021; F. Wang et al., 2020). However, the effects of the frozen surface on flow dynamics remain poorly understood (Ettema, 2002; Teal et al., 1994; Tsai & Ettema, 1996), particularly in alluvial streams (Ettema & Daly, 2004). Previous studies (Lotsari et al., 2017, 2022) suggest that the frozen surface acts as an additional roughness boundary and leads to an increase in flow complexity by facilitating the interaction between the flow and the channel's bed. The

---

[1] The content of this chapter was co-authored by Berkay Koyuncu, Lahcen Akerkouch, and Trung Le. Koyuncu was the main analyst and writer. Akerkouch assisted with the development of the depth-averaged model. Le provided feedback and served as a proofreader.

resulting dynamics lead to changes in the three-dimensional flow structures, which might have important consequences in alluvial processes (F. Wang, Huai, & Guo, 2021). The duration of coverage of river ice has recently been reported to decrease in the Northern Hemisphere (Yang et al., 2020) due to the impacts of climate change. Hence, studying flow dynamics in ice-covered channels will address the gap in knowledge of river flows in cold regions, which have been mostly studied under open-surface conditions.

On the contrary to the open-surface condition, the vertical velocity profile follows a two-layer structure (two-layer hypothesis) (Guo et al., 2017; Lau & Krishnappan, 1981) in ice-covered flows: (1) the upper ice layer, and (2) the lower bed layer (F. Wang et al., 2020; Y. Zhong et al., 2019). These layers are separated by the zero shear stress plane (Lau & Krishnappan, 1981; Parthasarathy & Muste, 1994). In practice, the maximum velocity plane was also shown to be close to the separation plane (Guo et al., 2017; P. Larsen, 1973; Teal et al., 1994) and thus it could also be used to monitor the separation of these layers as well. The location of the maximum velocity plane is sensitive to the ice and bed roughness and it generally tends to approach the smoother boundary (Tatinclaux & Gogus, 1983). A correct distribution of resistance accurately divides the water column into layers as Einstein's treatment method (Einstein, 1942) suggests, moreover, the average velocity of all sections is assumed to be equal to the depth-averaged velocity of the water column. Hence, a comprehensive roughness analysis is a key factor for computing velocity profiles (P. A. Larsen, 1969; Y. Zhong et al., 2019).

Estimating the depth-averaged velocity in ice-covered flows is crucial for many hydraulic applications (K. Smith et al., 2023; Teal et al., 1994; Zhang et al., 2021). Depth-averaged velocity is influenced by various factors (Sun & Shiono, 2009), including ice cover properties, channel geometry, and flow discharge. Laboratory experiments (E. Kempema et al., 1993; Teal et al., 1994; Urroz & Ettema, 1994a; F. Wang et al., 2020) are generally used to estimate the impacts of these factors on the depth-averaged velocity profiles. While these laboratory efforts provide the basic knowledge of hydraulic engineering applications (Y. Zhong et al., 2019), depth-averaged profiles at field scales have not been examined in detail (Koyuncu & Le, 2021; Koyuncu & Le, 2022; Lotsari et al., 2017, 2022). The analytical framework for studying depth-averaged profile and its dependence on the secondary flow patterns are discussed below.

2.2.2. Analytical models for ice-covered flows

One of the most popular methods for computing the depth-averaged velocity is the Shiono-Knight model (SKM) (Shiono & Knight, 1988), which was developed based on the two-dimensional Reynolds Averaged Navier-Stokes (RANS) equations (Pu, 2019) for a straight channel with fully-developed turbulent flows. The SKM was later improved by Shiono and Knight, 1991 with the integration of secondary currents coefficient (K) and adapted for curved channels (Tang & Knight, 2015).

The RANS equations can be combined and reduced to Shiono and Knight, 1991:

$$\rho\left[\frac{\partial UV}{\partial y}+\frac{\partial UW}{\partial z}\right]=\rho g S_0+\frac{\partial \tau_{yx}}{\partial y}+\frac{\partial \tau_{zx}}{\partial z} \tag{2.1}$$

where ρ is the water density; U, V, and W are the time-averaged velocity components in x (streamwise), y (lateral/transverse), and z (vertical) directions, respectively; τ_{yx} and τ_{zx} are the Reynolds shear stresses with respect to the horizontal and vertical planes, respectively.

The above momentum equation can be solved analytically for the depth-averaged profile $U_d(y) = \frac{1}{H}\int_0^H U(y)dz$ if the shape of the cross-section is precisely known.

In ice-covered channels, F. Wang et al., 2020 suggests that Equation 2.1 can be integrated along the depth (H) as:

$$\rho\frac{\partial(H(UV)_d)}{\partial y} = \rho g H S_0 + \frac{\partial(H\overline{\tau_{yx}})}{\partial y} - \chi_d \tau_d \tag{2.2}$$

It is required that the resistance of the ice layer is reflected by the parameter χ_d, which is the total dimensionless wetted perimeter of the river bed (χ_b) and the ice cover (χ_i) per unit width ($\chi_d = \chi_b + \chi_i$); $\overline{\tau_{yx}}$ and τ_d are the depth-averaged transverse and bed Reynolds shear stresses; g is the gravitational acceleration. S_0 is the channel bed slope.

Application of eddy viscosity assumption leads this term to be expressed as follows:

$$\overline{\tau_{yx}} = \rho\overline{\epsilon_{yx}}\frac{\partial U_d}{\partial y} \tag{2.3}$$

where $\overline{\epsilon_{yx}}$ is the depth-averaged eddy viscosity. Invoking the definition of the bed shear stress and the eddy viscosity assumption, we have:

$$\overline{\epsilon_{yx}} = \lambda_d u^\star H = \lambda_d H U_d\sqrt{\frac{f_d}{8}} \tag{2.4}$$

$$\tau_d = C_f \rho U_d^2 = \rho U_d^2 \frac{f_d}{8} \tag{2.5}$$

C_f and f_d are the drag coefficient and the comprehensive Darcy-Weisbach friction factor, respectively. λ_d is the dimensionless eddy viscosity; $u^\star$ is the shear velocity; τ_d is the comprehensive shear stress. The impact of the secondary flow was introduced to this relationship

(Ervine et al., 2000; F. Wang et al., 2020) as the secondary flow coefficient (K) (Ervine et al., 2000): $(UV)_d = KU_d^2$. Hence, the depth-averaged form of the governing equation can be derived as follows:

$$\rho g H S_0 - \rho \frac{f_d}{8} \chi_d U_d^2 + \frac{\partial}{\partial y}(\rho \lambda_d H^2 \sqrt{\frac{f_d}{8}} U_d \frac{\partial U_d}{\partial y}) = \frac{\partial(\rho H K U_d^2)}{\partial y} \tag{2.6}$$

This equation can be solved analytically to estimate U_d in special cases as discussed below.

For symmetrically trapezoidal channels (see Figure 2.1b), F. Wang et al., 2020 proposes that Equation 2.6 can be solved analytically by dividing the cross-section into three distinct zones with known side slopes ($1 : s$): (1) flood plain ($s = \infty$); (2) the side slope ($s = 1$); and (3) the main channel ($s = \infty$). It is required that wall boundary conditions applied on both sides of the channel ($y = 0$ and $y = B = 1\ m$) as $U(y = 0) = 0$ and $U(y = B = 1\ m) = 0$. As the channel geometry is symmetrical with the total width of B, the mid-boundary condition is needed ($y = \frac{B}{2}$) where the maximum velocity U_{max} occurs. Using these boundary conditions, Equation 2.6 can be solved for one-half of the channel's cross-section.

U_d is computed for the main channel and the flood plain (constant flow depth- $s = \infty$) using:

$$U_d = \sqrt{C_1 e^{r_1 (y - \frac{B}{2})} + C_2 e^{r_2 (y - \frac{B}{2})} + \omega} \tag{2.7}$$

where r_1, r_2, and ω are the coefficients; and C_1 and C_2 are the case-specific unknown constants. The values of C_1 and C_2 are not known in advance and must be calculated by fitting to the observational data. Other coefficients can be calculated as:

$$r_1 = \frac{1}{\lambda_d H}\left(\frac{8}{f_d}\right)^{1/2}\left(K + \sqrt{K^2 + 2\lambda_d \chi_d \left(\frac{f_d}{8}\right)^{3/2}}\right)$$

$$r_2 = \frac{2K}{\lambda_d H}\left(\frac{8}{f_d}\right)^{1/2} - r_1 \tag{2.8}$$

$$\omega = \frac{8gHS_0}{f_d \chi_d}$$

For $s = 1$ (side slopes), the analytical solution for U_d is given as:

$$U_d = \sqrt{C_3 \xi^{\alpha_1} + C_4 \xi^{\alpha_2} + \mathcal{A}\xi} \tag{2.9}$$

where C_3 and C_4 are the unknown constants that depend on the case setup; ξ presents the local flow depth on the side slope length of the trapezoid ($\xi = H - (y - \frac{B}{2} - b)/s$). Here, b is the semi-width of the main channel (see Figure 2.1). The coefficients (α_1, α_2, and $\mathcal{A}$) of this equation are calculated as:

$$\alpha_1 = \frac{\mathcal{L} - M + \sqrt{(M - \mathcal{L})^2 - 4N\mathcal{L}}}{2\mathcal{L}}$$

$$\alpha_2 = \frac{\mathcal{L} - M - \sqrt{(M - \mathcal{L})^2 - 4N\mathcal{L}}}{2\mathcal{L}} \tag{2.10}$$

$$\mathcal{A} = -\frac{gS_0}{\frac{\lambda_d}{s^2}\left(\frac{f_d}{8}\right)^{1/2} + \frac{2K}{s} - \frac{f_d}{8}\chi_d}$$

The parameters $\mathcal{L}$, M, and N are calculated as: $\mathcal{L} = \frac{\lambda_d}{2s^2}\left(\frac{f_d}{8}\right)^{1/2}$, $M = \frac{\lambda_d}{2s^2}\left(\frac{f_d}{8}\right)^{1/2} + \frac{K}{s}$, $N = \frac{K}{s} - \frac{f_d}{8}\chi_d$.

As shown above, the analytical solution is only available if the side slope s is a constant value (Y. Zhong et al., 2019). Therefore, it is impossible to apply this analytical method to compute U_d with arbitrary cross-sections.

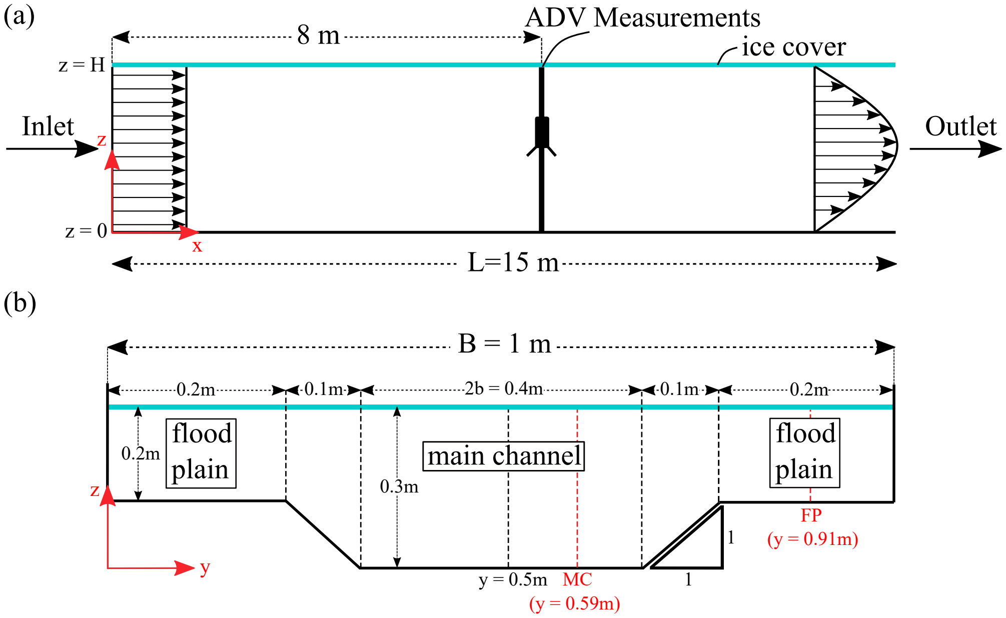

Figure 2.1. Dimensions of the laboratory flume in F. Wang et al., 2020. (a) The side view of the flume shows the location of the measured plane. The domain length $L = 15m$; (b) the cross-sectional sketch shows the locations of the measured data in the main channel (MC) and the floodplain (FP) verticals. The channel center is represented with a black dash line at $y = 0.5\ m$. Here, b and H are the semi-width of the cross-section and the flow depth, respectively.

2.2.3. Numerical simulations for ice-covered flows

The need to estimate U_d in field conditions has led to the use of one-dimensional (Lindenschmidt, 2017; H. T. Shen et al., 1995) or two-dimensional (Lotsari et al., 2019; H. T. Shen et al., 2000) models to capture large-scale hydrodynamic patterns in rivers. These models (Brayall & Hicks, 2012; Kolerski, 2014; Lindenschmidt, 2017) are computationally expedient and can incorporate large-scale hydro-climatic condition easily (H. T. Shen, 2010). However, they cannot provide details on the turbulent characteristics (Lotsari et al., 2019) in a cross-section. Recent advancements in Computational Fluid Dynamics (CFD) have enabled three-dimensional modeling of river flows (Le et al., 2018; Van Balen, Uijttewaal, & Blanckaert, 2010). These CFD models use advanced turbulence models such as large-eddy simulation (LES) and Reynolds-averaged Navier-Stokes (RANS) equations (Khosronejad et al., 2016). To date, LES was mostly performed under open-surface condition (Le et al., 2018).

2.2.4. Study objectives

Natural rivers and streams feature irregular cross-sectional shapes (Devi & Khatua, 2020), which prohibit the use of analytical solution such as Equation 2.7 and 2.9 for ice-covered flows. It is necessary to develop and validate a general method for computing depth-averaged flows in arbitrary cross-section. This study aims to develop such a general method using numerical approximation. The main objectives are:

- Develop a procedure to compute depth-averaged profile U_d (a numerical solution to Equation 2.1) in compound channels with arbitrary geometries.
- Validate the proposed numerical procedure with laboratory, analytical solution, and field data.
- Identify the key factors regulating the profile, especially the impact of secondary flows.
- Investigate the sensitivity of the U_d solution to the governing parameters (f_d, λ_d, and K).

First, a numerical procedure to determine U_d is developed for compound channels using the SKM-based method of (F. Wang et al., 2020). Second, large-eddy simulation (LES) is also performed and compared with experimental data in a straight channel in the experiment of F. Wang et al., 2020 to provide a complete three-dimensional flow field to serve as the validation data. Third, the proposed numerical procedure is validated using the available data of experiments of F. Wang et al., 2020 and the obtained LES results. Finally, the validated procedure is used to investigate the range of the governing parameters (f_d, λ_d, and K) in a river reach of the Red River, United States, to examine its applicability for field conditions.

2.3. Methodology

2.3.1. Laboratory data

The experimental setup for ice-covered flows is performed by F. Wang et al., 2020. The experiment is performed on a $L_0 = 12\ m$ long (x -streamwise), $B = 1\ m$ (y - lateral), and the total depth $H = 0.3\ m$ (z - depth) in a straight/trapezoidal flume (Figure 2.1(a)) with fully-covered condition (see Figure 2.1(b)).

A whole foam piece is used to mimic the full coverage of the ice layer. The channel bed slope was $S_0 = 0.01\%$ and the side slope (1: s) of the trapezoid was $s = 1$. The flow depth is 0.3 m and 0.2 m on the main channel and the flood plain, respectively. The flow discharge is $Q = 0.0510\ m^3/s$. The monitoring cross-section is chosen at a distance of 8 m from the inlet as shown in Figure 2.1(a). As the channel is symmetrical, flow measurements (Acoustic Doppler Velocimetry) are only obtained starting from the channel center and towards the right wall along the cross-stream direction ($y \geq 0.5m$).

In the experiments of F. Wang et al., 2020, the roughness length of the surface cover (foam - k_{si}) and channel bed (organic glass - k_{sb}) are not reported. As these roughness values are important for velocity profiles, the logarithmic fitting (Petrie & Diplas, 2016) is used to determine their values as follows:

$$\frac{U(z)}{u_\star} = \frac{1}{\kappa} \ln \frac{z}{k_s} + 8.5$$

$$u^\star = \kappa m \tag{2.11}$$

$$k_s = exp[8.5\kappa - \frac{\gamma}{m}]$$

where $U(z)$ is the local streamwise velocity at depth z ($0 < z < H$); κ is the Von Karman constant ($0.39 < \kappa < 0.41$) (P. M. Biron et al., 1998; Marusic et al., 2013; Petrie & Diplas, 2016; Petrie et al., 2013); k_s is the roughness length of the surface; $u^\star$ is the shear velocity of the surface (either the bed ($u_b^\star$) or the ice ($u_i^\star$)); and γ and m are the intercept point and the slope of the best-fit regression line, respectively.

Since the vertical velocity profiles are measured on the flood plain (FP) and the main channel (MC) separately by F. Wang et al., 2020, the roughness lengths (k_{si} and k_{sb}) can be estimated by fitting Equation 2.11 to find the appropriate values of m, and γ. As seen in Table 2.1, the fitting method yields similar values for the bed k_{sb} ($\approx 0.00535\ m$). However, different values k_{si} are found in the FP and MC regions $k_{si} = 0.00026 - 0.00091\ m$. It is thus necessary to investigate the impact of k_{si} on the flow profile. The values of the roughness length are used as inputs for the large-eddy simulations as described below.

Table 2.1. The fitted values of k_s for foam and glass in the main channel (MC) and floodplain (FP) verticals using the experimental data of F. Wang et al., 2020.

Material	Roughness Length, k_s (m)
Foam (from MC)	0.00091
Foam (from FP)	0.00026
Glass (from MC)	0.00490
Glass (from FP)	0.00570

2.3.2. Large-eddy simulation (LES) of flows in the trapezoidal channel

A series of LES is carried out to determine the three-dimensional flow structure in the trapezoidal channel (Figure 2.1). The open-source code Virtual Flow Simulator (VFS) is used to simulate the turbulent flows to replicate the experimental configuration of F. Wang et al., 2020. The VFS code has been validated with laboratory experiments under both fixed bed and live bed cases (Khosronejad et al., 2012, 2013). The numerical code has exhibited its efficiency and accuracy in capturing flow dynamics in open-surface conditions (Kang & Sotiropoulos, 2011; Kang et al., 2011; Khosronejad et al., 2012). In this context, we provide a concise overview of the adopted numerical techniques.

The filtered incompressible Navier-Stokes equations are solved using a fractional step method in a structured grid domain. The momentum equation is tackled using an implicit approach with a matrix-free Newton–Krylov solver (Calderer et al., 2015). The Poisson equation is solved using FGMRES with multi-grid preconditioner with Petsc numerical library (Kang & Sotiropoulos, 2011; Kang et al., 2011; Le et al., 2018). The channel surface is represented as an immersed surface inside the computational domain (Kang & Sotiropoulos, 2011). The wall boundary condition is then reconstructed at the immersed nodes using the roughness length k_s. For the details of the numerical methods, the reader is encouraged to review the related works (Kang & Sotiropoulos, 2011; Khosronejad et al., 2013; Le et al., 2018).

To examine the impacts of the roughness length k_s on the flow profiles, numerical simulations are performed using different roughness lengths. Initially, the bed (glass) roughness and the foam (ice) roughness are set to be $k_{sb} = 0.00535\ m$ and $k_{si} = 0.00059\ m$, respectively. These values are chosen as the averaged roughness of glass (bed) and foam (ice) in Table 2.1. Subsequently, the values of k_{si} and k_{sb} are systematically varied as $k_{sb} = 0.00535\ m - 0.00600\ m$ and $k_{si} = 0.00059\ m - 0.00800\ m$. The computational grid is a structured grid, which is from $1.3M$ (Grid-1) to $10.0M$ (Grid-3) as shown in Table 2.2. The grid spacing (Δ) is chosen to be fine enough so that the assumption on the logarithmic law of the wall is valid at the immersed node ($\Delta^+ = \frac{\Delta u^\star}{\nu} \leq 1000$). Here ν is the fluid viscosity. The combination of the computational grid, k_{si}, and k_{sb} gives rise to a total of 5 simulation cases as shown in Table 2.3.

Table 2.2. Computational grids for the trapezoidal channel of F. Wang et al., 2020. The value of Δ^+_{max} is estimated using $(\Delta^+)_{max} = \dfrac{max(\Delta x, \Delta y, \Delta z)u_\star}{\nu}$. The shear velocity is $u^\star \approx 0.0054\ m/s$, which is estimated from the measured profile of F. Wang et al., 2020.

Grid name	Size	Δx(m)	Δy(m)	Δz(m)	$(\Delta^+)_{max}$
Grid-1	$251 \times 101 \times 51$	0.0598	0.0099	0.0059	322
Grid-2	$1001 \times 101 \times 51$	0.0150	0.0099	0.0059	81
Grid-3	$1001 \times 101 \times 101$	0.0150	0.0099	0.0030	81

While the flow rate is set exactly as in the experimental value of $Q = 0.0510\ m^3/s$, the flow profile is not reported (F. Wang et al., 2020). Therefore, a uniform flow is assumed at the inlet (see Figure 2.1) with the bulk velocity $\overline{U} = 0.204\ m/s$. At the outlet, a fully developed flow condition is assumed. The flow-through time is defined as $T_0 = \frac{L}{\overline{U}}$. Due to the uncertainty in the inlet flow profile, the length of the simulation domain $L = 15\ m$ is made slightly longer in comparison to the actual channel length L_0 to accommodate the growth of the boundary layer along the computational domain. In all cases, the simulation is first run for a period of $20T_0$ to initiate the turbulent flow along the domain length (L). The time-averaged flow field is then acquired by accumulating the results starting from $t = 20T_0$ to $t = 40T_0$. The turbulent statistics are computed from the accumulated data.

Table 2.3. Computational setup for simulation cases in the trapezoidal channel in Figure 2.1. The combination of the computational grids (Table 2.2), ice roughness (k_{si}), and bed roughness (k_{sb}) give rise to 5 simulation cases.

Case	Grid	k_{si} (m)	k_{sb}(m)
1	Grid-1	0.00059	0.00535
2	Grid-1	0.00091	0.00535
3	Grid-1	0.00800	0.00600
4	Grid-2	0.00059	0.00535
5	Grid-3	0.00590	0.00535

2.3.3. Field measurement

Field surveys during the winter season of 2021 are conducted in a bend of the Red River of the North near Lindenwood Park, Fargo, North Dakota, United States (see Figure 2.2). The channel bed of the Red River is mostly identified as clay and silt (Weiss et al., 2015). Five separate cross-sections are surveyed: I_a (Feb/19/21), I_b (Feb/20/21), I_c (Feb/21/2021), I_d (Feb/21/2021), and I_e (Feb/21/2021). Among these cross-sections, I_a through I_d are separated with 6 m spacing between each other. The cross-section I_e is located right after the bend apex, approximately 310 m away from I_a.

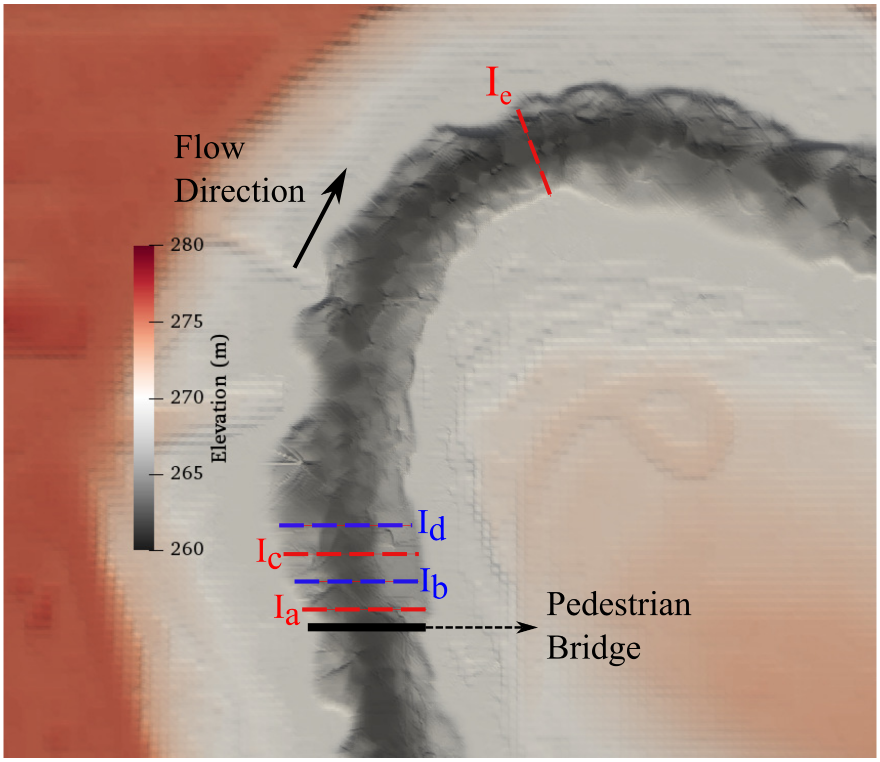

Figure 2.2. The location of the cross-sections in the study area. The river reach of the Red River (North Dakota-Minnesota border, United States) is selected. The Digital Terrain Model is generated from the LiDAR data (North Dakota Water Commission - https://lidar.dwr.nd.gov/ and the surveyed bathymetry data.

The Acoustic Doppler Current Profiler (ADCP), Sontek M9, is used to monitor velocity components at each vertical under the SmartPulse mode of 1 MHz. The reliability of the data sets is confirmed by monitoring the beam separation (signal-to-noise ratio - SNR) of all measurements during and after the acquisitions. To place the sensor below the ice cover, a gas auger is used to open ice holes large enough to lower the M9 into the flows. In each cross-section, the distance from the left bank (the reference point) ℓ is noted for each ice hole (vertical). The measurement period in each ice hole was limited to 120 s due to the impact of low air temperature on the equipment. The details of the number of ice holes in each cross-section are summarized in Table 2.4. The cross-sections and the ice hole locations are shown in Figure 2.3. The wet area of the cross-sections and the wetted perimeter are approximated as $A \approx 120\ m^2$ and $P \approx 95\ m$, respectively. The details of the field campaigns and the data processing can be found in my other works (Koyuncu & Le, 2021; Koyuncu & Le, 2024).

Table 2.4. The summary of the hydrological data at the USGS Fargo (05054000) Station and the number of ice holes in each cross-section.

Case	Q (m^3/s)	Elevation (m)	Total verticals (ice holes)
I_a	12.5	265.92	6
I_b	12.8	265.92	7
I_c	13.8	265.93	7
I_d	13.8	265.93	8
I_e	13.8	265.93	7

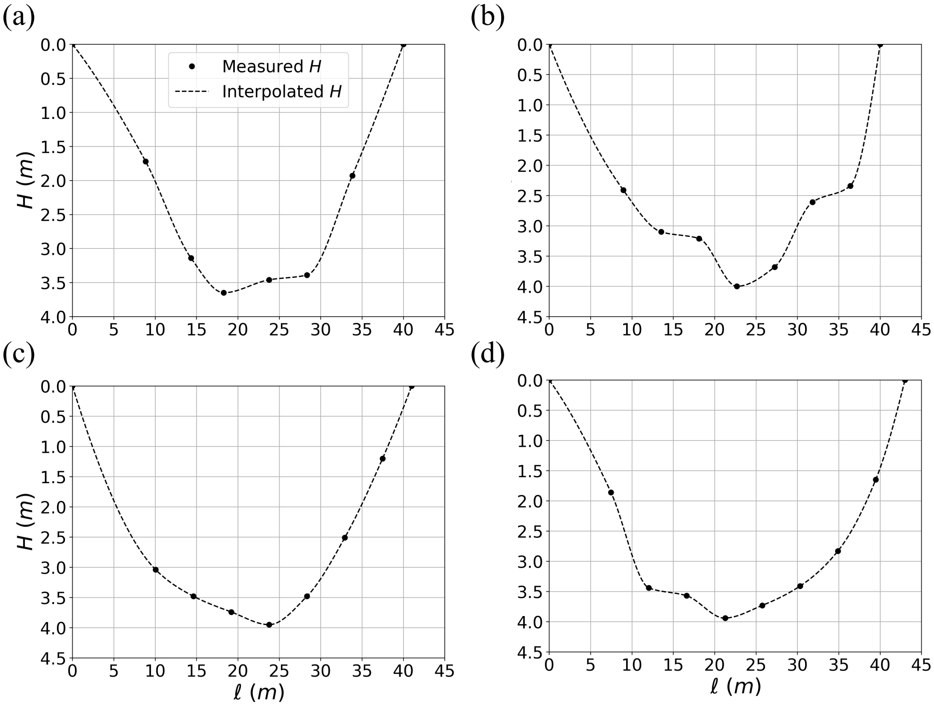

Figure 2.3. The measured flow depth (H) in each ice hole and the reconstructed shapes of the cross-sections using the Piecewise Cubic Hermite Interpolating Polynomial (PCHIP) function for (a) I_a, (b) I_b, (c) I_c, and (d) I_d. The details of the measurements are shown in Table 2.4.

2.4. SKM-based numerical solution for depth-averaged profile in an arbitrary cross-section

2.4.1. Numerical procedure

In this section, a novel algorithm is proposed to solve the momentum equation of the SKM in arbitrary cross-sections. Specifically, the numerical approximation of Equation 2.6 can be explained as follows.

$$\rho g H S_0 - \rho \frac{f_d}{8} \chi_d U_d^2 + \rho \lambda_d \sqrt{\frac{f_d}{8}} \frac{\partial}{\partial y} (H^2 \frac{\partial (U_d^2)}{\partial y}) = \rho K \frac{\partial (H U_d^2)}{\partial y} \tag{2.12}$$

For the tidiness of operations, a notation arrangement is made at this point as $\mathcal{V} = U_d^2$. Following the distribution of derivatives and applying the product rule, the momentum equation becomes:

$$\rho g H S_0 - \rho \frac{f_d}{8} \chi_d \mathcal{V} + \rho \lambda_d \sqrt{\frac{f_d}{8}} (\frac{\partial H^2}{\partial y} \frac{\partial \mathcal{V}}{\partial y} + H^2 \frac{\partial^2 \mathcal{V}}{\partial y^2}) = \rho K (\frac{\partial H}{\partial y} \mathcal{V} + H \frac{\partial \mathcal{V}}{\partial y}) \tag{2.13}$$

Afterward, three-point central differencing (2^{nd} order accurate) is applied for all derivatives assuming a constant spacing between two successive ice holes $i-1$, i, and $i+1$ (spacing Δy).

$$\begin{aligned} \rho g H_i S_0 - \rho \frac{f_d}{8} \chi_d \mathcal{V} + \rho \lambda_d \sqrt{\frac{f_d}{8}} (2 H_i \frac{H_{i+1} - H_{i-1}}{2\Delta y} \frac{\mathcal{V}_{i+1} - \mathcal{V}_{i-1}}{2\Delta y} + H^2 \frac{\mathcal{V}_{i+1} - 2\mathcal{V}_i + \mathcal{V}_{i-1}}{\Delta y^2}) \\ = \rho K (\mathcal{V}_i \frac{H_{i+1} - H_{i-1}}{2\Delta y} + H_i \frac{\mathcal{V}_{i+1} - \mathcal{V}_{i-1}}{2\Delta y}) \end{aligned} \tag{2.14}$$

$$
\begin{aligned}
-\rho\frac{f_d}{8}\chi_d\mathcal{V} + \rho\lambda_d\sqrt{\frac{f_d}{8}}(2H_i\frac{H_{i+1}-H_{i-1}}{2\Delta y}\frac{\mathcal{V}_{i+1}-\mathcal{V}_{i-1}}{2\Delta y} + H^2\frac{\mathcal{V}_{i+1}-2\mathcal{V}_i+\mathcal{V}_{i-1}}{\Delta y^2}) \\
-\rho K(\mathcal{V}_i\frac{H_{i+1}-H_{i-1}}{2\Delta y} + H_i\frac{\mathcal{V}_{i+1}-\mathcal{V}_{i-1}}{2\Delta y}) = -\rho g H_i S_0
\end{aligned}
\tag{2.15}
$$

Here, terms are grouped for the values of $\mathcal{V}$ at three successive ice holes ($i-1$, i, and $i+1$) as follows:

$$
\begin{aligned}
A_i = & \quad -\rho\lambda_d\sqrt{\frac{f_d}{8}}2H_i\frac{H_{i+1}-H_{i-1}}{4\Delta y^2} + \rho\lambda_d\sqrt{\frac{f_d}{8}}\frac{H_i^2}{\Delta y^2} + \rho K\frac{H_i}{2\Delta y} \\
B_i = & \quad -\rho\frac{f_d}{8}\chi_d - \rho\lambda_d\sqrt{\frac{f_d}{8}}\frac{2H_i^2}{\Delta y^2} - \rho K\frac{H_{i+1}-H_{i-1}}{2\Delta y} \\
C_i = & \quad \rho\lambda_d\sqrt{\frac{f_d}{8}}(2H_i\frac{H_{i+1}-H_{i-1}}{4\Delta y^2}) + \rho\lambda_d\sqrt{\frac{f_d}{8}}\frac{H_i^2}{\Delta y^2} - \rho K\frac{H_i}{2\Delta y} \\
D_i = & \quad -\rho g H_i S_0
\end{aligned}
\tag{2.16}
$$

We now need to solve the system of equations $i = 1 \dots N$ (N is the number of ice holes) to find $\mathcal{V}_i$ as:

$$
A_i \times \mathcal{V}_{i-1} + B_i \times \mathcal{V}_i + C_i \times \mathcal{V}_{i+1} = D_i \tag{2.17}
$$

An in-house Matlab script is developed to invert this linear system of equations to find the depth-averaged velocity at each ice hole i^{th} ($U_d^i = \sqrt{\mathcal{V}_i}$). Note that the coefficients A_i, B_i, C_i, and D_i can be determined before ice measurements if the local bathymetry, the ice coverage, and the bed roughness are known. However, it is required to supply the boundary conditions (e.g., known values of U_d at specific locations) to solve Equation 2.17 numerically.

2.4.2. Application considerations

As the natural cross-sections are not symmetrical as in the experimental settings by F. Wang et al., 2020, it is impossible to consider only one-half of the channel. In this case, it is required to reconsider the mid-boundary location that divides the cross-section into two separate parts with the number of ice holes as N_1 and N_2 so that Equation 2.17 can be solved correspondingly for each part. In other words, one value of $U_d^{mid-boundary}$ must be known at one ice hole around the middle part of the channel ($i = mid-boundary$), which is classified as the mid-boundary condition. There is also a need to prescribe the values of $U_d = 0$ at the left bank ($i = 0$) and the right bank ($i = N$). Note that there is no particular requirement on the location of such an ice hole $mid-boundary$ because Equation 2.17 only requires that U_d must be known for the beginning and end points of the part. The steps for the numerical procedure are as follows:

- *Step 1: Measure the depth-averaged velocity and depth at each ice hole from the ADCP data.*
- *Step 2: Build the shape of the cross-section.* To be as practical as possible, we assume that the cross-section is not surveyed in advance and is only known via measurements at the limited number of ice holes. To reconstruct the shape of the cross-section from the depth measurements at each ice hole. The shape of each cross-section is reconstructed using the Piecewise Cubic Hermite Interpolating Polynomial (PCHIP) method from the flow depth in each ice hole.
- *Step 3: Select a number of verticals for computations (N).* Theoretically, the larger the number of N, the obtained numerical values U_d^i will be more accurate.

- *Step 4:* Decide the $mid - boundary$ condition $U_d^{mid-boundary}$ by selecting the ice hole $mid - boundary$. The left (outer bank) and right (inner bank) parts are completely separated by the $mid - boundary$ ice hole.
- *Step 5:* Solve Equation 2.17 separately for the left and right parts by splitting the number of ice holes into $N = N^L + N^R - 1$. Here N_L and N_R are the number of verticals in the left and right parts, respectively. Please note that Equation 2.17 solves both sides independently. Therefore, the choice of N_L and N_R can be varied.
- *Step 6:* Compare the obtained values of U_d^i with the measured data from ADCP.

2.5. Result

2.5.1. Three-dimensional flow structures in the trapezoidal channel

The flow dynamics in the trapezoidal channel is reconstructed from the large-eddy simulation results as shown in Figure 2.4. The changes in the depth-averaged flow profile is monitored along the computational domain in the cross-sections 1, 2, 3, and 4. As there are uncertainties in the value of roughness (k_{si} and k_{sb}) and the inlet flow condition, it is necessary to identify the impacts of these uncertainties to the LES results by comparing the computational results with the experimental data.

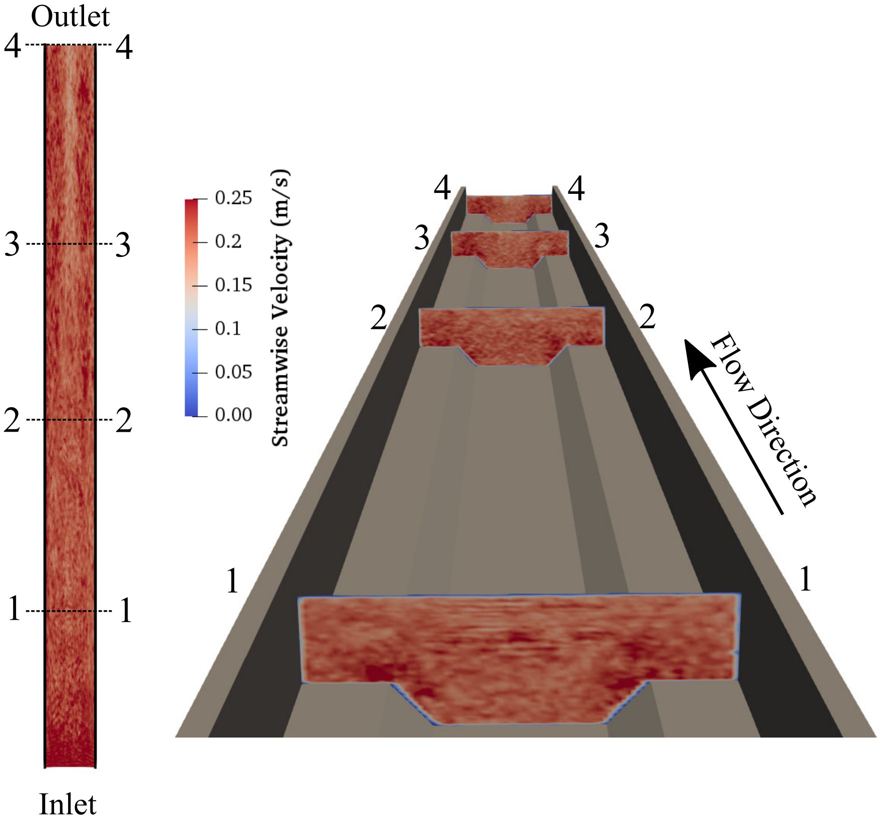

Figure 2.4. A planform (left) and cross-sectional view (right) of the large-eddy simulation setup. Cross-sections 1, 2, 3, and 4 are separated with an equal spacing of 3.75 m. The cross-section 4 corresponds to the outlet plane.

The impact of roughness on the vertical profile of streamwise component ($U(z)$) is investigated by comparing the simulation results of Case 1, 2, and 3 (Table 2.3) using the same computational Grid-1. As shown in Figure 2.5, the main channel and floodplain verticals are 0.3 m and 0.2 m deep (see also Figure 2.1), respectively. Although the values of k_{si} and k_{sb} are varied significantly, the vertical profiles in the main channel and the floodplain remain nearly identical. Thus, the LES results show that the roughness lengths of the ice and the bed does not impact the $U(z)$ significantly in this experimental setup.

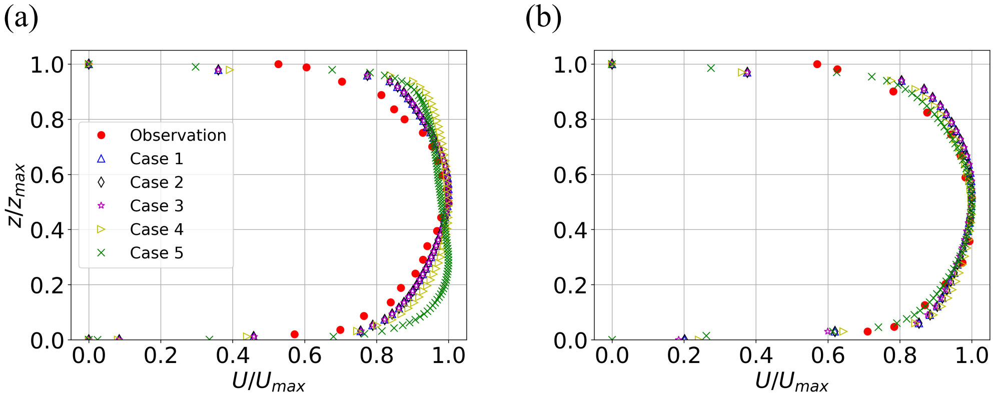

Figure 2.5. The observed and computed (LES) vertical velocity profiles for (a) the main channel vertical (MC, $y = 0.59\ m$), and (b) for the floodplain vertical (FP, $y = 0.91\ m$) at cross-section 4. The exact locations of these verticals are shown in Figure 2.1. The grid computational setups are shown in Table 2.2 and Table 2.3.

The sensitivity of the LES results with the computational grid is shown by comparing results of Case 1 ($1.3M$) and Case 4 ($5.0M$) in Table 2.3. The comparison in Figure 2.5 shows that increasing the number of grid points does affect significantly the profile in the main channel but not the floodplain one. To further examine the combined impact of the computational grid and the roughness, the vertical profiles of Case 1, 4, and 5 are compared. Note that the ice roughness in Case 5 is set to be 0.0059 m, which is one order of magnitude larger than the one of Case 1. It is evident that the results of the finest grid (Grid-3) in Case 5 reflects a deviation from the Case 1 and 4 data near the bed in the main channel. In brief, the vertical profile in the main channel requires the use of sufficiently fine mesh.

The depth-averaged profiles are compared across different grid levels from Grid-1 ($1M$), to Grid-2 ($5M$) and Grid-3 ($10M$) in Case 1, 4, and 5 as shown in Table 2.3. The computed velocity profiles at the cross-section 4 are then compared with the experimental observation of F. Wang et al., 2020. The results show that the computational results generally agree with the experimental observation regardless of the uncertainties in k_{sb} and k_{si}. As the computational grid is refined, the depth-averaged profile follows closely the experimental data, especially the transition from the main channel toward the side slope. The slight decrease over the side slope is captured accurately by all the grid configurations. The result of Grid-3 agrees excellently with the experimental data, especially in the transition over the floodplain and the vicinity of the side wall ($y = B = 1\ m$). Therefore, the grid refinement indicates that the LES is able to reproduce the depth-averaged profiles in the experiment of F. Wang et al., 2020. Since Case 4 has the averaged values of roughness in Table 2.1, its simulation result is used to report the flow dynamics in the subsequent sections.

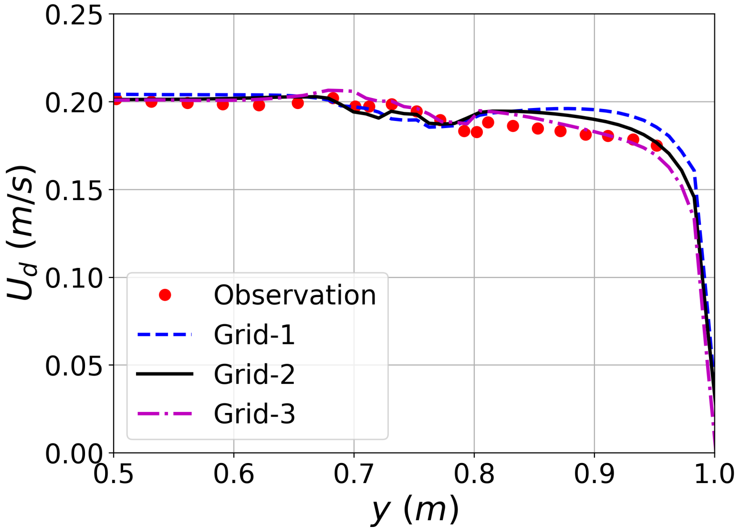

Figure 2.6. Grid refinement study for the distribution of depth-averaged velocity (U_d) in large-eddy simulation (LES) with different grid levels (Grid-1, Grid-2, Grid-3 - see Table 2.2) for case 1, 4, and 5 (see Table 2.3), respectively at cross-section 4 (see Figure 2.4). The computed profiles are also compared with the experimental observation (F. Wang et al., 2020), which is available only on the right side of the trapezoidal channel. The origin ($y = 0.5\ m$) is at the center of the channel.

The dependence of the lateral velocity ($V(z)$) on the computational grid is investigated in Figure 2.7 in two locations: (a) near the channel's center, and (b) on the flood plain for Case 1, 4, and 5. The results show that the value of $V(z)$ varies largely depending on the location of the vertical. In Figure 2.7(a), $V(z)$ is near zero and does not follow a particular pattern near the channel center. However, the distribution of $V(z)$ is completely different in the floodplain vertical with three separate regions as shown in Figure 2.7(b). In the mid-depth region, it is skewed toward the channel wall ($V > 0$) whereas it is negative ($V < 0$) near both the ice cover and the channel bed. In this region, the numerical value of $V(z)$ reaches $\approx 2\%$ of the $\overline{U}$. To investigate the dependence of $V(z)$ on the computational grids, all profiles of $V(z)$ are shown simultaneously on three grid configurations (Grid-1, Grid-2, and Grid-3). The computational results yield similar distributions of $V(z)$ in both verticals. In brief, the obtained distribution of $V(z)$ is consistent across grid resolutions. Due to the roughness values, only the computational data from Grid-2 (case 4 in Table 2.3) are used to report the results in the following discussions.

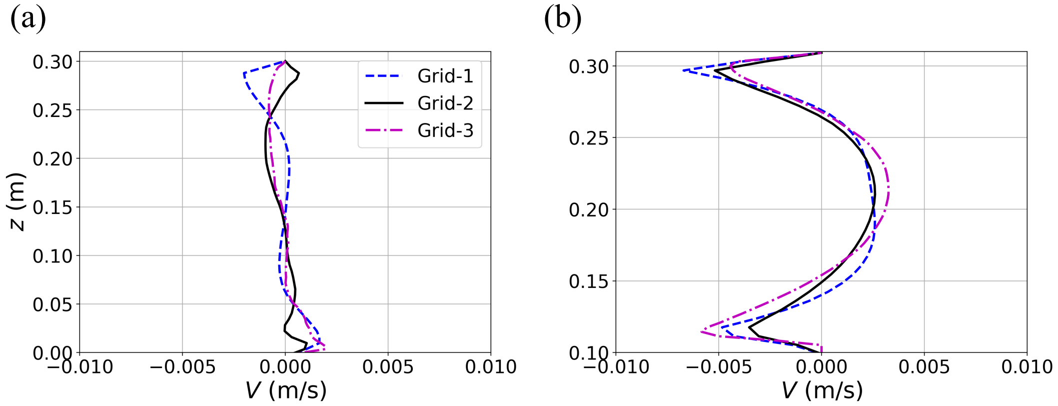

Figure 2.7. The cross-stream velocity profile ($V(z)$) along the depth from large-eddy simulation under different grid levels Grid-1 ($1.3M$), Grid-2 ($5M$), and Grid-3 ($10M$) in cases 1, 4, and 5 (Table 2.2) at cross-section 4. The verticals are at (a) $y = 0.59\ m$ in the main channel, and (b) $y = 0.91\ m$ on the floodplain (see Figure 2.1).

The secondary flow pattern in the channel is reconstructed from the LES results as displayed in Figure 2.8. The secondary flow patterns of Case 4 (Table 2.3) are shown in Figure 2.8(a). Remarkably, the two-layer structure appears on the floodplain near both banks, which is consistent with the double-stacked theory. On both floodplains, two streamwise circulations are found on top of each other over the flow depth of 0.2 m. These two circulations have opposite rotational directions: (1) clockwise in the ice layer circulation, and (2) counter-clockwise in the bed layer circulation.

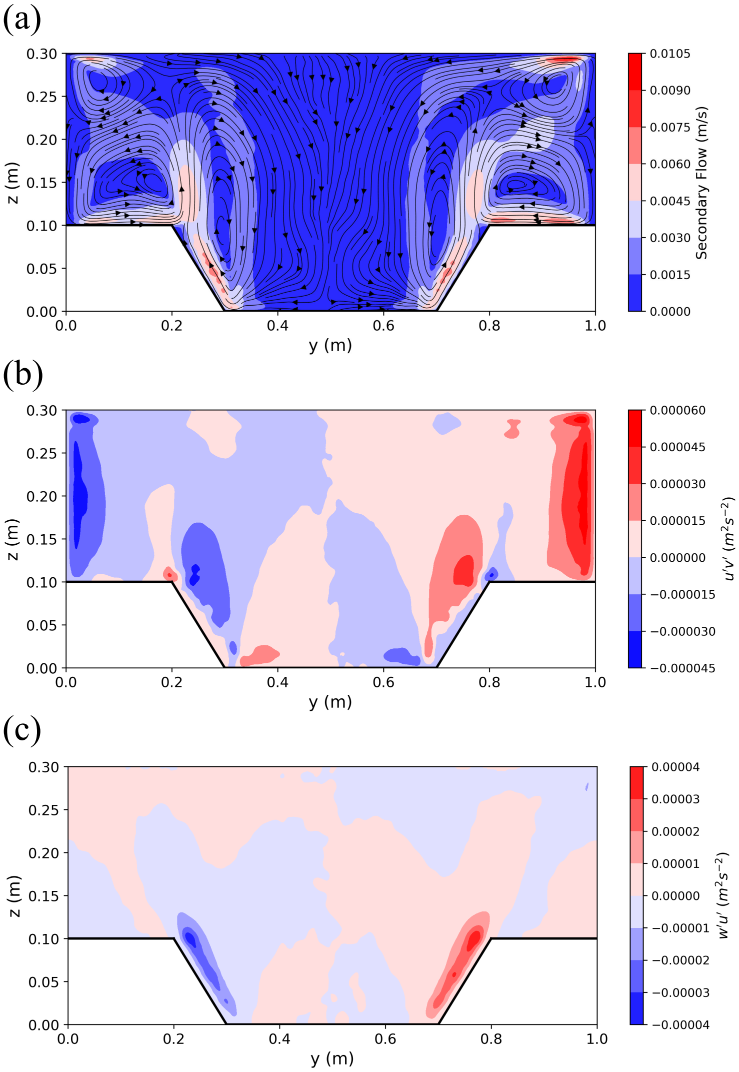

Figure 2.8. Reconstruction of secondary flow patterns from large-eddy simulation (Case 4) at the outlet. (a) The secondary flow patterns and circulations are generated using streamlines. The cross-stream (V) and vertical (W) velocity components are used to generate the streamlines and contours. (b) Cross-sectional distribution of the turbulence statistics for $\overline{u'v'}$, and (c) $\overline{u'w'}$. The area of high turbulent stresses corresponds well to the dynamics of the secondary flows.

The circulations near the ice layer rotate towards the channel center. The presence of these circulations shows the impact of rigid walls near the top (ice) and bottom (channel bed) boundaries. Interestingly, there is only one large circulation on the side slope ($0.7 \leq y \leq 0.8$) due to a strong downward movement of the secondary flows near the channel bed. The maximum secondary flow is located near the channel bed (both the side slope and the floodplain). Considering the bulk velocity ($\overline{U} = 0.204\ m/s$), the maximum secondary flow velocity reaches to $\approx$ 5% of $\overline{U}$. In conclusion, the LES results indicate a significantly strong secondary flow, which forms the double-stacked circulations on floodplains.

The distribution of turbulence statistics over one cross-section is presented in Figure 2.8(b) and 2.8(c). The turbulent stresses ($\tau_{xy} = -\rho\overline{u'v'}$ and $\tau_{zx} = -\rho\overline{u'w'}$) are highly correlated to the secondary flow dynamics on the floodplain and the side slopes as seen Figure 2.8(b) and Figure 2.8(c). The interaction between the banks (vertical walls) and the flow is shown as the elevated magnitude of $\overline{u'v'}$ as depicted in Figure 2.8(b). Both components $\overline{u'w'}$ and $\overline{u'w'}$ reach their highest magnitudes on the side slope as it is the location of the strongest upward movement in the secondary flows as illustrated in Figure 2.8(b) and (c). In short, the patterns of secondary flows correlate strongly with turbulent stresses.

2.5.2. Validation of SKM-based solution

The analytical solution (Equation 2.7 and 2.9) is reconstructed by fitting with the measured data using the reported values of f_d, λ_d, and K in F. Wang et al., 2020 (see Table 2.5). Note that the values of C_1, C_2, C_3, and C_4 (Equation 2.7 and 2.9) are not reported by F. Wang et al., 2020. Therefore, a fitting procedure was carried out to determine the values of (C_1, C_2- Equation 2.7) and (C_3, C_4 - Equation 2.9) in both the main channel/floodplain and the side slopes, respectively as seen in Table 2.5. The obtained fitted parameters are used to generate the complete depth-averaged profile in the cross-section.

Table 2.5. Fitted parameters of the analytical method (Equation 2.9 and 2.7) for each section in the trapezoidal channel (Figure 2.1). Note that values of K, f_d, and λ_d are taken from F. Wang et al., 2020. Abbreviations: Main Channel (MC), Side Slopes (SS), Floodplain (FP).

Section	f_d	λ_d	K (%)	C_1	C_2	C_3	C_4
MC	0.0280	0.067	1	-3×10^{-5}	9.9×10^{-3}	-	-
SS	0.0307	0.098	0.1	-	-	-0.143	1.5×10^{-4}
FP	0.0321	0.097	-3.5	2.5×10^{-7}	0.016	-	-

The comparison between the analytical solution and the measured data (F. Wang et al., 2020) is shown in Figure 2.9. The measured U_d profile at the channel center maintains a relatively large value in the main channel ($0.5 \leq y \leq 0.7$) and only decreases as the side slope starts ($y \geq 0.7\ m$). As the side slope of the trapezoid begins ($y = 0.7\ m$), the measured value of U_d decreases until the slope ends ($y = 0.8\ m$). U_d slightly increases at the transition from the slope to the floodplain at $y = 0.8\ m$. It becomes constant again in the floodplain. U_d continues to decrease sharply as near the vertical walls ($y = 1\ m$ and $U_d = 0$). The analytical solution fails to capture the flat profile in the main channel region as well as the slight increase at $y = 0.3\ m$ as seen in Figure 2.9. Note that the analytical solution is specifically available for a region with a constant slope, using either Equation 2.7 ($s = \infty$) or Equation 2.9 ($s = 1$), the analytical profile cannot be applied for a region with non-constant slope.

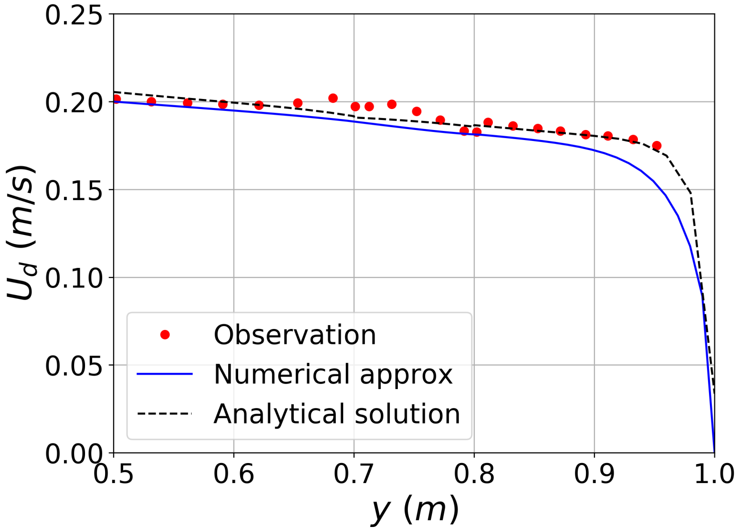

Figure 2.9. Validation of numerical reconstruction (Equation 2.17) for the depth-averaged velocity ($U_d(y)$) using $N = 101$. The numerical approximation is compared with the experimental observation of F. Wang et al., 2020, and the analytical solution (Equation 2.7 and 2.9). The experimental data is only available on one-half (the right side) of the trapezoidal channel ($y \geq 0.5\ m$).

The value of U_d using the proposed numerical procedure (blue solid line - Equation 2.17) is now validated with the measured data and the analytical solution as shown in Figure 2.9. In this case, the $mid-boundary$ location is chosen as the channel's center exactly as required by the numerical procedure in section 2.3. Although the channel geometry varies largely from $s = \infty$ in the main channel and floodplain, to $s = 1$ on the side slope, the numerical approximation is able to compute U_d with any value of s, eliminating the need for switching the form of solution. Results in Figure 2.9 show that the numerical approximation of U_d agrees well with the measured data based only on the reported values of the governing parameters: λ_d, f_d, and K. In conclusion, proposed numerical solution agrees well with both the measured data and the analytical solution without the need to introduce additional parameters in the trapezoidal channel.

2.5.3. Application for field data

2.5.3.1. Range of parameters

Three parameters (K, f_d, and λ_d) are required for the SKM-based approximation, such parameters must be evaluated before applying Equation 2.17 for field conditions. However, the ranges of these parameters have not been reported for ice-covered flows before. Thus, a systematic investigation of these ranges is needed as explained below.

The magnitude of K is varied in the range of 0.001 to 0.1 as suggested by previous works for both experimental data (F. Wang et al., 2020) and field condition (Ervine et al., 2000). Note that the value of K is typically $0.005 \leq K \leq 0.05$ in meandering rivers (Devi et al., 2021; Ervine et al., 2000).

The friction factor (f_d) can be estimated as F. Wang et al., 2020:

$$f_d = \frac{8g}{\chi_b + \chi_i} \left[\frac{n_b^{3/2} + \beta n_i^{3/2}}{(1+\beta)R} \right]^{1/3} (\chi_b n_b^{3/2} + \chi_i n_i^{3/2}) \tag{2.18}$$

where R is the hydraulic radius of the bed and ice layer ($R = A/P$); n_b and n_i are Manning's coefficients for the bed and ice, respectively; and $\beta = \chi_i/\chi_b$.

The range of Manning's coefficients for both the river bed (n_b) and the ice cover (n_i) are also investigated. For silt and clay in the river bed of the Red River, n_b is chosen to vary from $n_b = 0.014$ to 0.046 (Barnes, 1967). For ice roughness, $n_i = 0.030$ varies from $n_i = 0.01$ to 0.03 (H. T. Shen & Yapa, 1986). Following Equation 2.18, the resulted value of f_d varies from 0.011 to 0.11.

The value of λ_d has been reported to vary from $\lambda_{MC} = 0.067$ to $\lambda_{FP} = 40$ in the experiment of Shiono and Knight, 1991. In the current work, λ_d is varied within the range of $\lambda_d = 0.035 - 0.1$ as reported in Pu, 2019.

2.5.3.2. Validation with field data

The parameters (K, f_d, and λ) are found for each cross-section I_a, I_b, I_c, I_d, and I_e separately by fitting the SKM-based solution (Equation 2.17) with the field data (see section 2.3.3) using the ranges in section 2.5.3.1. From now on, the lateral (cross-stream) direction is denoted as ℓ instead of y to differentiate the field data (meandering river) from the laboratory experiment (straight channel).

As discussed in section 2.3, Equation 2.17 requires the splitting of the cross-section into two parts: (1) the left part (outer bank); and (2) the right part (inner bank). During the fitting, the values of K and λ are selected for each cross-section while f_d is calibrated for the left and right parts independently to find f_d^l (left) and f_d^r (right).

For meandering rivers, it is not obvious how to split the cross-section appropriately because the thalweg (H_{max}) and the locations of the maximum velocity (U_d^{max}) do not coincide typically. To address this splitting issue, the separation line $mid - boundary$ is selected in two approaches: In *Approach 1*, the $mid - boundary$ is at the ice hole with maximum velocity (U_d^{max}). In *Approach 2*, the $mid - boundary$ is at the thalweg location (H_{max}). While it is feasible to determine in advance the location of the thalweg (under ice-free condition, for example), it is not practical to determine the maximum velocity location before the actual ice measurement. Comparing Figure 2.3 and Figure 2.10, it is shown that the locations of U_d^{max} in cross-sections I_a, I_b, and I_c were slightly different ($\approx 5m$) from the locations of H_{max} (thalweg). At I_d, the locations of U_d^{max} and H_{max} coincide. Therefore, the comparison between computed values of U_d from *Approach 1* and *Approach 2*, and the measured depth-averaged velocity using ADCP will provide an uncertainty quantification on the estimated U_d.

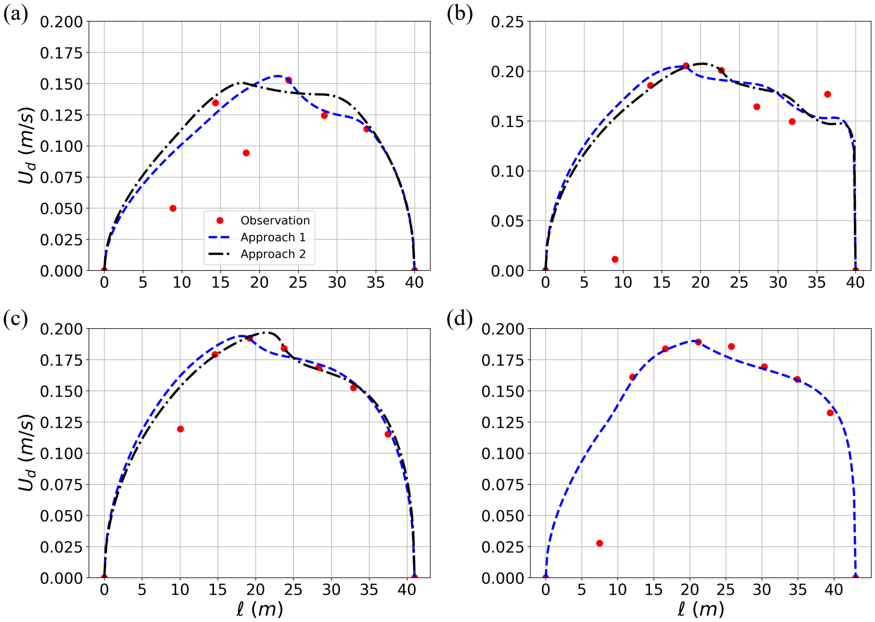

Figure 2.10. The distribution of depth-averaged velocity (U_d) at cross-section (a) I_a, (b) I_b, (c) I_c, and (d) I_d. The numerical approximations (Equation 2.17) are used to reconstruct U_d using two different approaches: (1) Approach 1 (maximum velocity location - blue dashed lines), and (2) Approach 2 (thalweg location - black dashed lines). The maximum velocity location coincides with the thalweg location in cross-section I_d. Therefore, a single U_d profile is shown for I_d.

The fitted parameters for all cross-sections using *Approach 1* and *Approach 2* are shown in Table 2.6 and Table 2.7, respectively. Comparing the results from *Approach 1* and *Approach 2* in Figure 2.10, it is evident that the fitted profiles U_d do not depend on the choice of the $mid-boundary$ point significantly. Comparing the obtained values of $K, \lambda_d, f_d^r, f_d^l$, it is clear that the differences are minimal between the two approaches. In short, the choice of the $mid-boundary$ has a minimal impact on the fitted parameters as well as the obtained profile U_d.

Table 2.6. Fitting parameters to estimate U_d profile using Approach 1 (the $mid-boundary$ location at U_{max}).

Section	Mid-boundary Vertical	f_d^l	f_d^r	λ_d	K
I_a	4	0.090	0.16	0.090	0.016
I_b	3	0.045	0.080	0.090	0.025
I_c	3	0.055	0.095	0.090	0.020
I_d	4	0.06	0.095	0.090	0.020
I_e	3	0.065	0.180	0.050	0.017

Table 2.7. Fitting parameters to estimate U_d profile using Approach 2 (the $mid-boundary$ location is at H_{max}).

Section	Mid-boundary Vertical	f_d^l	f_d^r	λ_d	K
I_a	3	0.095	0.120	0.09	0.016
I_b	4	0.045	0.090	0.090	0.015
I_c	4	0.055	0.110	0.090	0.020
I_d	4	0.06	0.095	0.090	0.02
I_e	5	0.065	0.300	0.050	0.010

2.5.3.3. Sensitivity analysis

The sensitivity of U_d with the governing parameters (K, λ_d, f_d) is investigated by perturbing these parameters from the fitted values ($f_d^l = 0.06, f_d^r = 0.095, \lambda_d = 0.09, K = 0.02$ (Table 2.6 and 2.7) for cross-section I_d. Note that the locations of U_{max} and H_{max} coincide at I_d. Therefore, there is only one choice for the $mid-boundary$ location. During the perturbation, only one parameter (either K, λ_d, f_d^l, or f_d^r) is changed whereas the others are kept unchanged as shown in Figure 2.11. First, results show that the profile U_d is most sensitive to the choice of the friction factor f_d as illustrated in Figure 2.11a. This result justifies the rationale to separate the choice for f_d^l and f_d^r separately for the left and right parts of each cross-section. Second, the impact of the dimensionless eddy-viscosity (λ_d) is found to be relatively insignificant as seen in Figure 2.11b. Although the value of λ_d is perturbed to very low and high values ($\lambda_d = 0.001$ to $\lambda_d = 1$), the profile of U_d does not change considerably. Third, the sensitivity of the secondary flow coefficient (K) is tested as well. Results show that K has a relatively low impact on the depth-averaged velocity profile as seen in Figure 2.11c. A low value of K coefficient tends to elevate U_d^{max} towards the outer bank. In conclusion, the friction factor plays the most important role in determining the U_d profile.

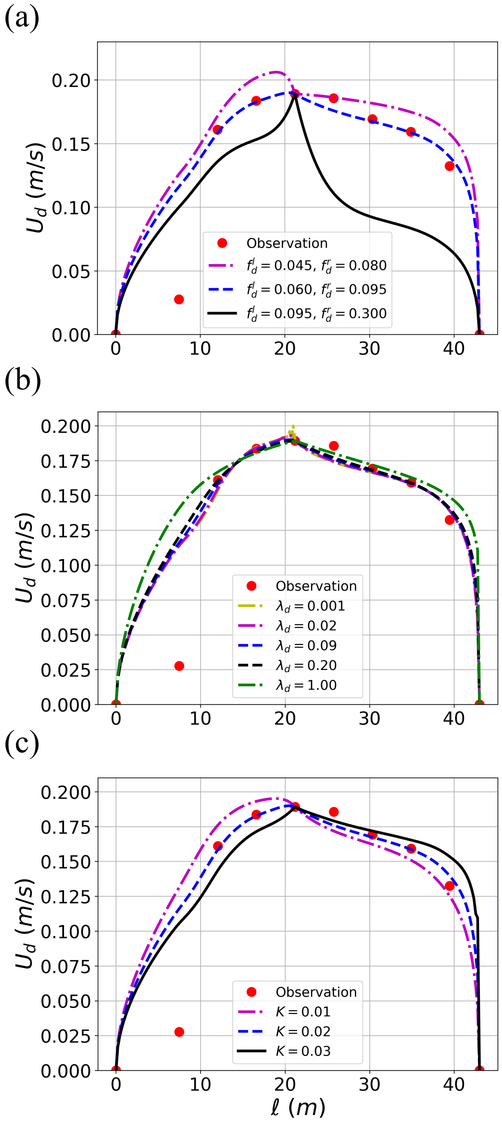

Figure 2.11. The sensitivity of $U_d(y)$ on the variability of governing parameters: (a) the friction factors (f_d^l and f_d^r); (b) the dimensionless eddy-viscosity (λ_d); and (c) the secondary flow coefficient (K).

2.6. Discussion

2.6.1. Numerical procedure to compute U_d

In this study, a novel method for computing a depth-averaged profile (U_d) in ice-covered streams is proposed using the Shiono-Knight method (SKM). The proposed method is validated with the laboratory data of F. Wang et al., 2020 and the results from large-eddy simulation as shown in Figure 2.9. The method is then applied for field data (Koyuncu & Le, 2021) in a bend of the Red River (United States) as depicted in Figure 2.10. The results show that the proposed method can replicate the experimental and simulation data well. The proposed method alleviates the constraints of the analytical solutions (F. Wang et al., 2020), which are only available for simple cross-sections. Therefore, proposed method applies to alluvial channels with arbitrary cross-sections.

The proposed method (Equation 2.17) requires only the knowledge of (i) the Darcy-Weisbach friction factor (f_d); (ii) the dimensionless eddy viscosity (λ_d); and (iii) the secondary flow factor K. As shown in section 2.5.3.1, it is possible to estimate the range of values of f_d, λ_d, and K using physical arguments Ackers, 1991. This is in contrast to the need to calibrate C_1, C_2, C_3 and C_4 in the analytical solution (Equation 2.9 and Equation 2.7) for a specific case in which it is unclear how to determine these values using physical measurements. In short, the proposed method is fully physically-based and the fitted values of f_d, λ_d, and K can be used to interpret the hydraulic characteristics of the channel.

This method requires the separation of one cross-section into the left and right parts and the value of U_d at the separation line (mid-boundary location). As Equation 2.17 only requires boundary conditions at the beginning and end verticals, it does not dictate how to choose the mid-boundary location. While the choice of the mid-boundary location is obviously at the channel's center for symmetrical channels (see Figure 2.1), it is not entirely clear how to apply the procedure for irregular cross-sections because the thalweg (H_{max}) and the location of U_d^{max} are not necessarily at the same place. The location of U_{max} tends to shift towards the outer bank (Abad & Garcia, 2009) in meandering channels. The analysis in Figure 2.10 indicates that the choice of the mid-boundary location does not significantly affect the reconstructed U_d profile in the straight part of the river reach. This is important because the cross-section shape $H(y)$ can be measured independently from the flow measurement during the open-surface condition. Therefore, the profile of U_d under ice-covered conditions can be recovered using the proposed method in this study with a single point of measurement at the thalweg location. This advantage will enable the fast calculation of $U_d(y)$ if the values of f_d, λ_d, and K are estimated from physical arguments (Tian et al., 2021).

The analysis in Figure 2.11 shows that f_d has the most significant impact on the $U_d(y)$ profile. As the cross-section is split into two parts, the friction factors of the left and right sections of each cross-section (f_d^l and f_d^r) are found to be slightly different from each other as shown in Table 2.6 and Table 2.7 for cross-section I_a to I_d. The results show that the friction factor near the inner bank (right) is always greater than the friction factor near the outer bank (left): $f_d^r > f_d^l$. These values of f_d agree well with the expected range in section 2.5.3.1. This is an unexpected finding since the measured values of U_d do not indicate a large skewness of the profile toward the outer bank. However, the proposed method can reflect this trend.

2.6.2. The double-stacked vortices

Laboratory conditions (Urroz & Ettema, 1994a) indicate that the vertical profiles can possess two points of inflections (Tsai & Ettema, 1996) in ice-covered flows. Field measurement of Demers et al., 2011 confirms that this feature indeed exists in a natural bend. Urroz and Ettema, 1994a suggests that the flow structures consist of two counter-rotating circulations in the same vertical. Field data of Lotsari et al., 2017 suggests that the presence of the double-stacked vortices is sensitive to the water depth. The simulation results for the trapezoidal channel in Figure 2.8 indicate that the double-stacked vortices can exist in the shallow area (floodplain). This result agrees well with the secondary flow patterns reported by F. Wang et al., 2020. Moreover, results indicate that the peak secondary flow is approximately 5% of the bulk velocity $\overline{U}$, which is consistent with the observed ranges of the coefficient K in Table 2.5. In addition, the secondary flow pattern suggests that the turbulent stresses are strongly correlated with the formation of the double-stack vortices in Figure 2.8(b) and (c). This is remarkable because it highlights that it is possible for the presence of high turbulent stresses near channel banks due to the interaction of these vortices with the channel's bed.

2.6.3. Limitation

As Equation 2.17 is derived for a straight channel (see Equation 2.1), it is important to test its applicability for cross-sections at meandering bends. While cross-section I_a, I_b, I_c, and I_d are at the straight section of the river reach, the cross-section I_e is at the bend apex as shown in Figure 2.2. Note that the cross-section shape of I_e is symmetrical (the thalweg at $\ell \approx 20m$) as shown in Figure 2.12(a). The locations of U_{max} and H_{max} are separated at a distance of more than 5 m. Two approaches of fitting (Approach 1 and 2) provide significantly different profiles as seen in Figure 2.12(b). Moreover, both approaches cannot correctly capture the location of U_d^{max}. In addition, the fitted values of f_d^r in Table 2.6 and Table 2.7 are much higher than the expected value of 0.1. These results indicate that the proposed method is mostly applicable to straight reaches. When it is applied for curved bends, its result might yield a discontinuous shape of U_d.

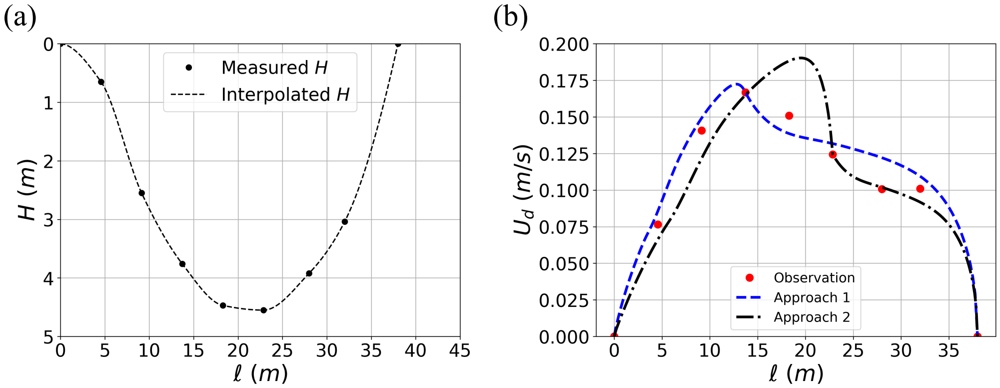

Figure 2.12. (a) Cross-section I_e at the bend apex (see Figure 2.2); and (b) U_d profiles based on Approach 1 and Approach 2.

2.7. Conclusion

A new method for computing depth-averaged profiles in ice-covered flows is proposed. The method is then validated with laboratory, numerical simulation, and field data. Results showed that the method is applicable to natural channels with irregular cross-sections. The following conclusions are made:

1. The proposed method (Equation 2.17) is applicable for ice-covered flows with arbitrary cross-sections. However, it is mostly suited for straight river reaches. When it is applied to river bends, it might result in inaccurate profiles.

2. Once the cross-section ($H(y)$) is known in advance, the proposed method can provide the depth-averaged profile ($U_d(y)$) with data from a single ice hole at the thalweg location.
3. Large-eddy simulation results show that the double-stacked vortices might exist in ice-covered streams near both banks if the local flow depth is low. The presence of the double-stacked vortices might impact the turbulent stresses.
4. Results show that the key parameters governing the U_d profile are (K, f_d, λ_d). The value of f_d is the most important factor to determine the shape of the profile. It is possible to extract the value of f_d from field measurements, which can provide important information on the resistance of ice cover.

3. ON THE IMPACTS OF ICE COVER ON FLOW PROFILES IN A BEND [2]

3.1. Abstract

In this study, the impacts of ice covered on flow and bed shear stress profiles are investigated in a river bend. I perform field measurements using Acoustic Doppler Current Profiler (ADCP) in a bend of the Red River, North Dakota, the United States. Field campaigns were carried out under both open-surface and ice-covered conditions in 2020 and 2021. Results show that the time-averaged velocity profile follows closely the quartic solution (Guo et al., 2017) under full ice coverage. While the flow profile under open-surface condition follows closely the logarithmic law near the bed, it is challenging to identify the logarithmic layers in our measured data under ice-covered condition. Results also show that the impact of ice coverage is most significant near both banks where the vertical velocity profile is modified significantly due to the interaction of turbulent flows with the ice cover. Results suggest that the bend curvature and ice coverage both have significant impacts on the velocity profile as well as the distribution of the bed shear stresses. Our findings provide new insights on sediment transport processes of ice-covered rivers, especially during the break-up period when the surface coverage changes rapidly.

3.2. Plain summary language

As climate change continues, shorter winter is expected to result in a smaller number of ice-covered days for natural streams. While ice cover has been linked to a variety of eco-hydraulic issues, it is unclear on the relationship between ice coverage and changes in

---

[2] The content of this chapter was co-authored by Berkay Koyuncu and Trung Le, and published as a research article in the *Water Resources Research* Journal. Koyuncu was the main analyst and writer. Le provided feedback, served as a proofreader, and checked the results.

river hydrodynamics. Thus, the understanding of ice-covered flows has become a critical issue to predict morphological and ecological conditions of river flows in cold regions. This study aims to identify the impact of ice by conducting field-scale observations and comparing with analytical models. Our results show that the ice layer alters flow patterns beneath it, which leads to active areas near banks. This new finding suggests that ice cover might play a significant role in sediment transport near banks in Spring when its extension can change sharply in a short amount of time.

3.3. Introduction

Ice coverage has been recognized as an important hydraulic aspect of alluvial channels for a long time (Guo et al., 2017). The role of river ice in ecological (Prowse, 2001c), morphological (Ettema, 2002), and hydraulic aspects (Prowse, 2001a) have been well recognized. Recent evidence suggests that it plays an important role in regulating large-scale turbulent structures (P. M. Biron et al., 2019) and ultimately channel lateral migration (Turcotte et al., 2011). Under the impact of climate change, the loss of river ice (Yang et al., 2020) is expected to lead to detrimental consequences for aquatic environments (Thellman et al., 2021). Despite its importance, our understanding of icy flows is limited because of challenges related to field measurements. The goal of this study is to examine the impacts of ice coverage on flow profiles in a meandering bend, a common feature of the riverine system.

Field measurement of turbulent flows in rivers is challenging even under open-surface condition (Petrie et al., 2013), especially when secondary flow is observed (Moradi et al., 2019). The measurement under ice coverage poses a different set of safety and accuracy issues when instruments are placed beneath the ice layer (P. M. Biron et al., 2019). Under a fully frozen surface, it is necessary to drill holes across the ice layer to submerge the sensor.

In particular, it is challenging to obtain reliable data close to the ice layer as well as the river bed (Attar & Li, 2013).

As the top surface is frozen during winter (Ettema, 2002), it provides layer of roughness in addition to the river bed. The presence of the ice coverage alters the spatial distribution of the velocity profile. Ice coverage creates a significant difference between the physical characteristics of surface and bed, forming an asymmetrical flow configuration (Chen et al., 2018; Parthasarathy & Muste, 1994). The asymmetrical flow configuration has been well studied under laboratory conditions (Hanjalić & Launder, 1972) in which the aspect ratio (width/depth) has been shown to control the overall flow dynamics.

There has been no universal law for asymmetrical flow configuration in rivers. In contrast to the logarithmic law of the open-surface case, it is unclear on the form of the time-averaged velocity profile in the asymmetrical configuration (Guo et al., 2017). There exists a maximum velocity, which typically does not locate on the symmetry plane (Tatinclaux & Gogus, 1983; Tsai & Ettema, 1994b; Urroz & Ettema, 1994b). As the shape of the velocity profile is changed under ice-covered condition, its gradient near the river bed is different from the open-surface counterpart (Guo et al., 2017). Therefore, the hydraulics of ice-covered flows differs significantly (Ettema, 2002; Prowse, 2001a) from the open-surface condition.

The main structure of the velocity profile can be described in Figure 3.1. We denote z as the distance from a measured point to the river bed surface as shown Figure 3.1A. The vertical distance corresponding to the maximum velocity u_{max} is z_{max}. Under ice-covered condition, z_{max} separates the profiles into: 1) the ice layer (h_i); and 2) the bed layer (h_b) as shown in Figure 3.1B. Thus the total depth $H = h_i + h_b$. Note that the local depth of a measured point is $h = H - z$. The stationary boundary condition on the ice and the bed surface dictate that $u(z=0) = u(z=H) = 0$.

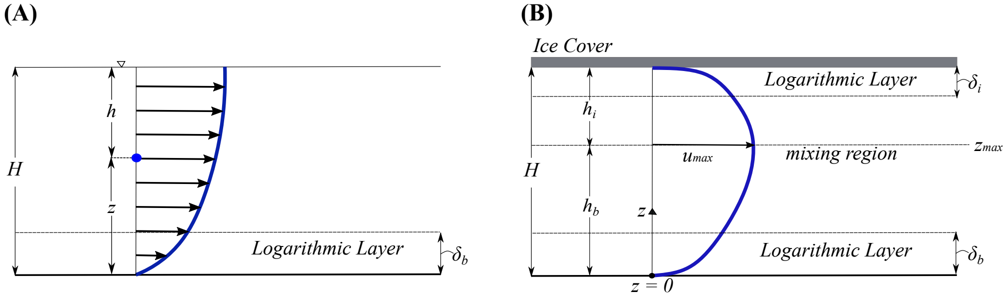

Figure 3.1. The differences in flow configuration under: (A) open-surface condition, and (B) ice-covered condition. Under open-surface condition, the total depth $H = h + z$ is separated into two portions: i) the distance to the river bed (z) of a measured point; and ii) its local depth (h). Under ice-covered condition, two logarithmic layers are assumed near the ice layer (δ_i) and the river bed (δ_b). The z_{max} is the position of the maximum velocity (u_{max}) from the river bed.

Under open-surface condition, one fundamental quantity that characterizes velocity profile near the river bed (Wilcock, 1996) is the friction velocity ($u_b^\star$). It can be linked to the bed shear stress as $\tau_b = \rho(u_b^\star)^2$, which is needed to determine sediment transport processes (Chaudhry, 2007). Therefore, the evaluation of $u_b^\star$ and τ_b are frequently required in river hydraulics.

Direct measurement of the bed shear stress τ_b or shear velocity $u_b^\star$ in rivers is not feasible (Petrie & Diplas, 2016) with the current technologies. Thus, many methods have been proposed (P. M. Biron et al., 1998) to calculate $u_b^\star$ indirectly from velocity measurements. Since the flow in the alluvial channel is characterized by high Reynolds numbers, turbulent statistics are typically involved in the calculation of $u_b^\star$ (A. Sukhodolov et al., 1999): (a) Turbulent Kinetic Energy (TKE) (Soulsby, 1981), (b) Reynolds stress, and (c) Wall similarity methods (Hurther & Lemmin, 2000; López & García, 1999). These methods have high accuracy and they do not assume a predetermined velocity profile. However, they require the full calculation of the Reynolds stress tensor. Therefore, precise measurement of turbulent fluctuation u' is required along the water column in a pointwise manner. For a small or medium river (A. Sukhodolov et al., 1999), it is a tedious task to perform this type of measurement along a cross-section in a reasonable amount of time because the sensor needs to traverse systematically point-to-point. For a large river, it is not feasible to carry out such a field campaign due to the potential change of the hydrological conditions (water level and discharge), which might alter completely the turbulent regime. Thus, these methods are not widely used under field conditions.

The most common method to determine $u_b^\star$ in practice is to utilize the time-averaged velocity profile to determine $u_b^\star$ via the assumption of a logarithmic layer close to the river bed (P. M. Biron et al., 1998; Petrie & Diplas, 2016; Petrie et al., 2013). The main assumption is that there exists an equilibrium layer near the river bed at which the turbulence production and dissipation balances out to give rise to the logarithmic law. In zero pressure gradient, the universal law of the wall has been verified in many laboratories and numerical simulations (Volino & Schultz, 2018). This logarithmic method does not require the acquisition of highly resolved turbulent statistics (P. M. Biron et al., 1998) and thus this procedure can be applied for many types of measurement devices including the popular Acoustic Doppler Current Profiler (ADCP) (Muste, Yu, Pratt, & Abraham, 2004; Muste, Yu, & Spasojevic, 2004; Petrie & Diplas, 2016). Since ADCP can provide the entire velocity profile in the water column in one measurement, the sensor is kept afloat at a stationary location (fixed-vessel method) (Petrie & Diplas, 2016) for a period, which can vary from 1 to 25 minutes (Petrie et al., 2013). The time-averaged velocity profile is then fitted with the logarithmic law to find

$u_b^\star$. Note that due to the spatial averaging nature, the ADCP data cannot be represented using a prefixed confidence limit (Petrie & Diplas, 2016; Petrie et al., 2013).

In order to compute shear velocities for ice-covered flows (A. Sukhodolov et al., 1999), it has been hypothesized (two-layer hypothesis) that there exist three regions: (a) two logarithmic layers near the river bed and the ice surface; and (b) the mixing (core) region at the mid-depth as shown in Figure 3.1B. Here, two logarithmic layers are assumed to locate near the top (ice) and bottom (river bed) surfaces.

Using the two-layer hypothesis, the logarithmic law method is typically applied (Ghareh Aghaji Zare et al., 2016) separately within the ice layer (δ_i) and the bed layer (δ_b) as shown in Figure 3.1B. To resolve the logarithmic layers, it is required that measured data must be carried out at locations near the ice layer and the river bed (A. Sukhodolov et al., 1999). However, the validity of the two-layer hypothesis has been questioned (Urroz & Ettema, 1994a) in meandering rivers since the secondary flows (Demers et al., 2011) might alter the local velocity profiles. In addition, it has been pointed out (Guo et al., 2017) that the double log-law profile is not physical as it is impossible to satisfy the continuity condition at the maximum velocity location u_{max}. This challenge motivates the use of the velocity profile (Attar & Li, 2012) to derive $u_i^\star$ and $u_b^\star$ in ice-covered flows. This practice alleviates the requirement of resolving the logarithmic layer but it needs an assumption on the form of velocity distribution, which is usually not known under the field condition. To provide a physical argument for assuming the velocity profile, (Guo et al., 2017) have derived an analytical form of velocity distribution along the water column using an assumption on the distribution of eddy viscosity. However, the accuracy and reliability of this method in estimating $u_i^\star$ and $u_b^\star$ (Guo et al., 2017; F. Wang et al., 2020) has not been examined in river bends.

As the logarithmic layer is considered valid within a thickness of (δ_b) in the bed layer as elaborated in Figure 3.1B, it is common to use wall units as dimensionless hydraulic quantities. In this approach, $u_b^\star$ and ν are used to form the velocity and viscous length scales. The friction Reynolds number based on shear velocity ($u_b^\star$), the logarithmic layer thickness δ_b, the vertical distance from the river bed z, and the non-dimensional velocity profile $u^+(z^+)$ are expressed in terms of wall units as:

$$\begin{aligned} Re_\tau^b &= \frac{Hu_b^\star}{\nu} \\ \delta_b^+ &= \frac{\delta u_b^\star}{\nu} \\ z^+ &= \frac{zu_b^\star}{\nu} \\ u^+(z^+) &= \frac{u(z)}{u_b^\star} \end{aligned} \tag{3.1}$$

Under laboratory condition, the logarithmic layer δ_b^+ can extend (Guo et al., 2017) up to $z^+ = 10^4$.

A similar procedure can be carried out to define the shear velocity for the ice layer as seen in Figure 3.1B with the shear velocity ($u_i^\star$):

$$\begin{aligned} Re_\tau^i &= \frac{Hu_i^\star}{\nu} \\ \delta_i^+ &= \frac{\delta_i u_i^\star}{\nu} \\ h^+ &= \frac{hu_i^\star}{\nu} \\ u^+(h^+) &= \frac{u(h)}{u_i^\star} \end{aligned} \tag{3.2}$$

Under open-surface condition, the existence of the logarithmic layer has been assumed to follow the theoretical estimate (Gao et al., 2020) as:

$$2.6Re_{\tau}^{1/2} \leq z^{+} \leq 0.15Re_{\tau} \tag{3.3}$$

The upper bound (thickness) for the logarithmic layer is thus: $\delta^{+}_{theory} = 0.15Re_{\tau}$.

To date, there has been no report on the thickness of the logarithmic layer under ice-covered condition.

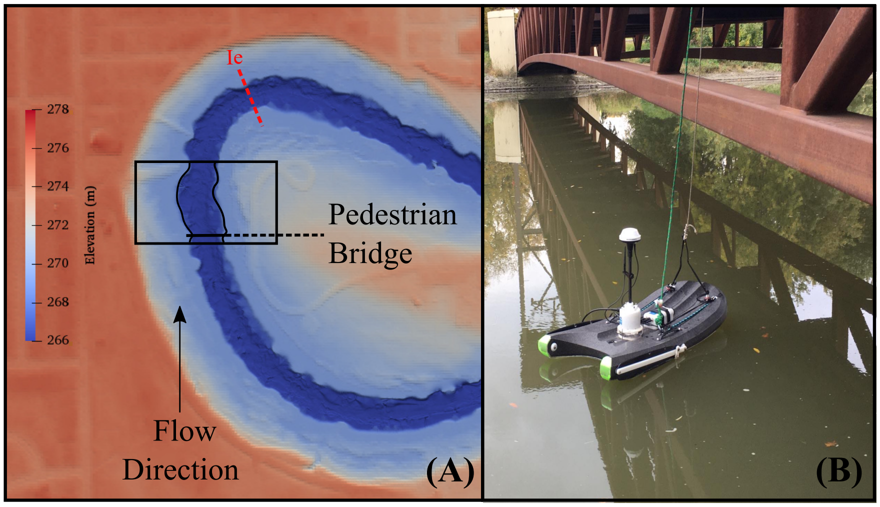

Figure 3.2. The study area and the measurement cross-sections. **(A)** The area of interest at the apex of a bend, and the location of cross-section Ie. The flow is in the North direction. **(B)** Under open-surface condition, the ADCP M9 sensor is deployed near the pedestrian bridge with the fixed-vessel methodology in five measurement days Oa, Ob, Oc, Od, and Oe (see Table 3.1). On each measurement day, the $M9$ is stationed in a number of vertical locations across the bridge as shown in Table 3.1.

As mentioned above, one important factor affecting the distribution of $u_b^{\star}$ is the effect of secondary flows (Petrie & Diplas, 2016). Laboratory experiments (Anwar, 1986) have shown that the vertical velocity profile deviates from the logarithmic law in the bend region. In complex three-dimensional flows, it is impossible to derive $u_b^{\star}$ using the logarithmic hypothesis (P. M. Biron et al., 2004). The distribution of the bed shear stress (τ_b) and thus the shear velocity ($u_b^\star$) has been shown to be dependent on the local secondary flows (Bathurst et al., 1979; Stoesser et al., 2010). Since the understanding of secondary flows under ice-covered conditions is limited, it is unclear how ice cover impacts the velocity and shear velocity distribution in meandering rivers. A laboratory experiment (Urroz & Ettema, 1994a) has shown that there exist two counter-rotating vortices (double-stacked cells) in the secondary flow pattern of an ice-covered bend. These two vortices are thought to belong to a complex three-dimensional structure of the bend flow. Field measurements of Demers et al., 2011 suggest that this double-stacked cell appears near the bend entrance but diminishes rapidly toward a single helical cell at the bend apex.

The main goal of the current study is to examine the impact of ice coverage on the vertical flow profile and its implication on the cross-stream distribution of bed shear stress.

Field works are carried out under both open-surface and ice-covered conditions to provide the vertical velocity profiles. Whenever appropriate, the logarithmic law is invoked to derive $u_b^\star$ and $u_i^\star$. On the other hand, the applicability of the quartic solution (Guo et al., 2017) will be examined using our measured dataset. The results from these methods are compared to evaluate their compatibility in providing accurate value of shear velocities. The three-dimensional structures of flows under ice coverage are also discussed to identify locations where complex flow patterns might occur and limit the use of analytical methods.

3.4. Methodology

3.4.1. Study area

The Red River is known as a low-gradient river with its regular basis spring floods. The channel bed of the Red River is mostly categorized as clay and fine silt (Weiss et al., 2015). A 2-km long section of the Red River near Lindenwood Park in Fargo, North Dakota was chosen as the study field (Figure 3.2A). A pedestrian bridge in the middle of the apex served as the reference location (Figure 3.2A and 3.2B). At the end of the reach, there exists a United States Geological Survey (USGS) station (USGS FARGO 05054000) at the gage elevation of 262.68 m above the North American Vertical Datum (NAVD88).

3.4.2. Measurement methodologies

Following the suggestion of A. Sukhodolov et al., 1999; A. N. Sukhodolov, 2012, the fixed-vessel (FV) method (Petrie et al., 2013) was used for this study. The Acoustic Doppler Current Profiler (ADCP), Sontek $M9$, was used to measure the velocity components and bathymetry under the SmartPulse mode of 1MHz. Note that the compass calibration must be carried out prior to each measurement. During the field surveys, the blank distance was set to be 0.05 m. The measured bin was adjusted automatically and varied from $0.02 - 0.06$ m depending on the total depth H ($H_{max} \approx 4.1$ m). Bin size at each vertical is monitored in the entire time series. Any time instances that have changes in the value of bin size are removed from the calculation. The signal-to-noise ratio (SNR) of all measurements were monitored online during the campaigns and also examined after the acquisition to check their reliability to avoid beam separation. The presence of signal interference near the river bed ($z \leq 30$ cm) was significant, thus the SNR was monitored closely in this region. If the SNRs from four different sensors were different from each other by 20 dB, the data points were omitted from the calculations.

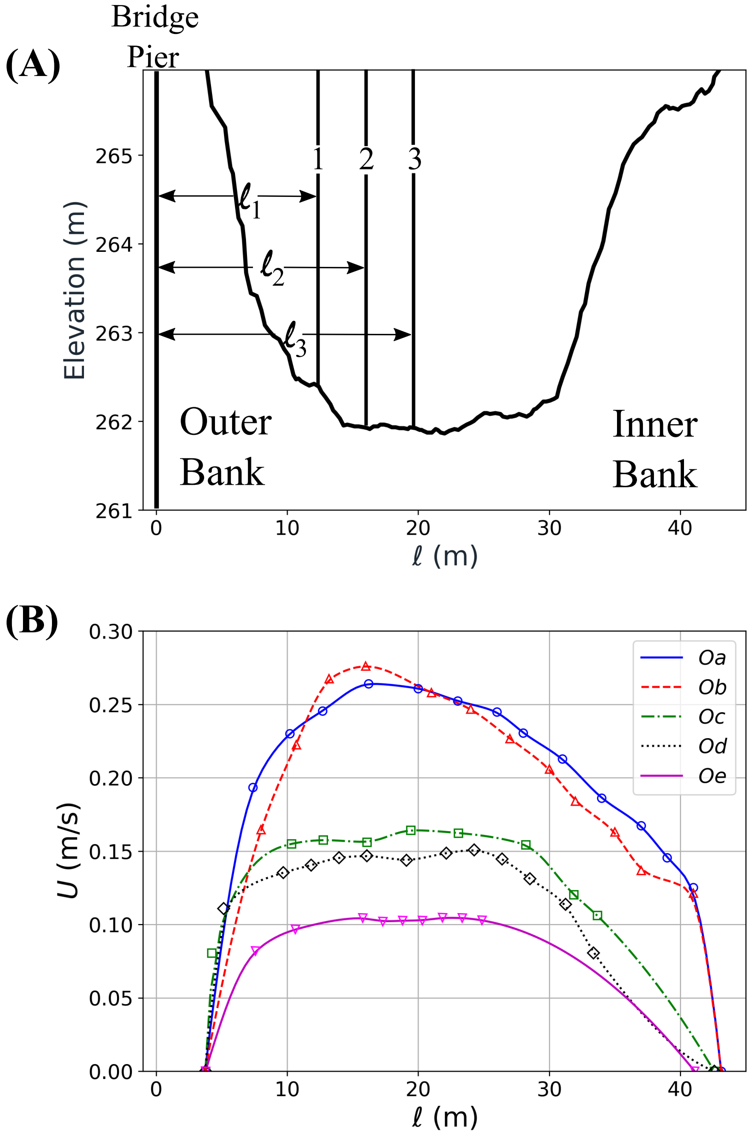

Figure 3.3. The depth-averaged velocity profiles (U) under open-surface condition at the bend apex. **(A)** The cross-section shape at the bridge. The value ℓ denotes the distance of the vertical location to the left bank. **(B)** Depth-averaged velocity profiles under different flow discharge Oa, Ob, Oc, Od, and Oe. The thalweg is defined as area with the total depth $H \geq 3.5$ m, which is in the 10 m $\leq \ell \leq$ 30 m region for this cross-section.

Under open-surface condition, only one cross-section was chosen at the bridge location (see Figure 3.2A) (O) since it was a well-defined cross-section (red line). Measurements under open-surface condition were carried out on five measurement campaigns: (a) $Oct/02/2020$ (Oa), (b) $Oct/04/2020$ (Ob), (c) $Jun/22/2021$ (Oc), (d) $Jun/24/2021$ (Od),

Table 3.1. Expeditions in Fall 2020, Winter 2020 and 2021, and Summer 2021. The hydrological data (flow discharge Q and elevation) is monitored at the USGS Fargo (05054000) Station. The exact location of each vertical location is illustrated in Figure 3.13. T_∞ (minutes) is the total time of measurement in each vertical/(ice hole) location. The notations $M1$ and $M2$ denote two consecutive measurements in one ice hole.

Case	*Date*	*Surface*	Q (m^3/s)	Elevation (m)	No. verticals	T_∞ (mins)
Oa	Oct/02/20	open	23.41	265.96	13	10
Ob	Oct/04/20	open	23.87	265.96	12	10
Oc	June/22/21	open	14.30	265.87	8	15
Od	June/24/21	open	12.20	265.85	11	15
Oe	June/30/21	open	6.82	265.72	6	15
Ia (M1/M2)	Feb/19/21	ice	12.5	265.92	6	2
Ib (M1/M2)	Feb/20/21	ice	12.8	265.92	7	2
Ic	Feb/21/21	ice	13.8	265.93	7	2
Id	Feb/21/21	ice	13.8	265.93	8	2
Ie (M1/M2)	Feb/21/21	ice	13.8	265.93	6	2

and (e) $Jun/30/2021$ (Oe). The $M9$ was attached to a Sontek Hydroboard as shown in Figure 3.2B. The fixed-vessel deployment technique was implemented by taking advantage of the pedestrian bridge. The location of the sensor ($M9$) was monitored both using the on-board GPS as well as the marked locations in the bridge section. As the HydroBoard is attached to the pedestrian bridge, its lateral motion is kept minimal. On-board GPS data shows a variation of 0.35 m in the lateral position of the boat, which is at the accuracy limit of the GPS device. At each vertical location, the $M9$ was kept stationary for at least 600 seconds. The value of (ℓ) indicated the distance from the outer bank along the horizontal axis X as shown in Figure 3.3A. The details of measurements and their associate discharges are shown in Table 3.1.

Under ice-covered condition, measurements were conducted by opening ice holes (Figure 3.4B). The number of opened ice holes varied from 6 to 8 holes depending on the cross-section. Locations of the ice holes were measured from the outer (left) bank. To probe the three-dimensional flow structures at this location, four separate cross-sections were chosen for measurements to elucidate the three-dimensional flow structures: Ia ($Feb/19/21$), Ib ($Feb/20/21$), Ic ($Feb/21/2021$), and Id ($Feb/21/2021$). These cross-sections were separated by a distance of 6.1 m along the North (Y) direction. To avoid bias in the measurement, a separate cross-section Ie ($Feb/21/2021$) at the bend apex, which was 310 m away from the bridge, was selected for an additional measurement (Figure 3.2A). In each measurement, the Sontek $M9$ sensor was placed 0.2 m under the ice layer. The distance from left bank ℓ at each cross-section was noted during the field survey and represented for each cross-section as seen in the diagram of Figure 3.4B. The period of measurement was limited to 120 s to avoid freezing of the equipment's surface since the air temperature went below $-20°$ C. This low air temperature was to ensure that the ice thickness was at least 0.25 m, which was required to be safe to perform measurements. All details of the measurements were summarized in Table 3.1.

3.4.3. Data processing and flow statistics

The raw data of the M9 in text format were processed using my in-house MATLAB code to produce $1Hz$ time series. A separate MATLAB code was used to calculate flow statistics from the time series including: (a) the depth-averaged velocity profiles; and (b) the time-averaged velocity profile for each vertical location. Following the suggestion of Petrie and Diplas, 2016, the depth-averaged value $U(T)$ and the time-average profiles for each vertical $u(z,T)$ were computed as the function of averaging period T as:

$$U(T) = \frac{1}{H}\int_{z=0}^{z=H} u(z,T)dz \tag{3.4}$$

$$u(z,T) = \frac{1}{T}\int_{t=0}^{t=T} u(z,t)dt \tag{3.5}$$

The final values of $U(T_\infty)$ and $u(z,T_\infty)$ correspond to the time-averaged value of the entire record ($T = T_\infty$). They are denoted as the long-term depth-averaged (U_∞) and time-averaged ($u_\infty(z)$) velocities, respectively, to provide a scale to indicate the range of variability of the signals. Note that the notation to describe the long-term (average) values is consistent with the ones proposed by Petrie and Diplas, 2016. Under the open-surface condition, the total length of the measurement period T_∞ for each vertical was $T_\infty \geq 10$ minutes whereas it was only $T_\infty \approx 2$ minutes for ice-covered cases as shown in Table 3.1. In total, there were 50 and 55 depth-averaged time series under the open-surface and ice-covered conditions, respectively. Finally, the calculation of the shear velocity $u_b^\star$ and $u_i^\star$ was based on the values of $u_\infty(z)$ as shown in the next sections. All subsequent analyses are conducted based on the time-averaged (u_∞) and depth-averaged (U_∞) velocity.

3.4.4. The logarithmic law of the wall

The logarithmic law of a rough wall (C. Shen & Lemmin, 1997) is:

$$\frac{u(z)}{u_b^\star} = \frac{1}{\kappa}\ln\frac{z}{z_0} + \beta \tag{3.6}$$

where $\kappa = 0.39$ is the Von Karman constant, β is the additive constant ($\beta = 8.5$). The parameter z_0 is the roughness length. The range of von Karman constant is $0.39 \leq \kappa \leq 0.41$ (P. M. Biron et al., 1998; Marusic et al., 2013; Petrie & Diplas, 2016; Petrie et al., 2013). The value of $\kappa = 0.39$ is selected as the condition of high Reynolds number flows in rivers (Marusic et al., 2013). In natural rivers, this logarithmic law is typically considered valid within a distance δ_b from the river bed. Typically, δ_b varies from 20% to 50% (Petrie &

Diplas, 2016; Petrie et al., 2013) of the total depth H. Under field conditions, the value of δ_b is not known in advance. Therefore, a procedure to determine δ_b will be discussed below.

The shear velocity ($u_b^\star$) and the roughness length (z_0) are found by fitting the Equation 4.3 with the measured data ($u(z)$) in each vertical. A common procedure (Petrie & Diplas, 2016) is to use the linear regression line between the measured value of $u(z)$ and $ln(z)$. As the linear regression line is known, the values of $u_b^\star$ and z_0 are computed as:

$$u_b^\star = \kappa m \tag{3.7}$$

$$z_0 = exp[8.5\kappa - \frac{\gamma}{m}] \tag{3.8}$$

Here, γ and m are the intercept point and the slope of the best-fit regression line, respectively.

Under open-surface condition, the agreement between the linear regression line and the measured data must satisfy (Petrie & Diplas, 2016) the following criteria: (1) the correlation coefficient $R^2 > 0.9$, (2) a positive shear velocity $u_b^\star > 0$, and (3) a realistic value of z_0 (0.001 m $< z_0 <$ 10 m). In brief, the detailed steps of the logarithmic method for both open-surface and ice-covered conditions are as follows:

- *Step 1*: Assume a value of δ_b ranging from $0.05H$ to $1.0H$ with an increment of $0.05H$ for each trial. The fitting to the logarithmic law is performed only when there is sufficient data in the logarithmic layer δ_b. The presence of at least five points within δ_b is required.
- *Step 2*: The velocity magnitude $u(z)$ is plotted against the $\ln(z)$ at every measurement point. Available MATLAB functions, *"polyfit"* and *"polyval"* are called to per-

form linear regression from the selected points in Step 1, to obtain the linear fitting parameters m and γ.

- *Step 3*: The shear velocity is computed as $u_b^\star = \kappa m$.
- *Step 4*: Equation 4.5 is used to compute the roughness length (z_0) using the values of the parameters γ and m.
- *Step 5*: R^2 value is computed from the linear fitting of Equation 4.3 in comparison to the corresponding measured data. The values of R^2, $u_b^\star$, and z_0 are checked simultaneously to validate the presence of the logarithmic layer. The following values are validated with $R^2 > 0.9$, $u_b^\star > 0$, and 0.001 m $< z_0 <$ 10 m.
- *Step 6*: Record the value of R^2 and δ_b. Go back to Step 1 with an increment in the value of δ_b until the best R^2 is found. If the best R^2 is greater than 0.9, move to Step 7.
- *Step 7*: Compute $u_b^\star$ and its associated z_0 corresponding to the best R^2.

The logarithmic fitting is performed for the ice layer in a similar fashion using the non-dimensional distance to the ice layer h^+ as shown in Equation 4.7.

3.4.5. Quartic profile for asymmetrical flows

The quartic profile of Guo et al., 2017 is formulated using the relative distance η, which is defined as $\eta = 2\frac{z}{H}$. The maximum velocity location is defined in term of its relative distance as: $\eta_{max} = \frac{2z_{max}}{H}$.

A non-dimensional parameter (λ) is used to represent the asymmetry of the flow profile as:

$$\lambda = \sqrt{\frac{2}{\eta_{max}} - 1} \tag{3.9}$$

Here $\lambda = \frac{u_i^\star}{u_b^\star}$ quantifies the asymmetry of shear stress on the top ($u_i^\star$) and bottom ($u_b^\star$) surfaces. Therefore, the value of λ is important in determining the shape of the velocity profile. An interim parameter ($\alpha = \frac{1-\lambda}{\lambda-\lambda^{2n}}$) is also used to reflect this asymmetry. In this equation, n is the mixing turbulent intensity. While n can vary depending on the turbulent flow condition, it is found for the symmetric flow condition as $n = 5/6$ (Guo et al., 2017).

The location of the zero shear stress plane (η_c) typically does not coincide (Hanjalić & Launder, 1972) with the maximum velocity location. After the value of λ is obtained from the Equation 3.9, the value of η_c is computed as:

$$\eta_c = \frac{2}{(1 + \lambda^n)} \tag{3.10}$$

Since λ is close to 1, the values of the critical and maximum positions are typically close in the thalweg ($u_c \approx u_{max}$, $\eta_c \approx \eta_{max}$).

The quartic solution finds the best-fit velocity profile (u_f) to the measured data. u_f can be written in terms of its non-dimensional form u^+ with the help of the bed shear velocity $u_b^\star$ as:

$$\frac{u_f(\eta)}{u_b^\star} = u^+(\eta) \tag{3.11}$$

Therefore, the bed shear velocity is used to provide a non-dimensional profile $u^+ = u/u_b^\star$. For example, the critical velocity at the critical depth η_c is non-dimensionalized as ($u_c^+ = u_c/u_b^\star$).

The main contribution of Guo et al., 2017 is that the dimensionless velocity profile (u^+) is suggested to follow the analytical solution:

$$u^+(\eta) = u_c^+ + \phi(\eta) \tag{3.12}$$

Here the velocity profile function ($\phi(\eta)$) is derived for infinitely long and straight channel as:

$$\phi(\eta,\lambda) = \frac{1}{\kappa}\{\ln(\frac{\eta}{\eta_c}) + \lambda \ln\frac{2-\eta}{2-\eta_c} - \frac{1+\lambda}{2}\ln[1+\alpha(1-\frac{\eta}{\eta_c})^2] - (1-\lambda^{n+1})\sqrt{\alpha}\tan^{-1}\sqrt{\alpha}(1-\frac{\eta}{\eta_c})\} \tag{3.13}$$

The shear velocity at the river bed can be calculated as:

$$u_b^\star = \frac{\sum_j \phi(\eta_j,\lambda)(u_j - u_c)}{\sum_j \phi^2(\eta_j,\lambda)} \tag{3.14}$$

The detailed steps for fitting the vertical velocity profile under the ice-covered condition with the ADCP data are as follows:

- *Step 1*: In each vertical location, the entire measurement points are selected from the value of $u(z)$ as discussed in Section 4.3.4. The number of available points along the depth is dictated by the measured cell size ($0.02 - 0.06$ m), which is automatically adjusted by the M9 sensor. Note that in each cross-section Ia, Ib, and Ie, there are two separate measurements $M1$ and $M2$ (2 minutes each) at every vertical location (see also Table 3.1). In such cases, the fitting procedure is performed on the averaged value of $M1$ and $M2$. Since the number of points along the depth can be slightly different between the first measurement $M1$ and the second measurement $M2$, we need to reconstruct the averaged profile of $M1$ and $M2$. First, the distance z is converted into the relative distance ($0 \leq \eta \leq 2$). The value of the entire depth is then divided into uniform intervals $N = 100$ in each vertical location as η_i ($i = 1 \rightarrow N$). For each measurement $M1$ or $M2$, a procedure is carried out to map the measured data $u(z_i)$ into the interpolated value $u(\eta_i)$ at the location η_i using the MATLAB function, "*interp1*" with piecewise cubic spline interpolation. Second, the averaged value of $\bar{u}(\eta_i)$ between the measurement $M1$ and $M2$ is finalized for further processing.

- *Step 2:* To further smooth out the variation of $\bar{u}(\eta_i)$ long the depth, a Fourier filtering method is performed on $\bar{u}(\eta_i)$ with the first 5 frequencies to obtain the filtered value $\widetilde{u(\eta_i)}$.
- *Step 3*: The location of the maximum velocity $\widetilde{u_{max}}$ in the vertical axis (η_{max}) is identified in this step. Since the value of η_{max} controls the fitting accuracy, it is important to investigate the sensitivity of the fitting procedure with η_{max} systematically. The value of η_{max} is varied within the 10% range.
- *Step 4*: The parameters λ and α are computed according to Equation 3.9 with the chosen value of η_{max}. The location of the critical position of the eddy viscosity (η_c) is computed from the Equation 3.10. To reduce the sensitivity of the fitting to process to the selection of η_{max}, the critical velocity is set to be equal to the maximum velocity ($u_c = \widetilde{u_{max}}$).
- *Step 6*: The velocity distribution function ($\phi(\eta_i)$) is computed by Equation 3.13.
- *Step 7*: The shear velocity at the river bed $u_b^\star$ is computed by Equation 3.14 using the values of $\widetilde{u_i}$ and u_c. The non-dimensional critical velocity is computed as $u_c^+ = \frac{u_c}{u_b^\star}$.
- *Step 8*: The non-dimensional velocity profile ($u^+(\eta_i)$) is produced by Equation 3.12.

- *Step 9*: The fitted velocity magnitude ($u_f(\eta_i)$) at the depth η_i is computed by Equation 3.11.
- *Step 10*: The correlation coefficient factor R^2 between the measured ($u(z)$) and fitted ($u_f(z)$) velocity profiles is computed. Record the dependence of the value R^2 on η_{max}.
- *Step 11*: Go back to Step 3. The iterative process will terminate until the highest correlation value R^2 is obtained with the selected η_{max}.

The fitting error is calculated using the RMSE criterion as follows:

$$RMSE = \sqrt{\frac{\sum_j^n (u_j - u_m)}{N_{obs}}} \tag{3.15}$$

Here, N_{obs} stands for number of observations along the depth while u_m is the corresponding value on the fitting curve.

3.4.6. Estimation of $u_b^\star$ from depth-averaged velocity (friction method)

The computation of boundary shear stress is a challenge since the ADCP is not able to measure accurately the flow velocities near the river bed due to side-lobe interference. This challenge leads to the use of depth-averaged velocity vector $\vec{U}(U_x, U_y)$ (Engel & Rhoads, 2016) to estimate $u_b^\star$ under open-surface condition. The procedure is as follows:

$$\begin{aligned} C_f &= [\alpha_r(\frac{H}{z_0})^{\frac{1}{6}}]^{-2} \\ \tau_{bx} &= \rho C_f U_x \sqrt{U_x^2 + U_y^2} \\ \tau_{by} &= \rho C_f U_y \sqrt{U_x^2 + U_y^2} \\ \tau_b &= \sqrt{\tau_{bx}^2 + \tau_{by}^2} \\ u_b^\star &= \sqrt{\frac{\tau_b}{\rho}} \end{aligned} \tag{3.16}$$

where, ρ, C_f, and z_0 are the fluid density, the friction coefficient, and the roughness height, respectively. The coefficient α_r is set equal to 8.1 (Parker, 1991). The equivalent roughness height z_0 is estimated as $2.95 \times d_{84}$ (Whiting & Dietrich, 1990).

The sediment characteristics of the Red River at Fargo have been well studied (Galloway & Nustad, 2012) by the United States Geological Survey (USGS). The particle-size distribution of the study area indicates that fine particles (silt) are the most found in the study area. The distribution shows that $d_{50} = 0.5$ mm.

The value of d_{84} is computed from the USGS field survey data as $d_{84} \approx 2.088$ mm (Blanchard et al., 2011; Galloway & Nustad, 2012). U_x and U_y are the two components of the depth-averaged velocity vector ($\vec{U}$) along the X and Y, respectively. The corresponding components of the magnitude shear stress (τ_b) are defined as τ_{bx} and τ_{by}. Since the depth-averaged velocity $\vec{U}$ is available for all vertical locations, this friction method can be applied anywhere. The Equation 3.16 indicates a direct correlation between $u_b^\star$ and U (Chauvet et al., 2014). The advantages and disadvantages of the logarithmic, quartic, and friction methods for computing shear velocity will be compared and contrasted.

3.4.7. Secondary flow visualization

The classical Rozovskii's method (Lane et al., 2000) is used to visualize the secondary flow pattern as shown in Figure 3.4A. The Cartesian components of the velocity u_x (East), u_y (North), and u_z (up) are used to derive the secondary components. The primary and the secondary flow components u_p and u_s are computed using the projections of the East and

North components on the depth-averaged velocity vector at the vertical:

$$u_p = (u_x^2 + u_y^2)^{0.5} \cos(\theta - \phi) \tag{3.17}$$

$$u_s = (u_x^2 + u_y^2)^{0.5} \sin(\theta - \phi) \tag{3.18}$$

Here ϕ and θ are defined as the angle between the depth-averaged vector U and the time-averaged vector u to the x (East) direction in the counter-clockwise direction. The components u_s and the u_z are used to visualize the secondary flow pattern.

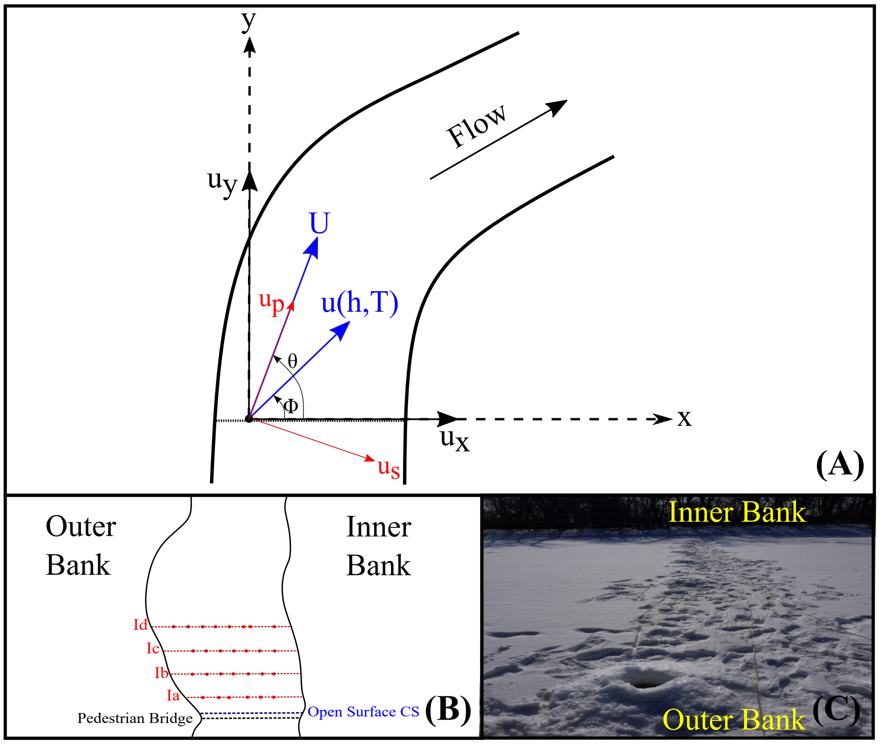

Figure 3.4. **(A)** The schematic diagram of the Rozovskii method. The degree of ϕ represents the orientation of time-averaged velocity, and θ is the degree of the depth-averaged velocity to the positive x axis. **(B)** The diagram shows the ice holes in five consecutive cross-sections Ia, Ib, Ic, Id and Ie in Feb/2021. The number of ice holes for each cross-section is shown in Table 3.1. Each vertical location in one cross-section is marked by its distance from the corresponding left bank ℓ (m) (see also Figure 3.3). **(C)** Cross-sectional view of the river and ice holes next to the pedestrian bridge (Feb/19/2021).

3.5. Result

As the measured cross-sections are in a meandering bend, the impact of the channel curvature is significant. This effect is presented using the depth-averaged velocities U under open-surface condition as shown in Figure 3.3. Overall, the depth-averaged profiles are asymmetrical toward the outer bank. At high discharges (Oa and Ob), the maximum velocity is visible in the left part of the thalweg. Note that $Q_{Oa} \approx Q_{Ob}$ and thus the velocity profiles of Oa and Ob are closely similar. At low flow conditions (Oc, Od, and Oe), such an asymmetry is not distinct as the flow in the thalweg is nearly uniform. In the following sections, the characteristics of the vertical profiles will be examined at each location ℓ in the cross-sections. First, the statistical analysis is carried out to determine if the measured data is sufficient to generate reliable values for U and $u(z)$. Second, the validity of the logarithmic law is examined under open-surface condition. Third, the presence of the double log-law is investigated for the ice-covered cases. Fourth, we revisit the quartic solution and its applicability to derive shear velocity for ice-covered condition in the current study. Finally, we address the changes in secondary flow patterns under the impacts of the ice cover.

3.5.1. Data statistics

Under open-surface condition, the results show that the value of the time-averaged velocity $u(h,T)$ at all locations h along the depth does depend on the averaging period T. Figure 3.5 illustrates that the $u(h,T)$ mostly oscillates near the free surface ($h = 0.26$ m) and the bed ($h = 3.44$ m) at the stations of Oa_5 and Ob_5, especially when $T < 200$ seconds. Despite the continuous oscillations even after the $T = 200$ seconds, they remain in the 5% of u_∞ range. In particular, $u(h,T)$ converges to its long-term values $u_\infty(h)$ within ±5% in the first 100 seconds. The value at the mid-depth $u(h = 1.82$ m,T) converges even more quickly to the long-term value. In contrast to the time-average velocity, the depth-averaged $U(T)$ converges rapidly to its long-term value U_∞ without any significant oscillation within the first minute. As shown in Figure 3.3, the obtained depth-averaged profiles of Oa and Ob are consistent given closely similar flow discharges. A similar observation is applied for Oc and Od. In brief, the period $T \approx 200$ seconds is sufficient for the time-averaged profile $u(h,T)$ and depth-averaged $U(T)$ to attain their accuracy within ±5% of their long-term values.

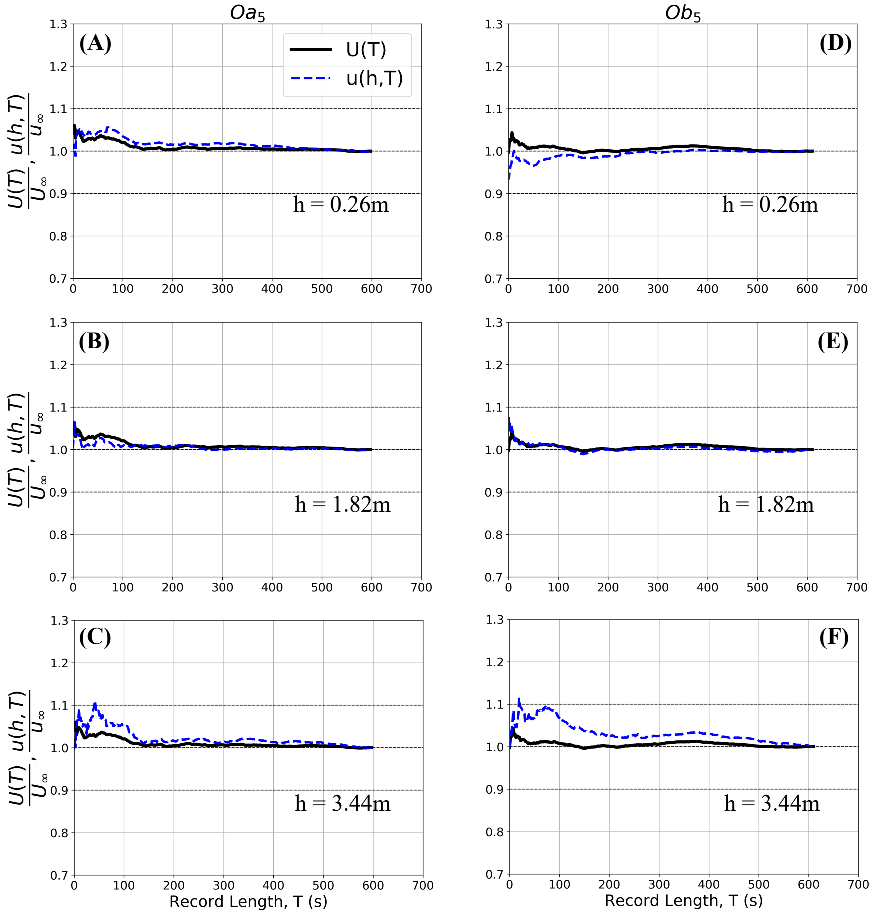

Figure 3.5. Statistical convergence properties for the depth-averaged velocity $U(T)$ and the time-averaged velocity $u(h,T)$ (section 4.3.4) as the function of the record length T for the vertical location Oa_5 (left column - $H_{Oa_5} = 4.1$ m) and Ob_5 (right column - $H_{Ob_5} = 4.1$ m). The record length T is varied from 1 second to the entire record ($T_\infty \approx 600$ seconds). The long-term values of $U(T_\infty)$ and $u(h,T_\infty)$ are denoted as U_∞ and $u_\infty(h)$, respectively. Three values of depth are chosen $h = 0.26$ m (near surface), $h = 1.82$ m (mid-depth), and $h = 3.44$ m (near bed).

The variation of the vertical velocity profile $u(h, T)$ under different periods of averaging T is shown in Figure 3.6. To examine the convergence of the vertical profiles as a function of the period T, four different periods are selected: $D-1$ ($t = 0 \rightarrow 120$ seconds) ; $D-2$ ($t = 200 \rightarrow 320$ seconds); $D-3$ ($t = 0 \rightarrow 400$ seconds); and $D-4$ ($t = 0 \rightarrow 620$ seconds) for the verticals Oa_5 (Figure 3.6A) and Oc_6 (Figure 3.6B). In both Oa_5 and Oc_6, there exists a significant complex flow profile near the free surface ($h < 1.5$ m). In this region, the shape of the vertical profile is significantly dependent on the averaging period T. Comparing the period $D-1$ and $D-2$, which last 120 seconds, the time-averaged profiles ($u(h, T)$) are significantly different, especially in the near surface region. In the near bed region ($h > 2$ m), the shape of the profile is less sensitive to the choice of the period T. Indeed, the profile ($u(h, T)$) becomes nearly identical between $D-3$ and $D-4$ when the value of T is extended to 620 seconds. In other vertical locations, the convergence of velocity profiles is similar to ones as seen in Figure 3.6. Therefore, a period of 600 seconds (10 minutes) is sufficient to obtain the velocity profile convergence under open-surface condition.

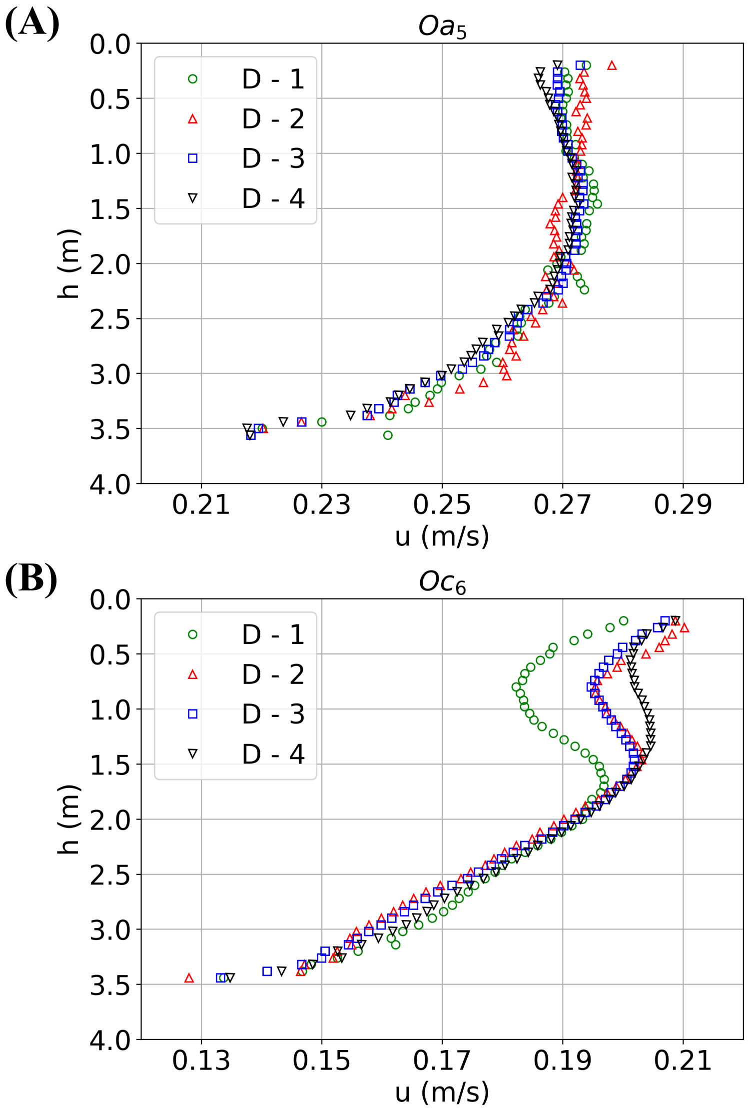

Figure 3.6. The variability of the vertical flow profile as the record length T changes at the vertical location Oa_5 and Oc_6. Four periods ($D-1$, $D-2$, $D-3$, and $D-4$) with different values of measurement period T (seconds) are examined: $D-1$ ($t = 0 \rightarrow 120$ seconds); $D-2$ $t = 200 \rightarrow 320$ seconds; $D-3$ ($t = 0 \rightarrow 400$ seconds; and ($D-4$) $t = 0 \rightarrow 620$ seconds. The vertical flow profile near the river bed converges rapidly in the first 120 seconds.

The impacts of T value on the three-dimensional flow pattern can be examined using the East (u_E - x) and Up (u_{up} - z) components as shown in Figure 3.7 (the vertical Oa_8). Note that the magnitudes of u_E and u_{up} are one order of magnitude smaller than the u_N. Hence, any dependence of three-dimensional flow pattern on the duration T can be reflected easily in u_E and u_{up} components. Different values of T, which correspond to four subsets with different periods $D-1$, $D-2$, $D-3$, and $D-4$, are tested. As seen in Figure 3.7, the structure of the circulatory vortex is consistent across all averaging periods $D-1$, $D-2$, $D-3$, and $D-4$. Thus, the 10-minute record ensures that the three-dimensional flow structure is captured accurately.

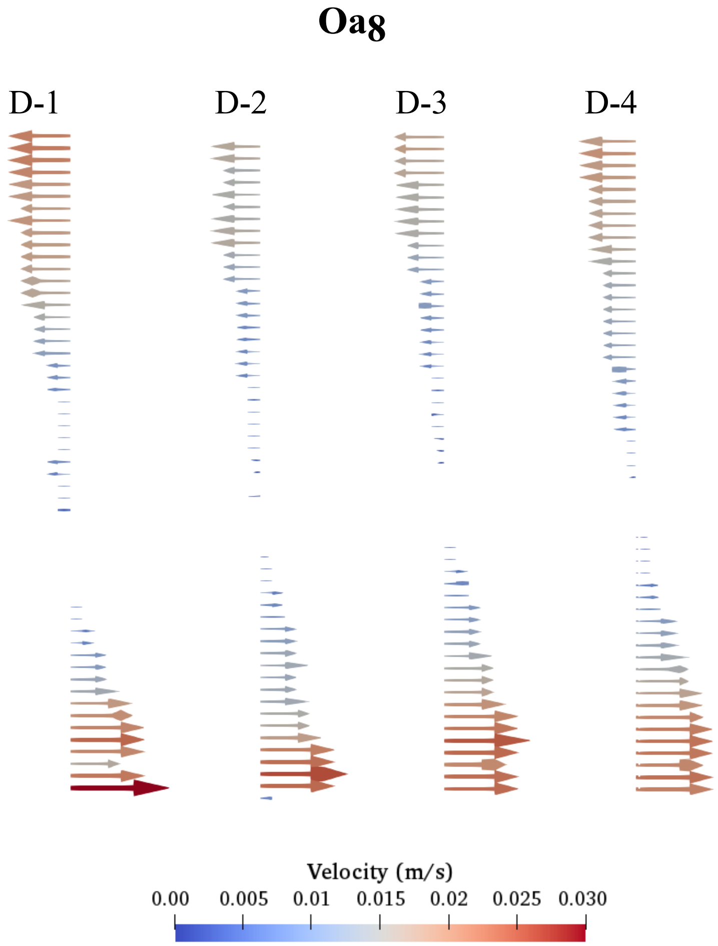

Figure 3.7. The sensitivity of the flow pattern $(u_x(T_\infty), u_z(T_\infty))$ to the length of the averaging period T (section 3.5.1). The flow patterns are consistent across different scenarios of: $(D-1)$ $t = 0 \rightarrow 120$ s ($T = 120$ s); $(D-2)$ $t = 200 \rightarrow 320$ s ($T = 120$ s); $(D-3)$ $t = 0 \rightarrow 400$ s ($T = 400$ s); and $(D-4)$ $t = 0 \rightarrow 620$s ($T = 620$ s). The center of the rotation is found closer to the bed.

Under the ice-covered condition in Figure 3.8, the total length of the measurement period T_∞ is limited to approximately 120 seconds. Therefore, there exists a larger variation of $U(T)$ and $u(h,T)$ from their respective long-term values. As seen in Figure 3.8, two independent measurements ($M1$ and $M2$) of the same ice hole Ib_7 at the depth $h = 1.64$ m are shown. The ratios $\frac{U(T)}{U_\infty} \geq 10\%$ and $\frac{u(h,T)}{u_\infty(h)} \geq 20\%$ for both $Ib_7 - M1$ and $Ib_7 - M2$ at the early stage from $T = 0$ to $T = 100$ seconds. Here, it is seen that the stabilization of $u(h,t)$ and $U(T)$ can only attain when $T > 100$ seconds. For other ice holes, their running statistics also show a similar behavior. There exist a significant variation of $\frac{U(T)}{U_\infty}$ and $\frac{u(h,T)}{u_\infty(h)}$ within ±10% in the first minute. The values of $U(T)$ and $u(h,T)$ converge in a synchronous fashion only when $T > 100$ seconds. In brief, it is evident that the duration of measurement $T = 120$ seconds has a significant impact on the velocity profiles.

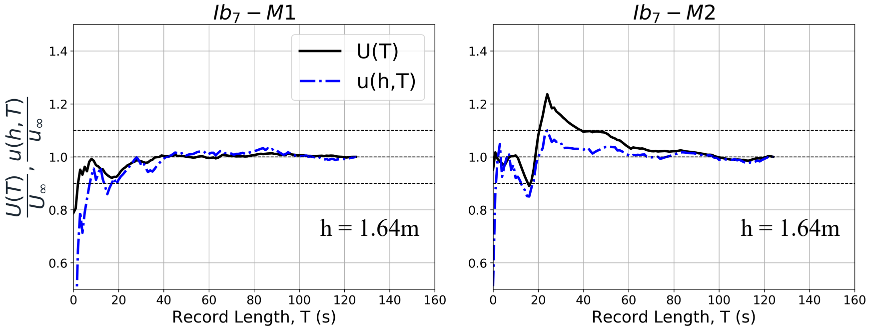

Figure 3.8. Statistical properties of the depth-averaged velocity $U(T)$ and the time-averaged velocity $u(h,T)$ under ice-covered condition as the function of the record length $T(s)$. Two measurements ($M1$ and $M2$) of same station Ib_7 are shown at the depth $h = 1.64$ m. Here the sample length T is varied from 1 second to the entire record ($T_\infty = 120$ seconds). The long-term values of $U(T_\infty)$ and $u(h,T_\infty)$ are denoted as U_∞ and $u_\infty(h)$, respectively.

To examine the variability of the vertical profile due to a short period of measurement $T = 120$ seconds, the vertical profiles at the vertical Ib_7 in two consecutive measurements ($M1$ and $M2$) are plotted in Figure 3.9A. The results show that the overall vertical profiles of both measurements are consistent. However, the depth-averaged velocities are significantly different ($U_{M1} = 0.1591$ m/s and $U_{M2} = 0.1967$ m/s). To further investigate the variation of the derived shear velocity, the logarithmic fitting is carried out for the bed and the ice layer in Figure 3.9B and 3.9C, respectively. There exists a significant difference in the value of $u_b^\star$ between the two measurements ($u_b^\star(M1) = 0.0352$ m/s and $u_b^\star(M2) = 0.0477$ m/s). However, the value of $u_i^\star$ does not vary significantly ($u_i^\star(M1) = 0.0269$ m/s and $u_i^\star(M2) = 0.0255$ m/s). Moreover, the separation from logarithmic profile initiates at $h^+ \approx 10,251$ in the first measurement ($M1$), while it is $h^+ \approx 9,693$ in the second measurement ($M2$). This behavior is consistent with the convergence characteristics as shown in Figure 3.8 where the two measurements exhibit slightly different convergence profiles. Recognizing this limitation, we use the averaged profile resulting from two measurements ($M1$ and $M2$).

3.5.2. The universality of the logarithmic law under open-surface condition

Under the open-surface condition, the logarithmic fitting is summarized in Table 3.2. The presence of the logarithmic law is validated in most measurements of Oa, Ob, Oc, Od, and Oe with high degree of agreement ($R^2 \geq 90\%$) in the thalweg. Location of each vertical is indicated under the column "ℓ (m)", as the distance from the outer bank. It can be observed in Table 3.2 that the logarithmic law is observed in all sufficiently deep locations ($H \geq 3.5$ m). In these locations, the logarithmic layer (δ_b) remains in 20% of the total depth ($\delta_b \approx 20\% H$). In most of the stations, the logarithmic layer can extend up to approximately 50% of the total depth. Therefore, the law of the wall is considered applicable for most locations in the bend thalweg regardless of the flow discharge.

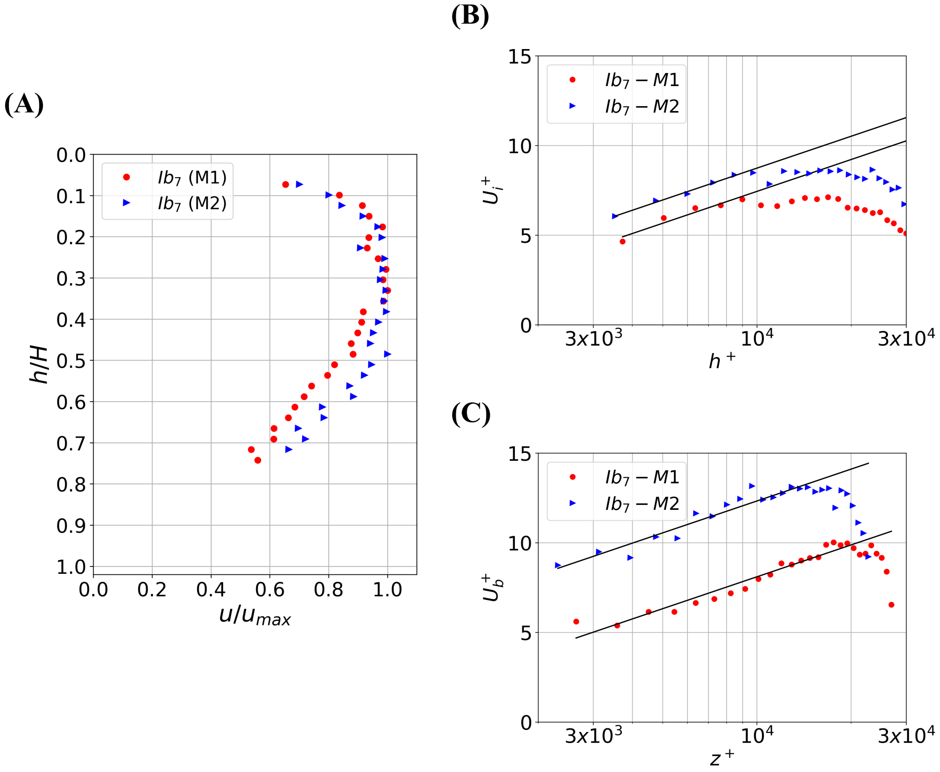

Figure 3.9. The presence of the logarithmic profile (solid lines) for two consecutive measurements under ice-covered flows. **(A)** Non-dimensional time-averaged velocity profiles of the first and the second measurement at vertical Ib_7. **(B)** on the ice layer at the vertical Ib_7; and **(C)** on the bed layer. The logarithmic law (Equation 4.3) is written in wall units (see Equation 4.6 and Equation 4.7). The separation from the logarithmic law determines the value of the logarithmic layer thickness δ_i^+ and δ_b^+.

To further examine the universality of the logarithmic law, the extension of the logarithmic layer is presented in Figure 3.10 in terms of wall units. Three vertical locations are shown in different measurement dates as Oc_4, Od_7, and Oe_5. The measured data fit excellently well with the logarithmic law as evidenced by the correlation between the $u^+(z^+)$ and z^+ for these cases in the range of $4000 \leq z^+ \leq 10,000$. However, the separation from the logarithmic law initiates at different values of z^+ depending on the profile. For example, the separation starts at $z^+ \approx 15,000$ for the case Oc_4 and Oe_5. However, it starts much later at $z^+ \approx 20,000$ for the case Od_7. Here the value of the shear velocity $u_b^\star$ is found to vary

Table 3.2. Derivation of the shear velocity $u_b^\star$ and the equivalent roughness height (z_0) using the logarithmic fitting (section 3.4.4) for the case *Oa*, *Ob*, *Oc*, *Od*, and *Oe* (see Table 3.1). The friction Reynolds number Re_τ^b and the thickness of the logarithmic layer δ_b^+ are explained in Equation 4.6. The theoretical bound for δ_{theory}^+ is computed from Equation 3.3. Only the stations in the thalweg region ($H \geq 3.5$ m) are listed in this table.

Case	ℓ (m)	H (m)	$\frac{\delta_b}{H}$	R^2	$u_b^\star$ (m/s)	z_0 (m)	Re_τ	δ_b^+	δ_{theory}^+
Oa_4	16.15	3.66	0.50	0.99	0.0150	0.061	57,876	28,938	8,681
Oa_5	20.12	4.10	0.50	0.94	0.0136	0.0245	55,883	27,941	8382
Oa_{10}	34.14	3.83	0.50	0.95	0.0090	0.014	34,453	17,226	5,168
Ob_5	19.51	4.10	0.50	0.91	0.0087	0.0003	35,549	17,774	5,332
Ob_6	22.53	4.20	0.30	0.95	0.0079	1.5×10^{-4}	24,613	7,384	3,692
Ob_7	25.60	4.23	0.20	0.99	0.0095	9.7799	57,067	11,413	8,560
Ob_8	28.65	3.99	0.20	0.99	0.0125	0.0365	12,428	2,485	1,864
Ob_9	31.70	3.82	0.20	0.98	0.0124	0.1006	27,596	5,519	4,139
Oc_2	10.36	3.50	0.50	0.99	0.0069	0.0001	24,147	12,073	1,811
Oc_4	16.15	3.95	0.35	0.99	0.0070	0.0188	32,142	11,249	4,821
Oc_5	19.51	4.06	0.20	0.99	0.00796	0.0195	26,764	5,352	4,015
Oc_6	23.16	3.95	0.50	0.98	0.01557	0.4489	61,531	30,765	9,230
Oc_7	28.35	3.65	0.45	0.97	0.0121	0.4760	46,680	21,006	7,002
Od_3	11.89	3.64	0.50	0.99	0.0122	0.5166	44,313	22,156	3,323
Od_4	14.02	3.88	0.40	0.98	0.0078	0.4182	33,176	13,270	4,976
Od_5	16.15	4.09	0.50	0.96	0.0121	0.5056	49,544	24,772	7,431
Od_6	19.20	4.22	0.40	0.97	0.0107	0.4165	51,227	20,491	7,684
Od_7	22.25	4.10	0.50	0.98	0.0109	0.2300	44,573	22,286	6,686
Od_8	24.38	3.80	0.50	0.96	0.0089	0.0570	33,914	16,957	5,087
Od_9	26.52	3.60	0.50	0.93	0.0096	0.2257	34,722	17,361	5,208
Od_{10}	28.65	3.70	0.45	0.99	0.0131	1.2623	49,931	22,469	7,490
Oe_2	15.85	4.01	0.50	0.94	0.0124	2.0462	49,601	24,800	7,440
Oe_3	18.90	4.03	0.35	0.98	0.0088	1.1045	43,687	15,290	6,595
Oe_4	20.42	4.05	0.45	0.96	0.0110	2.2522	47,432	21,344	7,115
Oe_5	23.47	3.76	0.50	0.94	0.0089	0.6461	33,410	16,705	5,011

around 0.01 m/s. Consequently, the local value of Re_τ^b (Equation 4.6) varies from $8,000$ to $60,000$. As shown in the Table 3.2, the logarithmic layer (δ_b^+) obeys the theoretical limit (Equation 3.3) excellently well with $\delta_b^+ \geq \delta_{theory}^+$ for all cases.

There are vertical locations that do not follow the logarithmic law (Oa_6, Oa_7, Oa_8, Oa_9, Ob_4, Oc_3). In these profiles, it is impossible to perform the logarithmic fitting with the listed constraints in section 3.4.4. They are mostly located near the inner and outer banks where the secondary flows are strong. The deviation of the velocity profiles of these locations from the logarithmic law will be discussed in section 3.5.5.

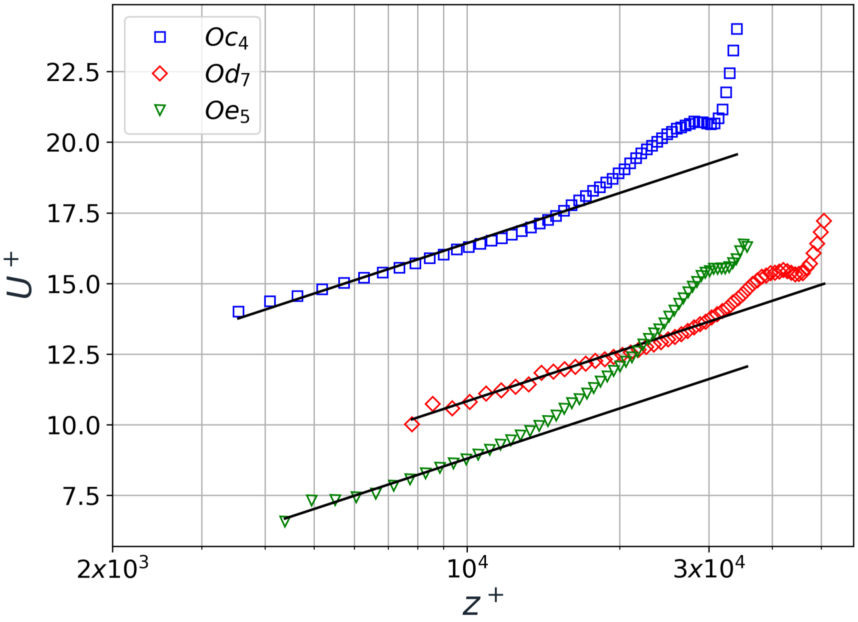

Figure 3.10. The presence of the logarithmic law (solid lines) at three vertical locations Oc_4 (blue circle), Od_7 (green triangle), Oe_5(red diamond) under open-surface condition (see Table 3.1). The logarithmic law (Equation 4.3) is written in wall units (see Equation 4.6). The separation from the logarithmic law determines the value of the logarithmic layer thickness δ_b^+. The logarithmic layer is considered as a collection of measured points near the river bed so that the value fitting of $R^2 \geq 0.9$ (see section 3.4.4).

3.5.3. The double log-law under ice-covered condition

In contrast to the open-surface condition, the presence of the logarithmic layer is found using the criteria in section 3.4.4 only in limited locations near the bed as shown in Table 3.3. In those locations, the logarithmic layer δ_b extends well beyond 20% and up to 50% of H. Interestingly, the value of $u_b^\star$ is found to be significantly larger near banks $u_b^\star \approx 0.04$ m/s (Ib_7 and Id_8) than ones in the thalweg region (Ia_6, Ib_2, Ib_6, Ic_2, Id_6) in which $u_b^\star$ varies around 0.01 m/s. In brief, the data confirm the presence of the logarithmic layer near the river bed in a limited number of ice holes.

Table 3.3. Derivation of the shear velocity $u_b^\star$ and the equivalent roughness height (z_0) using the logarithmic fitting (section 3.4.4) for the case Ia, Ib, Ic, and Id (see Table 3.1). The friction Reynolds number Re_τ and the thickness of the logarithmic layer δ_b^+ are explained in Equation 4.6. The theoretical bound for δ_{theory}^+ is computed from Equation 3.3.

Case	ℓ (m)	H (m)	$\frac{\delta_b}{H}$	R^2	$u_b^\star$ (m/s)	z_0 (m)	Re_τ	δ_b^+	δ_{theory}^+
Ia_6	33.83	1.93	0.40	0.9734	0.0161	1.8574	31,088	13,990	4,663
Ib_2	13.53	3.11	0.50	0.9158	0.0128	0.1205	40,001	16,000	6,000
Ib_6	31.82	2.60	0.35	0.9418	0.0137	0.1364	35,623	8,905	5,343
Ib_7	36.39	2.33	0.50	0.9478	0.0477	5.6604	111,125	38,893	16,669
Ic_2	14.63	3.50	0.50	0.9162	0.0102	0.0538	29,113	14,556	4,367
Id_2	12.04	3.43	0.50	0.9620	0.0170	0.998	47,217	23,608	7,083
Id_6	30.33	3.42	0.50	0.9206	0.0089	0.0247	24,773	12,386	3,716
Id_8	39.47	1.65	0.45	0.9921	0.0203	1.5292	26,143	11,764	3,921

The logarithmic layer near the ice cover is found in a larger number of vertical stations as shown in Table 3.4 in all cross-sections Ia, Ib, Ic, Id and Ie. In these locations, the logarithmic layer extends mostly up to 20% of the total depth H in general. However, the value of the shear velocity $u_i^\star$ is generally lower than 0.01 m/s. In short, the applicability of the logarithmic law for the ice layer is different from the river bed layer.

Following the fitting procedure, lower and upper limits of $u^\star$ and z_0 are investigated using a 95% confidence limit as shown in Table 3.5 for both the ice and bed layers. On one hand, the results show that the confidence interval for $u^\star$ in bed and ice layers are in the order of 0.008 m/s, except verticals close to the banks (e.g., Ia_1). On the other hand, the confidence interval of z_0 is unrealistically large in both ice and bed layers.

The thickness of the logarithmic layers in wall units (δ_i^+ and δ_b^+) for applicable ice holes are summarized in Table 3.3 and Table 3.4 for the bed and the ice layer, respectively.

Table 3.4. Derivation of the shear velocity $u_i^\star$ and the equivalent roughness height (z_0) using the logarithmic fitting (section 3.4.4) for the case *Ia*, *Ib*, *Ic*, and *Id* (see Table 3.1). The friction Reynolds number Re_τ^i and the thickness of the logarithmic layer δ_i^+ are explained in Equation 4.6. The theoretical bound for δ_{theory}^+ is computed from Equation 3.3.

Case	ℓ (m)	H (m)	$\frac{\delta_i}{H}$	R^2	$u_i^\star$ (m/s)	z_0 (m)	Re_τ	δ_i^+	δ_{theory}^+
Ia_1	8.84	1.72	0.30	0.9033	0.0213	2.0291	29,706	8,912	4,455
Ia_4	23.77	3.46	0.20	0.9499	0.0117	0.0767	33,374	6,675	5,006
Ia_5	28.35	3.39	0.30	0.9276	0.0197	0.7907	27,459	8,238	4,118
Ib_4	22.68	4.01	0.20	0.9174	0.0083	0.0007	27,177	5,435	4,076
Ib_5	27.25	3.68	0.30	0.9837	0.0078	0.0023	23,455	7,037	3,518
Ib_7	36.39	2.33	0.20	0.9921	0.0255	0.4402	48,465	9,693	7,269
Ic_1	10.06	3.04	0.25	0.9262	0.0120	0.4061	30,021	7,505	4,503
Ic_3	19.20	3.74	0.20	0.9398	0.0066	0.0001	21,242	4,248	3,186
Ic_5	28.35	3.48	0.35	0.9630	0.0053	0.0001	15,101	5,285	2,265
Id_2	12.04	3.43	0.25	0.9852	0.0089	0.0117	24,838	6,209	3,725
Id_3	16.61	3.57	0.20	0.9404	0.0041	1×10^{-7}	11,917	2,383	1,787
Id_5	25.76	3.74	0.30	0.9716	0.0053	1×10^{-5}	15,978	4,793	2,396
Id_6	30.33	3.42	0.25	0.9663	0.0070	0.0011	19,543	4,886	2,931
Id_8	39.47	1.65	0.30	0.9845	0.0049	0.0001	6,591	1,977	988
Ie_2	9.14	2.54	0.30	0.9860	0.0101	0.0392	20,941	6,282	3,141
Ie_5	22.86	4.41	0.40	0.9322	0.0044	0.0001	15,930	6,372	2,389
Ie_7	32.00	3.04	0.20	0.9539	0.0034	4.5×10^{-5}	8,313	1,662	1,246

Table 3.5. The accuracy of the logarithmic fitting. The lower and upper limits of $u^\star$ and z_0 for the ice and bed layers in representative verticals according to 95% confidence level.

Case	H (m)	$u_{lo}^\star$ (m/s)	$u^\star$ (m/s)	$u_{up}^\star$ (m/s)	z_0^{lo} (m)	z_0 (m)	z_0^{up} (m)
Oc_2 (bed)	3.50	0.0065	0.0069	0.0073	4.28×10^{-5}	0.0001	0.0003
Ob_5 (bed)	4.10	0.0079	0.0087	0.0095	0.0002	0.0003	0.0004
Ib_7 (bed)	2.33	0.0401	0.0477	0.0553	4.0442	5.6604	7.2766
Id_6 (bed)	3.42	0.0076	0.0089	0.0102	0.0044	0.0247	0.0450
Id_8 (bed)	1.65	0.0192	0.0203	0.0214	0.2415	1.5292	2.8169
Ia_1 (ice)	1.72	0.0116	0.0213	0.0310	0.6902	2.0291	3.3680
Ib_5 (ice)	3.68	0.0072	0.0078	0.0084	0.0008	0.0023	0.0038
Ib_7 (ice)	2.33	0.0213	0.0255	0.0297	0.2339	0.4402	0.6465
Ic_5 (ice)	3.48	0.0048	0.0053	0.0059	2.5×10^{-5}	0.0001	0.0002
Id_8 (ice)	1.65	0.0040	0.0049	0.0058	3×10^{-6}	0.0001	0.0002

Here, the theoretical bounds (Equation 3.3) are well below the measured values of δ_i^+ and δ_b^+.

Thus, the Equation 3.3 is effective in predicting the potential thickness of the logarithmic layer under ice coverage.

3.5.4. The applicability of quartic profiles for ice-covered flows

Overall, the profiles in almost all ice holes follow closely the quartic solution as shown in Figure 3.11 and Table 3.6 following the fitting procedure as discussed in section 3.4.5. Surprisingly, the quartic solution works well even in the shallow parts of banks (Id_2 and Id_7 in Figure 3.11, for example). In particular locations (Ia_5 and Id_2), the existence of the maximum velocity u_{max} is evident. However, it is not straightforward to assign a unique value of u_{max} in the time-averaged velocity profile for other cases. Here, the optimization of R^2 (see section 3.4.5) is useful in justifying the value of η_{max}. As shown in Table 3.6, the u_{max} location does not typically coincides to the symmetry plane ($\eta = 1$). Rather, the value of η_{max} is frequently greater than 1 and indicates that the maximum velocity appears closer to the ice layer. The asymmetry of the velocity profile is also evident as the value of $\lambda = \frac{u_i^\star}{u_b^\star}$ is mostly less than 1 as shown in Table 3.6. Therefore, the data supports the general use of the quartic form for ice-covered flow profiles in rivers. The value of Root Mean Square Error (RMSE) and Absolute Error (AE) are computed for the discrepancy between the quartic solution and the observation at each vertical (see Figure 3.11). Results show that the error is approximately 5% of the value of u_{max} as shown in Figure 3.12.

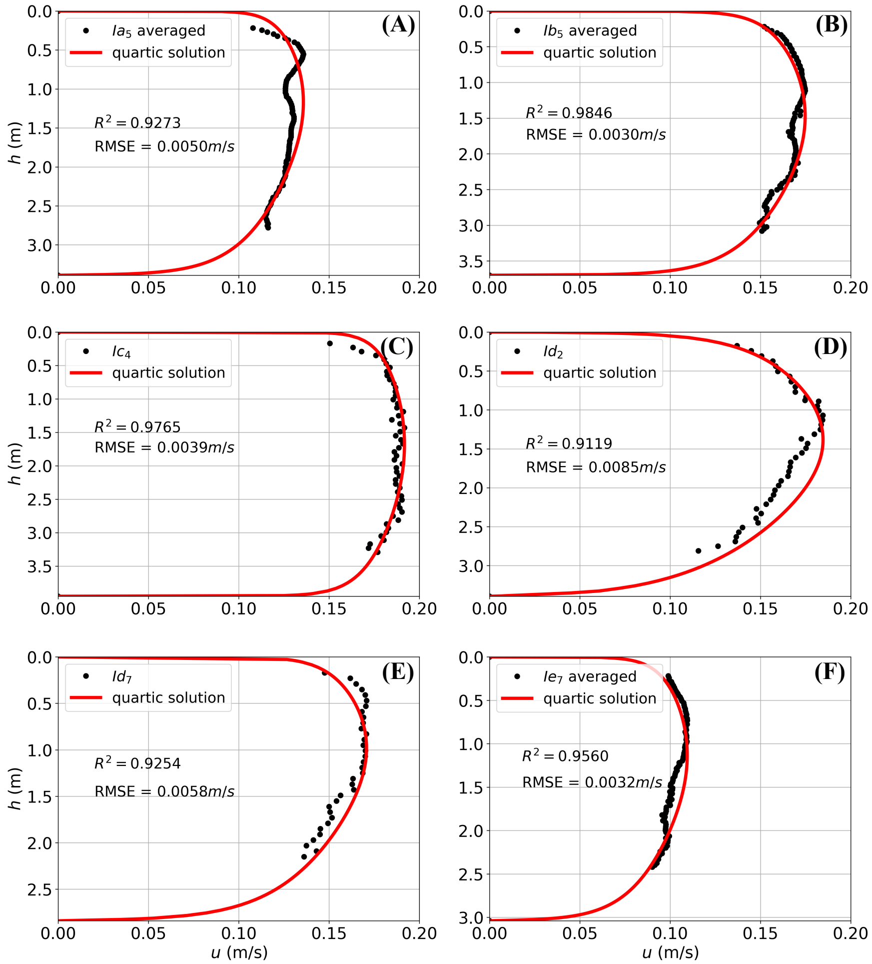

Figure 3.11. The agreement between the measured profiles and the quartic solution. The fitting procedure provides the shear velocity on the river bed ($u_b^\star$) and the ice layer ($u_i^\star$) in section 3.4.5. The details of the available data are described in Table 3.6 for all ice holes. The averaged profile (from two measurements M1 and M2) is used for the cross-sections Ia, Ib, and Ie. The discrepancies between the model and the observations are computed with RMSE.

3.5.5. The structures of secondary flow

Under open-surface condition, results show the signature of a classical circulation in the bridge cross-section under high discharge (Oa and Ob) as shown in Figure 3.13A (upper panel). On Oa, the secondary flow contains a large vortex occupying the thalweg area from the river bed to the free surface. In Ob, the secondary vortex is closer to the bed. This

Table 3.6. Derivation of the shear velocity on the ice layer ($u_i^\star$) and the bed layer ($u_b^\star$) using the quartic solution (section 3.5.4) for the case Ia, Ib, Ic, and Id (see Table 3.1). The local Reynolds number based on shear velocity $u_b^\star$ and water viscosity ν is Re_τ (see equation 4.6). The location (η_{max}) and the maximum velocity (u_{max}) are determined by the iterative procedure in section 3.5.4.

Case	ℓ (m)	H (m)	u_{max} (m/s)	R^2	$u_b^\star$ (m/s)	$u_i^\star$ (m/s)	λ	η_{max}
Ia_2	14.33	3.14	0.1451	0.9184	0.0012	0.0016	1.3234	0.7269
Ia_5	28.35	3.39	0.1357	0.9273	0.0073	0.0032	0.4422	1.6729
Ib_2	13.53	3.11	0.1998	0.9916	0.0078	0.0062	0.7886	1.2331
Ib_4	22.68	4.01	0.2115	0.9748	0.0074	0.0048	0.6428	1.4153
Ib_5	27.25	3.70	0.1747	0.9846	0.0074	0.0049	0.6564	1.3977
Ib_6	31.82	2.60	0.1599	0.9795	0.0023	0.0030	1.3067	0.7387
Ib_7	36.39	2.33	0.2036	0.9828	0.0293	0.0193	0.6596	1.3937
Ic_2	14.63	3.50	0.1926	0.9746	0.0071	0.0034	0.4825	1.6223
Ic_4	23.77	3.95	0.1917	0.9765	0.0045	0.0034	0.7535	1.2756
Ic_5	28.35	3.48	0.1844	0.9383	0.0064	0.0050	0.7784	1.2454
Id_2	12.04	3.43	0.1846	0.9119	0.0143	0.0097	0.6777	1.3706
Id_3	16.61	3.57	0.1983	0.9560	0.0075	0.0033	0.4372	1.6791
Id_4	21.18	3.95	0.2023	0.9733	0.0060	0.0023	0.3879	1.7384
Id_5	25.76	3.74	0.1934	0.9812	0.0057	0.0035	0.6142	1.4521
Id_6	30.33	3.42	0.1843	0.9295	0.0084	0.0066	0.7912	1.2300
Id_7	34.90	2.84	0.1707	0.9254	0.0103	0.0046	0.4453	1.6690
Id_8	39.47	1.65	0.1476	0.9380	0.0121	0.0076	0.6305	1.4310
Ie_1	4.57	0.65	0.0839	0.9486	0.0022	0.0020	0.9009	1.1040
Ie_2	9.14	2.54	0.1551	0.9631	0.0088	0.0064	0.7290	1.3059
Ie_3	13.72	3.78	0.1741	0.9781	0.0056	0.0033	0.5836	1.4919
Ie_4	18.29	4.46	0.1596	0.9485	0.0044	0.0021	0.4776	1.6285
Ie_7	32.00	3.04	0.1094	0.9560	0.0063	0.0035	0.5624	1.5194

circulation rotates in the clockwise direction (Oa_{4-12} and Ob_{4-12}). In Oa, the center of this circulation locates near the vertical Oa_6 to Oa_9. In Ob, the circulation locates at the vertical Ob_6. In other words, the location of the circulation center is sensitive to the change in flow discharge. In addition to the main circulation, the presence of the outer bank cell is also evident in both Oa and Ob.

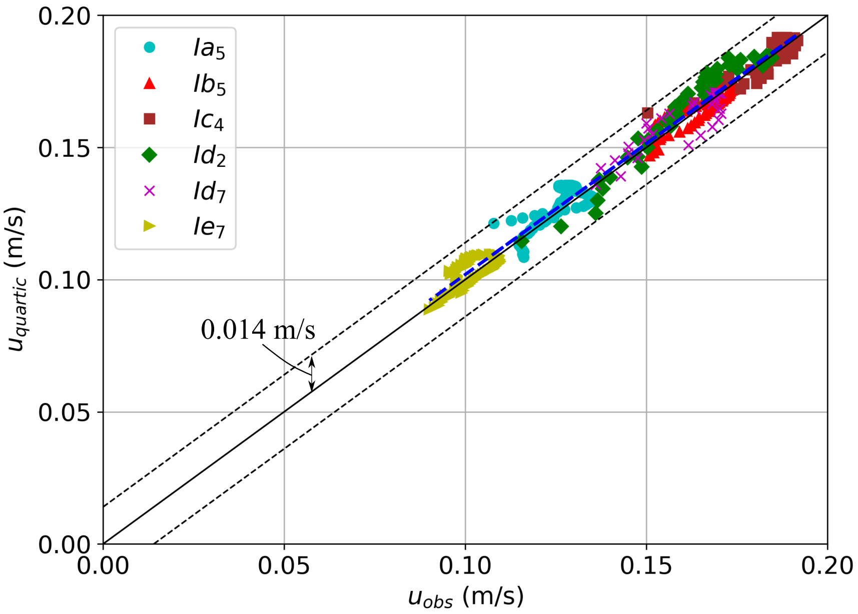

Figure 3.12. Error analysis of profile fitting using the quartic solution for Ia_5, Ib_5, Ic_4, Id_2, Id_7, and Ie_7. The observed values (u_{obs}) are plotted against the fitted results ($u_{quartic}$). The line of perfect agreement is shown in black. The linear regression line is displayed by a blue dashed line, which shows a good agreement between the observed and fitted data. The maximum absolute errors are shown indicating the upper and lower bound errors of $0.014(m/s)$.

Under lower discharges in Oc, Od, and Oe, the secondary flow structure completely changes. The main circulation (clockwise) becomes weaker in the thalweg (Oc_6, Od_{7-8}, and Oe_3). The main circulation moves toward the center of the thalweg as the discharge decreases (Oc, Od, and Oe - see Table 3.1) as shown in Figure 3.13 (lower panel). There exist two additional (counterclockwise) circulations near the outer and inner banks. The extensions of these circulations are significantly large as shown in Oc_{1-4}, Oc_{7-8}, Od_{1-5}, and Od_{9-11}. Three circulations are visible in both Oc and Od and roughly the same size. In brief, the migration of the main circulation is significant as the water level reduces due to the presence of the outer and inner-bank cells.

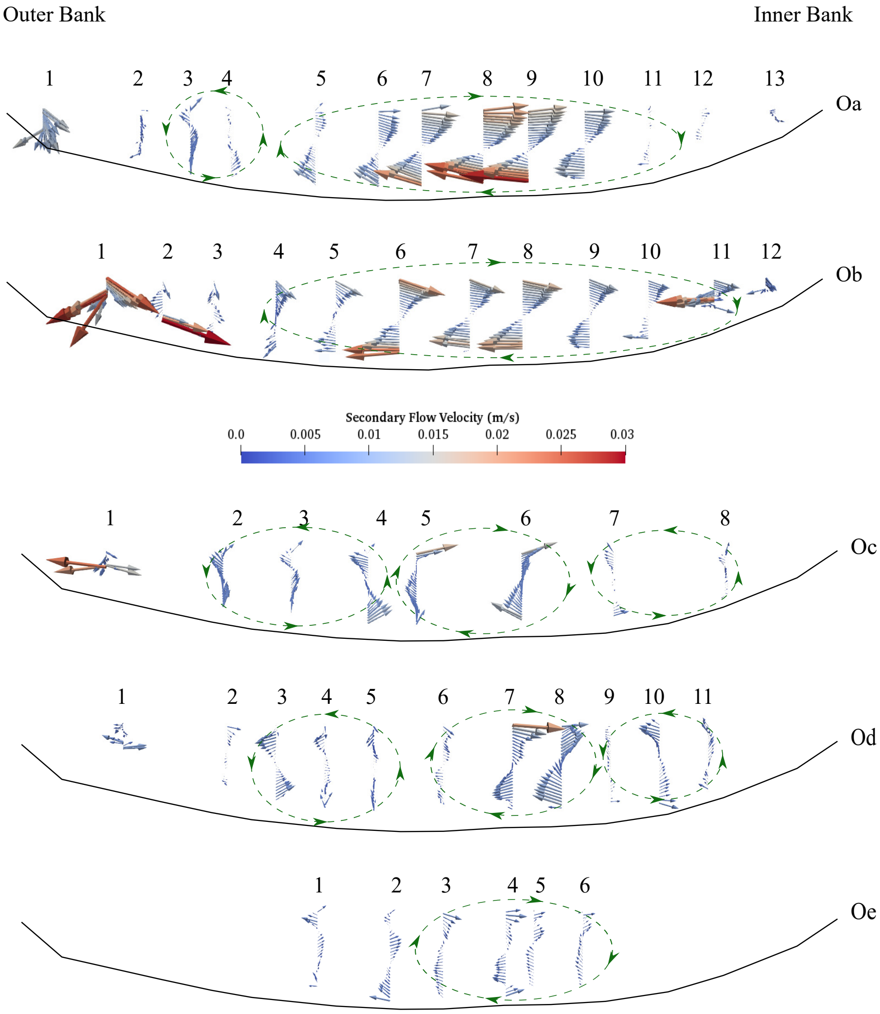

Figure 3.13. The dependence of secondary flow structures at the bridge cross-section on flow discharge (See Table 3.1) under open-surface condition. The secondary flow vectors are visualized with the Rozovskii method. The vertical location of each ADCP measurement on the cross-section is marked with numbers. The number of vectors is reduced by a factor of two for visibility purposes.

Field observations indicates a significant impact of the ice cover on the secondary flow pattern. Since the cross-section Ia, Ib, Ic, and Id are parallel and separated from each other, it is possible to infer the three-dimensional flow structure at the study site as shown in Figure 3.14. Under ice coverage, both the main circulation and the flow convergence pattern are altered. Weak circulations are found in the cross-section Ia (Ia_2 and Ia_4). Here there are signatures of two "double-stacked" cells. However, the senses of rotation are in the opposite directions. The existence of such structures cannot be found in Ib. There are two main structures in Ib, the main circulation and the inner bank cell. Both rotate in the counterclockwise direction between Ib_1-Ib_5 and Ib_6-Ib_7. The secondary flow pattern returns to the regular pattern with a clockwise circulation in the thalweg in Ic and Id. In addition, the inner bank circulation also reverses its direction to the clockwise direction (Ic_6-Ic_7 and Id_6-Id_8). Therefore, the secondary flow pattern varies drastically from one cross-section to another in the ice-covered bend.

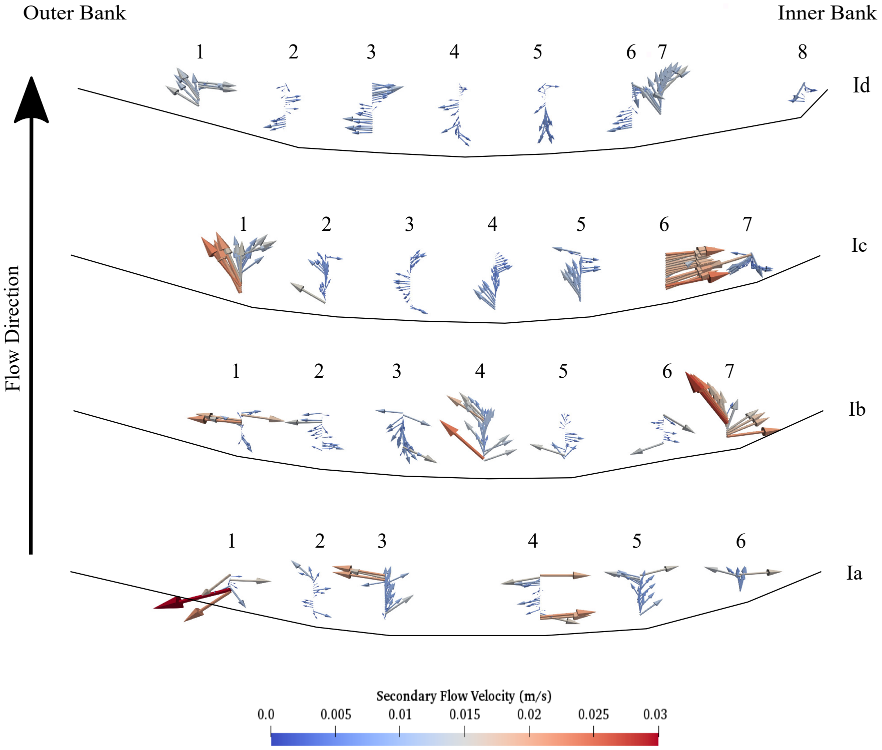

Figure 3.14. The spatial variability of secondary flow structures across four consecutive cross-sections under ice-covered condition in Feb/2021. The cross-sections Ia, Ib, Ic, and Id are parallel to each other and separated by a distance of 6.1 m as shown in Figure 3.13. The flow direction is from Ia to Id in the South-North direction (bottom to top). The ice holes are numbered from the outer bank to the inner bank as shown in Table 3.1. Number of vectors is reduced by a factor of two for visibility purposes.

3.5.6. Shear velocity distribution in the bend

Under open-surface condition, the bed shear velocity ($u_b^\star$) is derived using the logarithmic method as summarized in the Table 3.2. At high discharge (Oa and Ob), $u_b^\star$ can be as high as 0.04 m/s. Despite a slight difference in the value of Q_{Oa} and Q_{Ob}, the distribution of $u_b^\star$ across the cross-section is consistent. In both measurements (Oa and Ob), there exists a strong skewed distribution of the shear velocity toward the outer bank as shown the trend line in Figure 3.15A. The location of the maximum $u_b^\star$ (Oa_2) does not coincide with the maximum depth-averaged velocity location (Oa_4 and Ob_4) (see also Figure 3.3). The value of $u_b^\star$ decreases gradually from the outer bank to the thalweg toward the value of 0.01 m/s, but it slightly increases near the inner bank. This trend is not observed under low discharges (Oc and Od) in Figure 3.15B, which shows that $u_b^\star$ varies in a small range from 0.005 m/s to 0.015 m/s in the thalweg. In brief, a higher discharge leads to a skew $u_b^\star$ distribution with a large magnitude increase (up to four folds) near the outer bank.

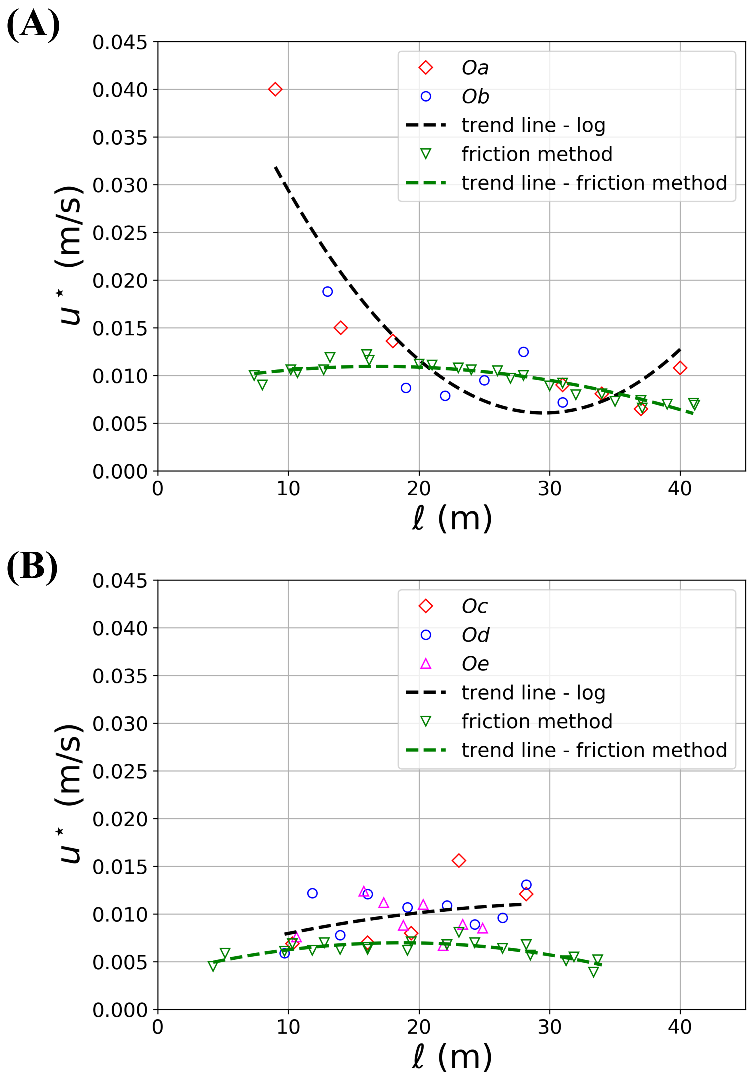

Figure 3.15. Shear velocity ($u_b^\star$) profiles on the river bed under open-surface condition. The value of $u_b^\star$ is derived by the logarithmic fitting method in section 3.4.4. The relative location ℓ to the outer bank (along the East direction) is chosen to represent the vertical locations (see Figure 3.3). Two levels of flow discharge are examined: (**A**) high discharge ($Q_{Oa} = 23.41$ m^3/s and $Q_{Ob} = 23.87$ m^3/s); and (**B**) low discharge ($Q_{Oc} = 14.3$ m^3/s, $Q_{Od} = 12.2$ m^3/s, and $Q_{Oe} = 6.82$ m^3/s). The details of the flow measurements are reported in Table 3.1.

Under ice-covered condition, the value of $u_i^\star$ and $u_b^\star$ are derived from two separate methods: i) the logarithmic law (section 3.4.4); and ii) the quartic profile (section 3.4.5). Shear velocities from the logarithmic law are listed in Table 3.4 for all cross-sections Ia, Ib, Ic, and Id, while estimates from the quartic solution are shown in Table 3.6. On both the ice and the bed layers, the quartic solution can provide the value of $u_i^\star$ and $u_b^\star$ in most ice holes as seen in Figure 3.16. On the contrary, the logarithmic method (solid diamonds) can provide only at particular locations due to the stringent constraints (see section 3.4.4) as seen in Table 3.3. For both $u_i^\star$ and $u_b^\star$, the logarithmic method yields a significantly higher value in comparison to the quartic solution as indicated in Figure 3.16. Both the logarithmic and the quartic methods indicate that $u_i^\star$ and $u_b^\star$ are elevated near banks. In particular, $u_b^\star$ can increase from 0.01m/s (thalweg) to approximately 0.05 m/s near the inner bank. Therefore, shear velocity magnitude varies across the cross-section under ice coverage.

3.6. Discussion

Ice coverage is an essential component of river hydraulics (Ettema, 2002; B. T. Smith & Ettema, 1995; J. Wang et al., 2008). The impacts of ice on flow dynamics in rivers has recently drawn significant attention (Lauzon et al., 2019b) from a wide range of viewpoint such as hydrological (Beltaos & Prowse, 2009), morphological (Chassiot et al., 2020; Kämäri et al., 2015), ecological (Knoll et al., 2019) applications. Under the impact of climate change, global coverage of river ice has declined sharply (Peng et al., n.d.; Yang et al., 2020) potentially leading to a large-scale transformation of river dynamics in cold regions, especially during spring when snow and ice thaw (Lotsari et al., 2020). Changes in river ice dynamics might lead to new morphological evolution of river deltas in cold regions (Lauzon et al., 2019b) as it is known that ice coverage alters sediment transport regime (Lau & Krishnappan, 1985; Turcotte et al., 2011). However, field measurement of ice-covered flows is challenging and thus there are limited data on flow profiles to date (P. M. Biron et al., 2019; Ghareh Aghaji Zare et al., 2016; Lotsari et al., 2017). Therefore, this work is intended to revisit this important problem using a modern approach of turbulent flows.

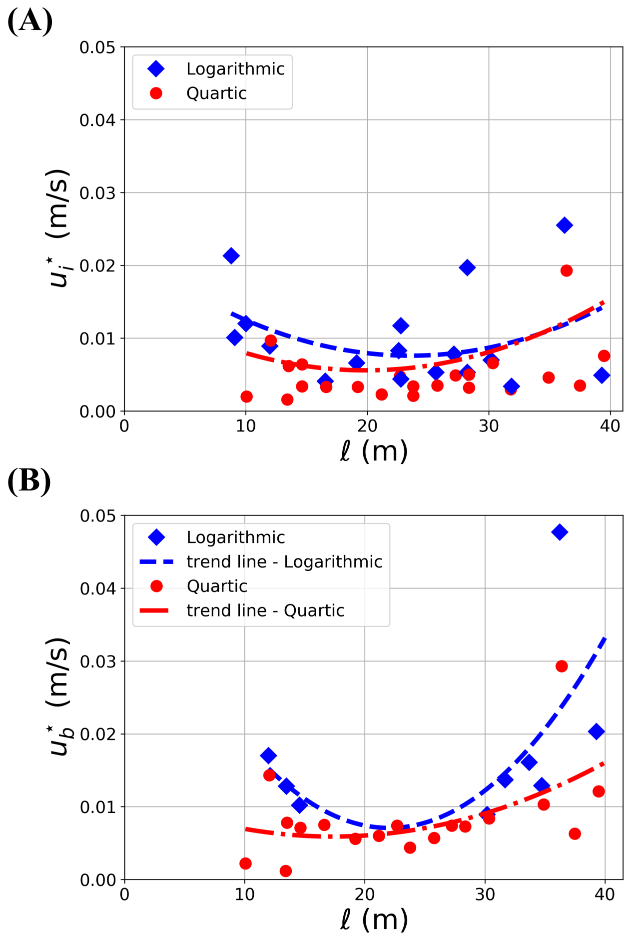

Figure 3.16. The distribution of shear velocity on: (**A**) the ice layer ($u_i^\star$), and (**B**) the river bed ($u_b^\star$) across the bend apex cross-section. The blue diamonds represent the shear velocities which are derived from the logarithmic methodology (section 3.4.4). The red circles represent the shear velocities, which are derived from the quartic methodology. The dash-dotted lines show the trend lines of $u_i^\star$ and $u_b^\star$ with each type of fitting methodology.

3.6.1. The logarithmic layer under open-surface condition

The data support the existence of a universal logarithmic layer (Marusic et al., 2013) for the current site. Results in Table 3.2 show that the logarithmic layer is applicable for vertical locations with sufficient depth ($H \geq 3.5$ m) in the thalweg. In these locations, the logarithmic layer is easily detectable as it accounts for a significant portion of the depth (up to 1.5m as shown in Figure 3.6).

As demonstrated in Figure 3.10, stations Oc_4, Od_7, and Oe_5 all follow closely the logarithmic profile. It has been known that the logarithmic law might be valid for the majority portions of the flow depth (P. M. Biron et al., 1998) in laboratory conditions. The value of δ_b is suggested to be 10 to 20 percent of the total depth (P. M. Biron et al., 1998, 2004) under field conditions. Our results show that the logarithmic layer can extend up to half of the total flow depth ($\delta_b/H = 50\%$) regardless of the flow rate. This observation can be seen in the thalweg region and/or near both banks due to its sensitivity to the local morphological details. As suggested in Afzalimehr and Rennie, 2009, extension of the logarithmic law can be even beyond the value of 50% with a different channel bed condition (gravel).

A closer examination of the logarithmic layer thickness in wall units shows that it follows closely the theoretical bounds in Equation 3.3. Our results in Table 3.2 and Figure 3.10 show that the upper bound is applicable for the current site. In fact, the logarithmic layer can extend well beyond the $0.15Re_\tau$ limit in many cases as shown in Table 3.2. Note that the value of $u_b^\star$ (and thus Re_τ) can be estimated using the Equation 3.16 from the depth-averaged velocity U. Therefore, our data suggests that the Equation 3.3 can serve as an estimation for the logarithmic layer thickness if the velocity profile $u(z)$ is not available.

It is known that complex flow fields in shallow areas or rapidly changing bathymetry (P. M. Biron et al., 1998; Stone & Hotchkiss, 2007) can lead to the deviation from the logarithmic law (P. M. Biron et al., 2004) due to the presence of secondary flows (Petrie & Diplas, 2016). In the presence of complex bathymetry with an adverse pressure gradient, the equilibrium layer could become thin or completely vanish. Thus the logarithmic law might not exist in particular locations (Bagherimiyab & Lemmin, 2013; P. M. Biron et al., 1998).

In meandering rivers, secondary flows (Petrie et al., 2013) might impact the distribution of the vertical velocity profile. The absence of the logarithmic layer is also shown to coincide with a strong presence of secondary flow circulation at our site (Oa_6, Oa_7, Oa_8 - see Figure 3.13A). In particular, the secondary flow is significantly strong in Oa and Ob for locations near both the outer and inner banks. The impact of secondary flow from both banks on the vertical profile is demonstrated in Figure 3.6. While the variation of the vertical profile in the first 1.5 m depth is minimal in Oa_5, there is a significant deviation of the profile from the logarithmic law near the surface of Oc_6 (Figure 3.6B), which is a common signature of secondary flows. This behavior is consistent with field observation of Chauvet et al., 2014, which indicates that the degree of deviation depends on the distance to banks. Thus our results show that it is challenging to perform the logarithmic fitting near both banks even under open-surface condition when the flow depth is limited.

3.6.2. The challenge of using logarithmic fitting for ice-covered flows

It is striking that the theoretical bound for δ_i^+ and δ_b^+ (Equation 3.3) is highly effective. As shown in Table 3.3 and Table 3.4, the limit of δ_{theory}^+ is satisfied in all available cases for both the ice and river bed layers. This highlights a potential use of the Equation 3.3 in examining the presence of the logarithmic layers in ice-covered flows. As the value of $u_b^\star$ can be estimated from the quartic method (section 3.5.4), the value of δ_{theory}^+ can be deduced from the Equation 3.3. Therefore, the physical value of δ_{theory} can be recovered. This estimated value of δ_{theory} can guide field measurements to capture sufficient data.

As the logarithmic fitting is the standard method for estimating $u_b^\star$ in straight channel in open-surface condition (Petrie & Diplas, 2016), it is not clear how to estimate $u_b^\star$ under ice coverage (Attar & Li, 2012; Ghareh Aghaji Zare et al., 2016; A. Sukhodolov et al., 1999), especially in river bends (A. N. Sukhodolov, 2012). Previous works (Ghareh Aghaji Zare et al., 2016; A. Sukhodolov et al., 1999) have assumed the double log-law and used the logarithmic fitting for ice coverage to derive $u_b^\star$. Our results in Table 3.3 and Table 3.4 indicate that only few vertical stations are qualified to perform logarithmic fitting using our data. The strict requirement of the logarithmic fitting thus does not allow the recovery of $u_b^\star$ value for ice-covered condition in all ice holes. The reason for this challenge might be the presence of the secondary flows as shown in Figure 3.14. Under ice-covered condition, the magnitude of the secondary flow is approximately 0.1 m/s, which is in the same order as the streamwise component. Field measurements (Demers et al., 2011; A. Sukhodolov et al., 1999; A. N. Sukhodolov, 2012) have shown that complex three-dimensional flow might arise in river bend with ice-covered condition. This complex flow field (P. M. Biron et al., 1998, 2004) might deviate the near-wall profiles from the classical logarithmic law. Therefore, it is critical to find a robust method to estimate the value of $u_b^\star$ under field condition.

3.6.3. The performance of quartic solution

It has been recognized (P. M. Biron et al., 1998) in early measurements that the logarithmic method requires sufficient data in the boundary layer. This requirement is typically not satisfied in field measurements (Attar & Li, 2012) as it is challenging to obtain measured data near the river bed and the ice layer. Our data in Figure 3.11 shows that the quartic solution agrees well with field measurement. As it uses the velocity profile, the quartic solution can be applied in most ice holes. Note that the quartic solution is designed (Guo et al., 2017) so that it coincides to the logarithmic layer in the limit of $z^+ \to 0$. This feature relaxes the strict requirement of section 3.4.4. Therefore, the quartic solution can provide an estimation for the shear velocity $u_b^\star$ even if there are limited measurements along the vertical profile. One important assumption of the quartic solution is the separation of flows in the ice and the bed layer by a distinct maximum velocity location $u_{max}(z_{max})$.

As shown in Figure 3.1, the velocity profile is governed by different sets of shear velocities (Ghareh Aghaji Zare et al., 2016; Guo et al., 2017; A. Sukhodolov et al., 1999). The presence of u_{max} in the analytical solution is apparent because the shear stress distribution along the depth is assumed to be linear (Guo et al., 2017). However, it is not clear whether or not a distinct u_{max} is evident in field measurements. Our results show that it is challenging to determine the location z_{max} from our field data since the time-averaged profile does not typically show a distinct u_{max}. While our fitting procedure attains good agreement ($R^2 \geq 0.9$) with measurement data, the determination of u_{max} location does affect the overall shape of the profile. The maximum velocity location η_{max} is the critical factor to attain a high value of R^2. In fact, the value of u_{max} and its position in near-bank locations are usually determined decisively as shown in Figure 3.11 (Id_2). However, the minimal variation of the velocity profile $u(z)$ in the mixing core region prevents a straightforward approach to locate η_{max} (Ic_4) in the thalweg. Therefore, an iterative procedure as shown in Section 3.5.4 is necessary to obtain the maximum value for R^2. The difficulty of locating a single value for η_{max} also highlights the limitation of the quartic method. It is required that the velocity profile has a distinct maximum value, which is not guaranteed in the presence of complex bathymetry. The strong secondary flow as illustrated in Figure 3.14 near Ia_5, Ic_4, and Id_7 might deviate the vertical velocity profiles from the quartic form.

3.6.4. Secondary flow patterns

It has been long known that flows in streams and rivers have helical patterns (Demers et al., 2011) which possess secondary flow (SF) components. In contrast to the randomness of turbulent structures, secondary flows appear in time-averaged velocity profiles (Q. Zhong et al., 2016) as separate entities. Secondary flows originate from two main sources: channel curvature (Prandtl's first kind); and heterogeneous turbulent stresses (Prandtl's second kind) (Nikora & Roy, 2012). In the first kind, secondary flow is directed from the inner bank toward the outer bank as the flow approaches a bend (Kang et al., 2011). The impacts of curvature on the formation of the main flow cell are clear and were discussed in many studies (Koken et al., 2013; Van Balen, Blanckaert, & Uijttewaal, 2010). The second kind of secondary flow is formed in response to roughness heterogeneity (Rodríguez & García, 2008). In this flow type, the fluctuations of turbulent shear stress are sustained across the cross-section, leading to the formation of many flow cells (Nezu et al., 1993) occupying the entire cross-section (Blanckaert et al., 2010). The distribution of shear stresses along the cross-sectional perimeter (e.g., bed, bank, and surface) determines the types and number of flow cells, and how these cells interact with each other (Albayrak & Lemmin, 2011; Blanckaert et al., 2010; Nikora et al., 2019; Rodríguez & García, 2008). While this phenomenon has been postulated for natural channels (Nezu et al., 1993), its existence has rarely been investigated under field condition (Chauvet et al., 2014).

Under open-surface condition, our results in Figure 3.13 show a striking dependence of secondary flow patterns on the flow discharge. The dominance of the main circulation in *Oa* and *Ob* is replaced by the co-existence of multiple-cell structures in *Oc*, *Od*, and *Oe*. In effect, our results show a transition from a single circulation (high discharge) to multiple circulations (low discharge). This transition is important because it highlights the potential linkage between the flow discharge with the strength of the main circulation. Our results in *Oa* suggest that the impact of channel curvature, which induces the main circulation, is dominant when the flow discharge is sufficiently large. At low discharges, this dominance is lost. The main circulation and the bank cells all play important roles in creating the helical patterns across the cross-section. This phenomenon agrees with the field observation of Chauvet et al., 2014 and laboratory data of Albayrak and Lemmin, 2011. Future works might be needed in understanding the precise threshold at which this transition occurs.

Comparing our results in Figure 3.13 and Figure 3.14, it is evident that the ice cover adds further complexities in the secondary flow patterns. The maximum velocity is found to be $u_{max} \approx 0.19$ m/s in the thalweg area (see Figure 3.11). Meanwhile, the corresponding secondary flow velocity in the same vertical (Ic_2) remains below 0.015 m/s, which is less than 10% of u_{max}. This range of secondary flow agrees with other observations in literature (Tsai & Ettema, 1994a). While the flow convergence pattern is still visible at Ia, the secondary flow patterns at other cross-sections vary greatly in a short distance of approximately 20 meters. These results indicate that the large-scale flow structure of the entire reach has been modified with the presence of the ice cover. There is no apparent existence of a large-scale circulation at Ia, Ib, and Ic as shown in Figure 3.14. A circulation reemerges at Id near the outer bank but it is also accompanied by a change in the flow convergence pattern. The intermittent appearance of the circulation suggests that the large-scale circulation is truly a local phenomenon, which could depend on the bathymetry and the flow depth.

Laboratory experiment by Urroz and Ettema, 1994a suggests that the secondary flow under ice-covered condition could have a special structure (double-stacked) where two sets of vortices are found on top of each other in the thalweg. Field measurements of Demers et al., 2011 suggest that the double-stacked vortices might exist at the bend entrance. However, our results in Figure 3.14 do not support the persistent existence of such a structure in this case in all cross-sections Ia, Ib, Ic, and Id. Our result only shows a single vortex in Id close to the outer bank. It has been shown (Lotsari et al., 2017) that flow depth can alter the secondary flow pattern of ice-covered flows at river bends by changing the direction of the high-velocity core (Attar & Li, 2013). Therefore, the disagreement from our measurements with the laboratory experiment of Urroz and Ettema, 1994a might be explained by the difference in aspect ratio between field and laboratory scales. In the experimental setup of Urroz and Ettema, 1994a, the range of aspect ratio (AR) is $10 < AR < 20$ (large aspect ratio). In our case, the aspect ratio is estimated to be 10. Thus the double-stacked vortices might appear only at certain aspect ratios of river cross-sections.

3.6.5. Shear stress distribution

In the literature, the period of ice coverage is assumed to be a quiescent period of sediment transport (Ettema, 2002) since the value of $u_b^\star$ is assumed to be smaller than the open-surface counterpart. Comparing the Figure 3.16B and Figure 3.15B under similar flow discharges, it is evident that the ice coverage contributes to a significant increase of $u_b^\star$ near banks. The value of $u_b^\star$ can reach from 0.02 m/s to 0.05 m/s in the vicinity of the inner and outer banks under ice-covered condition. Such a magnitude is comparable to the bed shear stress under open-surface condition near the outer bank as shown in Figure 3.15 at a much higher level of flow discharge (Oa). This finding is surprising since the ice-covered flow discharge is much smaller in comparison to the open-surface ones as shown in Table 3.1. Such a sharp increase indicates a potential impact on sediment transport processes in shallow areas. Future efforts should be carried out to investigate this phenomenon further.

Overall, the friction method (3.4.6) provides an excellent estimation of $u_b^\star$ with minimal input information, especially at low discharge. Under low flow condition (Oc and Od)

in Figure 3.15B, the friction method predicts that $u_b^\star \approx 0.007$ m/s while the logarithmic method suggests that $u_b^\star \approx 0.01$ m/s. However, the it cannot provide an accurate estimation of $u_b^\star$ at high discharge (Oa and Ob) as shown in Figure 3.15A. The friction method gives a reasonable estimation of $u_b^\star \approx 0.01$ m/s throughout the cross-section. However, the friction method cannot capture the extreme values of $u_b^\star$ near the outer bank. A careful approach must be carried out to examine shear velocities near banks separately.

3.6.6. Limitation

In laboratory measurement or numerical simulation (Ma et al., 2021), turbulent statistics can be obtained by extending the averaging time T to an extremely large value ($T = 50\frac{H}{u_b^\star}$, for example). Under field conditions, it is challenging to obtain reliable data for the velocity profile (P. M. Biron et al., 1998) in large rivers. It is because of a well-known limitation of the ADCP signal near the river bed. It requires a long period of measurement (Petrie & Diplas, 2016) to provide an accurate time-averaged velocity profile. Therefore, the duration of measurement (Buffin-Bélanger & Roy, 2005) plays an important role in attaining statistically convergent results. Under open-surface condition, our time series length is set to be a minimum of 600 seconds in all vertical locations. Note that the $T_\infty = 10$ minutes has been reported to be sufficient for ADCP measurement (Chauvet et al., 2014) to reconstruct secondary flow features at field scale.

Since the field campaign can be only carried out when the ice cover is sufficiently thick (≥ 0.25 m) for this Red River, it thus requires that the air temperature in the field campaign should be sufficiently low (a typical situation in February). The ADCP M9 sensor can function properly in the range of air temperature ($> -20^\circ$ C). However, a prolonged campaign in few hours in many ice holes leads to the deterioration of the signal quality as the sensor surface can become frozen easily and make a long acquisition infeasible. In contrast to the open-surface condition, the record length (T_∞) of our ice measurements is short (2 minutes) to prevent the $M9$ sensor surface from freezing. Such a short duration (2 minutes) might not be enough to obtain the fully convergent profile $u_\infty(z)$ ($\pm 5\%$) (Marian et al., 2021). In addition, it is impossible to obtain boundary layer flow in the first distance of 0.25 m from the ice layer due to the configuration of ADCP measurement. Future works need to rely on other modalities such as Acoustic Doppler Velocimetry (ADV) to capture this boundary layer flow more accurately in conjunction with ADCP data. In addition, the comparison between ADV and ADCP data can provide sufficient data for uncertainty analysis (Longo et al., 2012) to precisely determine the required sampling duration T_∞ for ice-covered flows.

In laboratory condition (Flack & Schultz, 2010) or numerical simulation (Ma et al., 2021), the value of the equivalent roughness height, z_0, can be related to the physical roughness (Flack & Schultz, 2010). However, it has been shown (Petrie & Diplas, 2016) that the value of z_0 cannot be determined reliably using field measurement data (Petrie et al., 2013). Under open-surface condition, the obtained values of z_0 can vary from 1.0×10^{-4} m to the order of 10.0 m. This variability agrees with other field studies in literature (Petrie & Diplas, 2016; Petrie et al., 2013). In particular, this range of obtained z_0 does not agree with the measured sediment grain size at the site, which has $d_{50} \approx 0.5$ mm (Galloway & Nustad, 2012). In ice-covered case, our estimation for z_0 varies from 1.0×10^{-7} m to 2.03 m as shown in Table 3.4 for ice roughness. This estimation does not agree with the physical range of ice roughness (Bushuk et al., 2019), which is at the limit of 0.02 m. Therefore, the fitted value of z_0 cannot be interpreted as the actual physical roughness.

3.7. Conclusion

The impacts of ice coverage on velocity profiles in a river bend are investigated using Acoustic Doppler Current Profiler. The main goal is to evaluate the changes in the vertical velocity profiles as well as the secondary flow pattern as the ice coverage emerges in a river bend. In addition, the quartic method is examined as an alternative procedure to derive the bed shear velocity instead of using the classical logarithmic method. Our results show that the vertical flow profiles and the bed shear velocity are altered significantly under ice coverage. The following conclusions are made:

1. Our data support the existence of a universal logarithmic layer close to the river bed (within 20% of the local depth) in the thalweg of the bend under open-surface condition. In particular locations, the logarithmic layer can extend up to 50% of the total depth. In wall units, the theoretical bound (Equation 3.3) is well respected.
2. Under ice-covered condition, the logarithmic law is not recognized for most of the vertical locations. In the cases where it is applicable, the logarithmic layer is restricted in 20% of the total depth.
3. It might be challenging to use the logarithmic law to derive the shear velocities $u_b^\star$ and $u_i^\star$ due to the lack of data both temporally and spatially near the bed and the ice layers. On the other hand, the quartic solution (Guo et al., 2017) is helpful in determining these shear velocities. The quartic solution, however, is sensitive to the determination of z_{max}, which might result in an underestimation of the shear stresses.
4. Our results show that the ice coverage changes the spatial distribution of the bed shear stress across the cross-section. Under the open-surface condition, the spatial distribution of bed shear velocity is skewed toward the outer bank, especially under

a high discharge. Under the ice-covered condition, high values of bed shear velocity appear on both banks. The elevated values of shear stresses near the banks suggest that sediment transport processes might be active during winter in shallow areas.

5. Under open-surface condition, the secondary flow pattern is dependent on the flow discharge. At high discharge, a single circulation dominates the overall pattern. At low discharge, two counter-rotating circulations, which have reverse senses of rotation to the high discharge one, mutually exist. Under ice-covered condition, the secondary flow pattern becomes more complex. Multiple circulations are found simultaneously with alternating senses of rotation. This feature is distinctively different from the open-surface counterparts.

4. MODELING SHEAR STRESS DISTRIBUTION IN ICE-COVERED STREAMS[3]

4.1. Abstract

Distribution of bed shear stress is the critical factor in regulating the meandering of single-thread rivers. However, the impact of ice cover on bed shear stress is largely unknown. I develop a theoretical model of cross-stream momentum balance to examine the distribution of bed shear stresses in ice-covered meandering rivers. To validate the theoretical model, field surveys were carried out in a river reach of the Red River in Fargo, North Dakota. Data monitoring was completed using an Acoustic Doppler Current Profiler to obtain time-averaged velocity profiles. Our theoretical model indicates that an ice covering develops high-shear zones near both the inner and outer banks, which might exacerbate sediment transport and enhance bank erosion. Velocity measurements confirm the results of the proposed model and demonstrate a clear impact of meandering river banks on velocity profiles and secondary flow patterns under ice cover. Based on the results, I hypothesize that ice cover increases turbulent stresses near banks, which in turn lead to the enhancement of the bed shear stress. Our work provides new insights into the impact of ice cover on bed shear stress distribution, which could play an important role in driving sediment-transport processes and the long-term morphodynamic evolution of meandering rivers seasonally covered by ice.

---

[3] The content of this chapter was co-authored by Berkay Koyuncu and Trung Bao Le, and published as a research article in the *Special Publications of Geological Society, London.* Koyuncu was the main analyst and writer. Le assisted with the development of the shear stress distribution model, provided feedback, and served as a proofreader.

4.2. Introduction

Past studies in river hydraulics mostly focused on the ice-free condition (Blanckaert & De Vriend, 2005; Blanckaert & Graf, 2001; Constantinescu et al., 2011; Koken et al., 2013; Van Balen, Blanckaert, & Uijttewaal, 2010). On the other hand, the existence of seasonally observed ice cover during the winter seasons in cold regions changes flow structures (Kirillin et al., 2012; F. Wang, Huai, Guo, & Liu, 2021; F. Wang et al., 2020). In comparison to the open surface condition, the ice cover increases the complexity of the three-dimensional flow structures, especially the vertical velocity profiles (Teal et al., 1994; F. Wang et al., 2020). Hence, the flow dynamics of ice-covered streams is still an active area of research (Demers et al., 2011). To date, the impact of ice cover on the hydrodynamic and morphological characteristics of rivers is still largely unknown (Gautier et al., 2021). Globally, the extent of river ice tends to be decreasing under the impact of climate change (Yang et al., 2020). Thus the understanding of the ice-covered hydrodynamics will assist the prediction of the forthcoming changes in the large-scale morphology of river deltas in cold regions (Lauzon et al., 2019a).

The most common theoretical approach to address the impact of ice is the two-layer hypothesis, which assumes the independent existence of two logarithmic layers near the channel bed and the ice cover, respectively (Urroz & Ettema, 1994a; F. Wang et al., 2020). The presence of the logarithmic layer allows the logarithmic fitting to estimate the shear velocity of the bed ($u_b^\star$) (Petrie & Diplas, 2016). Recently, the logarithmic fitting has been used to estimate the shear velocity of the ice layer ($u_i^\star$) as well (Ghareh Aghaji Zare et al., 2016; A. Sukhodolov et al., 1999). However, the recent work of Guo et al. (2017) suggests that the two-layer hypothesis has many shortcomings including the discontinuity of the velocity gradient (Guo et al., 2017). In addition, the relationship between the shear stresses on the river bed and the ice cover has not been clarified in previous studies due to the de-coupling assumption of the two logarithmic layers.

Bed shear stress is a critical factor in regulating river morphology (Nanson & Huang, 2017). In classical theories of open channel flow in straight channels, the river channel is usually assumed to be infinitely wide (Devauchelle et al., 2022). This assumption ignores the lateral momentum transfer across one cross-section. Thus, the distribution of bed shear stress near banks to the momentum transfer is typically not considered. This assumption is, however, contradictory to the formation process of natural channels (Parker, 1978). The river width has a close relationship with the flow and sediment discharges as the result of the sediment transport process near banks (Métivier et al., 2017; Popović et al., 2021; Seizilles et al., 2013). The bed shear stress distribution plays a critical role in the evolution of river width (Devauchelle et al., 2022; Seizilles et al., 2014).

The most significant location for the cross-stream momentum balance is the river bend. Flow over a bend is characterized by an acceleration of flow velocity near the outer bank, especially at the point of the maximum channel curvature (bend apex). Under open-surface conditions, the centrifugal force gives rise to the emergence of a helical motion that directs fluid from the inner bank toward the outer bank within one cross-section (Ferreira da Silva & Ebrahimi, 2017). This redistribution of momentum has been thought to be the driving force for river meandering. Under the open surface condition, the main circulation in the clockwise direction is dominant throughout the cross-section at a high flow rate (bank-full condition) (Koyuncu & Le, 2022). Under ice-covered conditions, this helical motion (secondary flow) is observed to change (Demers et al., 2011; Koyuncu & Le, 2020). There is evidence suggesting that the helical cell pattern is altered as the ice cover promotes the cross-stream momentum transfer by introducing an additional helical cell near the ice layer (Demers et al., 2011). It is the formation of double-stacked helical cells, which are hypothesized to influence the secondary flow patterns under the ice cover (Lotsari et al., 2017; Tsai & Ettema, 1996; Urroz & Ettema, 1994a). To date, it is unclear how this change affects the distribution of bed shear stress.

In this work, the impact of ice coverage on the bed shear stress distribution is investigated. First, a theoretical model is developed based on the momentum balance to identify the important parameters of the problem. We propose a relationship between the shear stresses on the bed and ice surfaces using the cross-stream momentum balance. Second, field measurements are carried out to provide validation data for the theoretical model. The impacts of the ice cover on the vertical velocity profiles are reported. A comparison between the theoretical model and the measured data is discussed. Finally, the applications of the proposed theoretical model for estimating bed shear stress under ice coverage are explained.

4.3. Methodology

4.3.1. Study area

The study area is chosen as a 1.0-km reach of the Red River, which originates on the border of North Dakota and Minnesota, United States. This specific location was chosen due to the accessibility to the river surface both on open-surface and ice-covered conditions. At the end of the reach, the hydrologic data (water level, discharge, temperature) is collected continuously in the United States Geological Survey (USGS) Fargo station (05054000). The station is located at latitude $46°51'40''$ and longitude $-96°47'00''$ (NAD27) in North Dakota, USA. The gage is at 263 m (862.88 ft) above the datum.

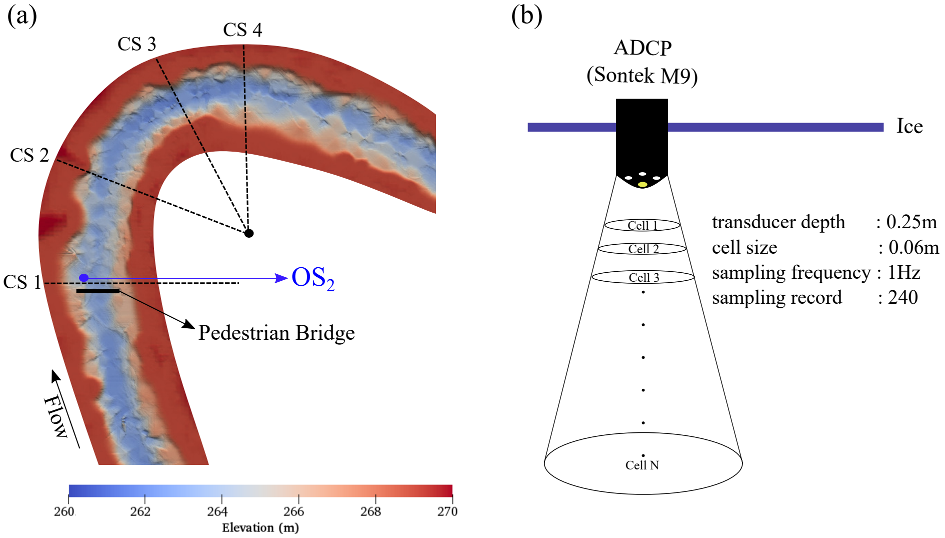

Figure 4.1. (a) The locations of the cross-section CS_1, CS_2, CS_3, and CS_4 in Feb/2022. The location of CS_1 is at the bridge. The elevation of the bathymetry is shown in the UTM-14N WGS-84 coordinate system. A stationary measurement was carried out near the outer bend (OS_2) under open-surface condition (Oct/02/20) as shown in Table 3.1. (b) The placement of the ADCP M9 under the ice cover. Due to the side-lobed configuration of sensors, signal interference might occur near the river bed.

The topography data of the study area is retrieved from the ND Department of Water Resources LiDAR data (https://lidar.dwr.nd.gov/) with the horizontal and vertical accuracy of 1 m and 0.2 m, respectively. The radius of the curvature is measured as 110 m and the river width is approximately 38 m, accordingly, the ratio of the radius of curvature to river width is calculated as 2.9 for the bend in Figure 4.1a.

4.3.2. Field survey

Field surveys are carried out on October/02/2020, October/10/2020, and February/08/2022 in the study area as shown in Figure 4.2c. The summary of the field expeditions is shown in Table 4.1. Sontek M9 Acoustic Doppler Current Profiler (ADCP) is employed for the data collection stage. The sampling frequency of the ADCP was 1Hz with 0.06 m vertical cell size. During all the measurements, the transducer depth is set to 0.25 m

Table 4.1. The summary of all expeditions in Fall 2020 (bridge cross-section and bathymetry measurement), and Winter 2022 (CS_1, CS_2, CS_3, and CS_4). The hydrological data (flow discharge Q and water surface elevation) is monitored at the USGS Fargo (05054000) Station. T (minutes) is the total time of measurement in each vertical/(ice hole).

*(*Case)	*Date*	*Surface*	Q (m^3/s)	Elevation (m)	No. verticals	T (mins)
OS	Oct/02/20	open	23.5	267.22	13	10
Bathymetry	Oct/10/20	open	20.1	267.17	-	-
CS_1	Feb/8/22	ice	11.1	267.05	6	4
CS_2	Feb/8/22	ice	11.1	267.05	6	4
CS_3	Feb/8/22	ice	11.1	267.05	5	4
CS_4	Feb/8/22	ice	11.1	267.05	5	4

below the water surface. Depending on the case and purpose, two deployment techniques are adopted to conduct measurements: (1) moving-vessel (MV), and (2) fixed-vessel (FV) techniques. MV deployment technique is only available for the open surface condition while collecting the bathymetry to develop the digital terrain map (DTM). During the bathymetry collection and cross-sectional measurements, the M9 and the Hydroboard are attached to the kayak and moved on the river surface. On the contrary, FV deployment technique is for the ice-covered condition to monitor the vertical velocity profile by keeping the sensor stationary throughout the recording.

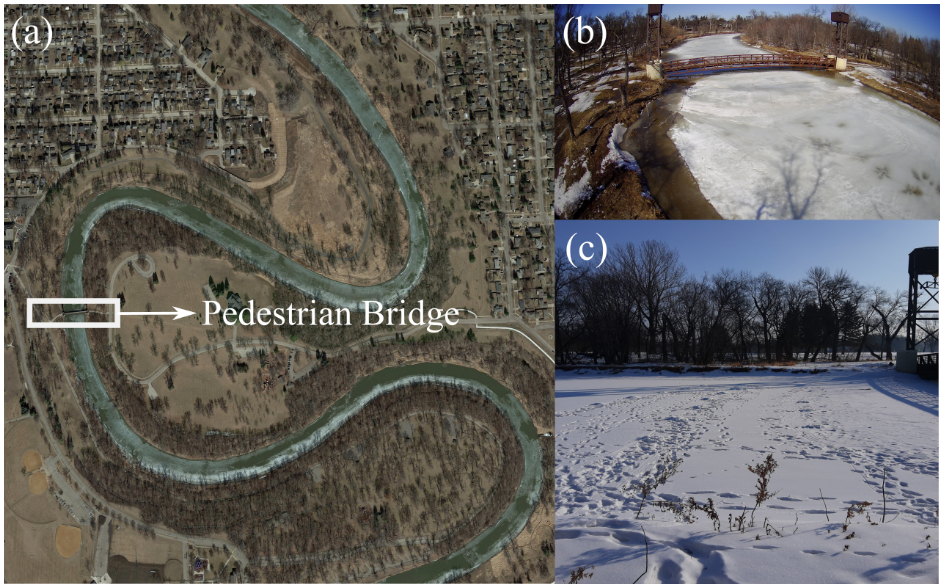

Figure 4.2. (a) The Red River reach in the study area (Source: Google Earth Pro - November/2021). The pedestrian bridge locates in the relative straight portion of the reach; (b) Drone photograph of the pedestrian bridge (3/19/2022); (c) The ice holes were opened along the cross-sections.

Under the open-surface condition (Oct/10/20), the ADCP is towed in the entire bend to create the bathymetry (see Figure 4.1(a)). The depth-averaged velocity is collected continuously along this towing process. In addition, we perform one FV measurement on Oct/02/2020 on the bridge cross-section (see Figure 4.1a and Figure 4.7). These datasets provide the baseline ice-free conditions.

Since the FV deployment technique (stationary technique) is the only available option for the measurements during the winter, ice holes are opened on the cross-sections (see Table 4.1). The most critical issue for the FV technique is that the ice thickness must be thick enough to walk on. The ice thickness is checked manually using a chisel throughout our study in all cross-sections before any measurements. Measurements showed that the ice layer thickness is around $0.3 - 0.5$ m. The air temperature is low at around $-15°C$ on most of our measurement days. In this condition, the ADCP sensor is sensitive to air temperature and its surface could become frozen easily. The ADCP sensor has also the well-known issue of signal interference near the river bed (see Figure 4.1b). Thus, it is challenging to collect data points close to the river bed and the ice cover (Demers et al., 2011).

The field survey in the ice-covered condition was carried out in a single day (8:00 AM - 5:00 PM February 8^{th}, 2022) and thus variations in the flow rate are considered negligible. Four cross-sections are selected at downstream of the pedestrian bridge as CS_1, CS_2, CS_3, and CS_4 as shown in Figure 4.1. The record length for each ice hole is limited to $T = 4$ minutes. We would refer a measurement at the cross-section N with a vertical line M as the notation $CS_N - M$.

4.3.3. Topography and bathymetry data processing

Since the LiDAR data does not provide the river bathymetry, it is necessary to combine the ADCP data and the LiDAR point clouds. After completing the collection of bathymetry and cross-section data, a three-dimensional (3D) model of the study area can be reconstructed. An in-house MATLAB script is written to merge the LiDAR and ADCP data using the reference water level at the USGS Fargo Station. Finally, the Meshmixer software is used to generate the final output, the Digital Terrain Model (DTM), as seen in Figure 4.1.

4.3.4. Flow data processing

The raw data of the ADCP in text format is processed using our in-house MATLAB script to produce a 1 Hz time series of three-velocity components u_E, u_N, and u_{up} in the East, North, and vertical directions of the Universal Transverse Mercator (UTM), respectively. Note that the raw velocity data of ADCP is in the UTM system. Therefore, the local velocity magnitude $u(z,t)$ at one depth(z) and time t is computed as:

$$u(z,t) = \sqrt{u_E(z,t)^2 + u_N(z,t)^2 + u_{up}(z,t)^2} \tag{4.1}$$

A separate MATLAB script is used to calculate flow statistics from the time series including (a) the depth-averaged velocity profiles, and (b) the time-averaged velocity profile for each vertical location. Following the suggestion of Petrie and Diplas, 2016, the time-averaged profiles for each vertical $u(z,T)$ and the depth-averaged value $U(T)$ are computed as the function of averaging period T as :

$$\begin{aligned} u(z,T) &= \frac{1}{T}\int_{t=0}^{t=T} u(z,t)dt \\ U(T) &= \frac{1}{H}\int_{z=-H}^{z=0} u(z,T)dz \end{aligned} \tag{4.2}$$

The final values of $U(T)$ and $u(z,T)$ correspond to the time-averaged values of the entire record. They are denoted as the depth-averaged (U_∞) and time-averaged ($u_\infty(z)$) velocities, respectively, to provide a scale to indicate the range of variability of the signals. Finally, the calculation of the shear velocity $u_b^\star$ and $u_i^\star$ are based on the values of $u_\infty(z)$ as shown in the next sections. If otherwise noted, the notation ∞ is dropped to simplify the discussion of the vertical velocity as $u(z)$.

4.3.5. The logarithmic velocity profile

The traditional method to determine the values of $u_i^\star$ and $u_b^\star$ is to assume that there exist two logarithmic layers near the ice and the bed surfaces in the vertical velocity profile $u(z)$ (Ghareh Aghaji Zare et al., 2016). The logarithmic law of a rough wall for the bed layer is (C. Shen & Lemmin, 1997):

$$\frac{u(z-z_b)}{u_b^\star} = \frac{1}{\kappa}\ln\frac{z-z_b}{k_s} + \beta \tag{4.3}$$

where $\kappa = 0.39$ is the Von Karman constant, and β is the additive constant ($\beta = 8.5$). z_b is the bed elevation. The parameter k_s is the roughness length. In natural rivers, this logarithmic law is typically considered valid within a distance δ_b from the river bed. Typically, δ_b varies from 20% to 50% of the total depth H (Petrie & Diplas, 2016; Petrie et al., 2013).

The shear velocity ($u_b^\star$) and the roughness length (k_s) are found by fitting the Equation 4.3 with the measured data ($u(z-z_b)$) in each vertical. A common procedure is to use the linear regression line between the measured value of $u(z-z_b)$ and $ln(z-z_b)$ (Petrie & Diplas, 2016). As the linear regression line is known, the values of $u_b^\star$ and k_s are computed as:

$$u_b^\star = \kappa m \tag{4.4}$$

$$k_s = exp[8.5\kappa - \frac{\gamma}{m}] \tag{4.5}$$

Here, γ and m are the intercept point and the slope of the best-fit regression line, respectively.

It is common to use wall units to describe the fitting process using $u_b^\star$ and ν to form the velocity and viscous length scales. The vertical distance from the river bed $z - z_b$ and the dimensionless velocity profile $u^+((z-z_b)^+)$ are expressed in terms of wall units as:

$$(H- \mid z \mid)^+ = \frac{(H- \mid z \mid)u_b^\star}{\nu}$$

$$u^+((H- \mid z \mid)^+) = \frac{u(H- \mid z \mid)}{u_b^\star} \tag{4.6}$$

A similar fitting procedure can be carried out to define the shear velocity for the ice layer using the value of $\mid z \mid$:

$$|z|^+ = \frac{|z|u_i^\star}{\nu}$$

$$u^+(|z|^+) = \frac{u(|z|)}{u_i^\star} \tag{4.7}$$

To perform the fitting process, data points must be available in the logarithmic layer. The minimum number of available points is selected as five in the current study. The agreement between the linear regression line and the measured data must also satisfy the following criteria: (1) the correlation coefficient $R^2 > 0.70$, (2) a positive shear velocity $u_b^\star, u_i^\star > 0$, and (3) a realistic value of k_s ($0.001\ m < k_s < 10\ m$). The fitting process is rejected if one of these conditions is not met.

4.3.6. Quartic profile for asymmetrical flows

The quartic profile of Guo et al., 2017 is formulated using the relative distance η, which is defined as $\eta = \frac{2(H-|z|)}{H}$. The maximum velocity location in each vertical (z_{max}) is defined in terms of its relative distance as $\eta_{max} = \frac{2(H-|z_{max}|)}{H}$.

The dimensionless parameter (λ) is used to represent the asymmetry of the flow profile. It is assigned by the fitting as:

$$\lambda = \sqrt{\frac{2}{\eta_{max}} - 1} \tag{4.8}$$

Here $\lambda = \frac{u_i^\star}{u_b^\star}$ quantifies the asymmetry of shear stress on the top ($u_i^\star$) and bottom ($u_b^\star$) surfaces. Therefore, the value of λ is important in determining the shape of the velocity profile.

The location of the zero shear stress plane (η_c) typically does not coincide with the maximum velocity location (Hanjalić & Launder, 1972). In practice, they are relatively close (Guo, 2017). To simplify the fitting procedure, we assume that $\eta_c \approx \eta_{max}$. Thus, this location can relate to λ as $\eta_c \approx \eta_{max} \approx \frac{2}{(1+\lambda^n)}$ with $u_c \approx u_{max}$.

The quartic solution finds the best-fit velocity profile (u_f) to the measured data. u_f can be written in terms of its dimensionless form u^+ with the help of the bed shear velocity $u_b^\star$ as:

$$\frac{u_f(\eta)}{u_b^\star} = u^+(\eta) \tag{4.9}$$

Therefore, the bed shear velocity is used to provide a dimensionless profile $u^+ = u/u_b^\star$. For example, the critical velocity at the critical depth η_c is dimensionless as $u_c^+ = u_c/u_b^\star$.

It is suggested that the dimensionless velocity profile (u^+) follows the analytical solution (Guo et al., 2017):

$$u^+(\eta) = u_c^+ + \phi(\eta) \tag{4.10}$$

Here the velocity profile function ($\phi(\eta)$) is derived for infinitely long and straight channel as:

$$\phi(\eta,\lambda) = \frac{1}{\kappa}\{\ln(\frac{\eta}{\eta_c}) + \lambda \ln\frac{2-\eta}{2-\eta_c} - \frac{1+\lambda}{2}\ln[1+\alpha(1-\frac{\eta}{\eta_c})^2] - (1-\lambda^{n+1})\sqrt{\alpha}\tan^{-1}\sqrt{\alpha}(1-\frac{\eta}{\eta_c})\} \tag{4.11}$$

where, α is an interim parameter ($\alpha = \frac{1-\lambda}{\lambda-\lambda^{2n}}$) used to reflect the asymmetry. In this equation, n is the mixing turbulent intensity. While n can vary depending on the turbulent flow condition, it is found for the symmetric flow condition as $n = 5/6$ (Guo et al., 2017). The shear velocity at the river bed can be calculated using all available data points as:

$$u_b^\star = \frac{\sum_i \phi(\eta_i,\lambda)(u_i - u_c)}{\sum_i \phi^2(\eta_i,\lambda)} \tag{4.12}$$

The shear stresses can be computed as:

$$\begin{aligned} \tau_b &= \rho(u_b^\star)^2 \\ u_i^\star &= u_b^\star\lambda \\ \tau_i &= \rho(u_i^\star)^2 \end{aligned} \tag{4.13}$$

4.3.7. Secondary flow visualization

The classical Rozovskii method is used to visualize the secondary flow pattern (Lane et al., 2000). The Cartesian components of the velocity u_x (East), u_y (North), and u_z (up) are used to derive the secondary components. The primary and the secondary flow components are u_p and u_s are computed using the projections of the East and North components on the depth-averaged velocity vector at the vertical:

$$u_p = (u_x^2 + u_y^2)^{0.5} \cos(\theta - \omega) \tag{4.14}$$

$$u_s = (u_x^2 + u_y^2)^{0.5} \sin(\theta - \omega) \tag{4.15}$$

Here ω and θ are defined as the angle between the depth-averaged vector U and the time-averaged vector u to the x (East) direction in the counter-clockwise direction. The components u_s and the u_z are used to visualize the secondary flow pattern.

4.3.8. The theoretical model

To simplify the analysis, we introduce conceptually a local coordinate system (x, y, z), which changes from one cross-section to another. The x, y, and z are the cross-stream, streamwise, and vertical directions, respectively. The cross-stream direction (x) is identified as the water/ice interface identically as shown in the model configuration in Figure 4.3. Here the coordinate system is local to each cross-section with $x = 0$ at the intersection between the water surface and the outer bank. In the mathematical expressions, we assume a flat water/ice interface across the cross-sections. The ice-water interface is also used to determine the $z = 0$ plane.

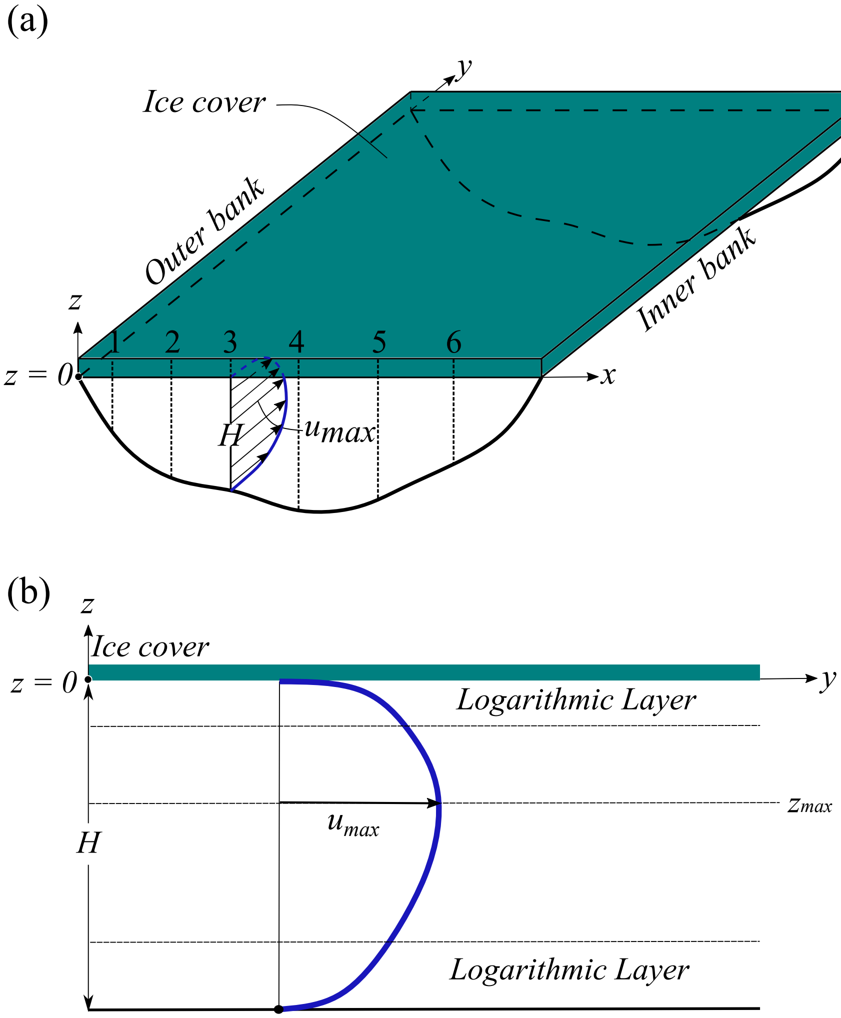

Figure 4.3. (a) The mathematical model of the cross-stream momentum transfer utilizes the local coordinate system. (b) The vertical flow profile and the logarithmic layers under the ice cover. The ice-water interface is set at the level $z = 0$. The main flow direction (streamwise) aligns toward the y axis. The cross-stream direction x starts from the outer bank $x = 0$ toward the inner bank $x = B$. The local depth at one location on the cross-section defines the cross-sectional shape $H(x)$. The maximum velocity u_{max} appears near the mid-depth of the vertical under the ice cover. The verticals are numbered as 1, 2, 3 etc. from the outer bank toward the inner bank across the cross-section. The number of verticals for each cross-section is shown in the Table 4.1.

Three components of the velocity field $\vec{u}(u_1, u_2, u_3)$ are denoted as u_1, u_2, and u_3 in the x, y, and z, respectively. Note that the streamwise velocity component is u_2 whereas the (u_1, u_3) are the cross-stream velocity components. Under this configuration, the distribution of the streamwise velocity profile $u_2(x, z)$ can be described by the balance of momentum (Devauchelle et al., 2022). The details of the mathematical analysis can be found in the Appendix.

With the use of turbulent viscosity ν_t, the gravitational acceleration g, the energy slope S_f, and ignoring the effect of curvature, the momentum equation is:

$$\nu_t \left(\frac{\partial^2 u_2}{\partial^2 x} + \frac{\partial^2 u_2}{\partial^2 z} \right) + g S_f = 0 \tag{4.16}$$

The no-slip conditions on the ice-water interface and the river bed can be written as:

$$\begin{aligned} u_2 = 0 \ \ for \ \ z = 0 \ \ (ice - water \ \ interface) \\ u_2 = 0 \ \ for \ \ z = -H(x) \ \ (river \ bed) \end{aligned} \tag{4.17}$$

Note that the flow depth $H(x)$ changes from one vertical to the other (the cross-section shape) as shown in Figure 4.3. We assume that the river cross-section can be approximated by a polynomial function that is sufficiently smooth so that the side slope exists ($\mid \frac{\partial H}{\partial x} \mid < \infty$) (Abramian et al., 2020).

The depth-averaged streamwise velocity (U_2) can be computed as:

$$\int_{z=-H}^{z=0} u_2 dz = U_2 H \tag{4.18}$$

Here we use the definition of the shear stresses on the ice (τ_i) and the bed (τ_b) surfaces:

$$\tau_i = -\mu_t \frac{\partial u_2}{\partial z}\Big|_{z=0}$$

$$\tau_b = \mu_t \frac{\partial u_2}{\partial z}\Big|_{z=-H} \tag{4.19}$$

After several algebraic transformations as shown in the Appendix, the Equation 4.16 can be written as:

$$\rho\nu_t \frac{\partial^2}{\partial x^2}(U_2 H) - \tau_i - \tau_b \left(1 + \left(\frac{\partial H}{\partial x}\right)^2\right) + \rho g S_f H = 0 \tag{4.20}$$

The impact of the lateral momentum transfer is accounted by the variation of the depth ($\frac{\partial H}{\partial x}$) and the lateral transfer of turbulence ($\rho\nu_t \frac{\partial^2}{\partial x^2}(UH)$) along the cross-section.

The ratio between the shear stresses can be related to the shear velocity ratio via a factor λ as follows:

$$\lambda = \frac{u_i^\star}{u_b^\star}$$

$$\frac{\tau_i}{\tau_b} = \frac{\rho(u_i^\star)^2}{\rho(u_b^\star)^2} \tag{4.21}$$

The bed shear stress can be estimated as:

$$\tau_b = \frac{\rho g S_f H + \rho\nu_t \frac{\partial^2}{\partial x^2}(U_2 H)}{1 + \lambda^2(\frac{\partial H}{\partial x})^2} \tag{4.22}$$

The value of depth-averaged ν_t can be approximated as $\nu_t = 0.1u_b^\star H$ (Vionnet et al., 2004). Once the bed shear stress (τ_b) is available from measurements, it is possible to validate our theoretical model by comparing the measured value of τ_b with one obtained from Equation 4.22. Accordingly, the shear velocity can be estimated with the relationship of $u_b^\star = \sqrt{\frac{\tau_b}{\rho}}$.

To validate the mathematical results with the measurement data, we introduce a notation ℓ to represent the measured distance from one point to the outer bank in the field measurements. Conceptually, ℓ and x are identical. However, it is challenging to determine the exact starting point of the cross-section under the ice cover. Thus, a reference point on the outer bank is selected for $\ell = 0$. This selection does not affect all calculations since only the value of derivatives is needed in our model.

4.4. Results

4.4.1. Flow pattern induced by the ice coverage

The statistical properties of the velocity time series $u(z,t)$ are examined to determine the accuracy of the time-averaged $u_\infty(z)$ and the depth-averaged U_∞ velocities. As illustrated in Figure 4.4, the values of the time-averaged velocity ($u(z,T)$) and depth-averaged velocity ($U(T)$) converge to the long-term values (u_∞ and U_∞) as the measurement duration T is increased. For example, the value of $U(T)$ varies largely in the first 35 seconds of $CS_3 - 3$. However, $U(T)$ remains within the 5% of U_∞ as $T > 35$ seconds. The convergence of the $u(z,T)$ to u_∞ at different depths exhibits a similar fashion. However, the impact of the ice surface and the river bed boundaries is evident. Measurement results show that the velocities at different depths in both stations including the one close to the surface (dashed blue line) and bed (dashed yellow line) are within the 10% of the long-term values ($u_\infty(z)$)

after the 40^{th} second. Of note, the velocity in the vicinity of the ice surface ($z_1 = -0.44\ m$) at $CS_2 - 4$ fluctuates until the 180^{th} second. This type of fluctuation poses a challenge in obtaining accurate data near the ice cover.

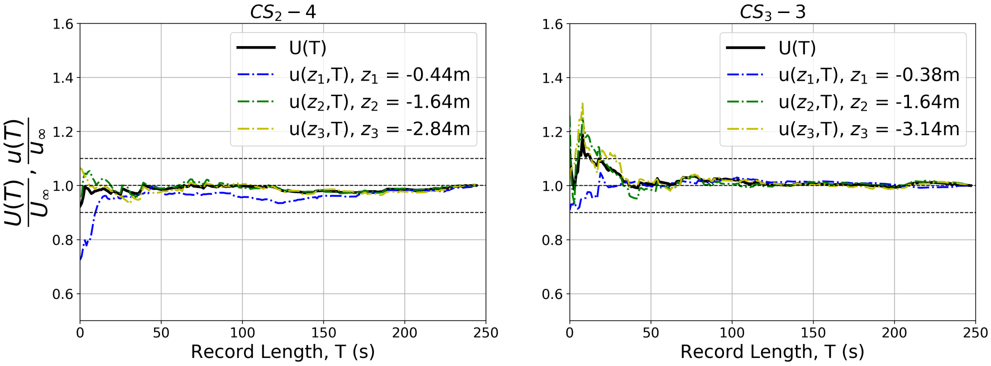

Figure 4.4. The convergence properties (Equation 4.2) of the time-averaged ($u(z,T)$) and depth-averaged ($U(T)$) velocities of $CS_2 - 4$, and $CS_3 - 3$ at different depths (z) as a function of the measurement duration T. The instantaneous velocity magnitude $u(z,t)$ is computed from the East, North, and up components of the measured ADCP data $u(z,t) = \sqrt{u_E^2(z,t) + u_N^2(z,t) + u_{up}^2(z,t)}$. In both cases (the 4^{th} station of CS_2 and the 3^{rd} station of CS_3), the measured verticals are in the thalweg. The value of $u(z,T)$ converges quickly within $T = 100$ seconds.

As the value of U_∞ is available for ice holes, it is possible to reconstruct the planform of the flow pattern. The depth-averaged velocity vectors ($U_\infty(u_E, u_N)$) on February/08/2022 are represented in Figure 4.5 and Figure 4.6(a). Here, the impact of the channel curvature can be seen clearly at the cross-section CS_1, which is located next to the pedestrian bridge (see Figure 4.1). The U vectors direct toward the inner (west) bank indicating a sharp turn in the large-scale flow pattern (see Figure 4.5 and Figure 4.6(a)). On the other hand, the flow vectors in the CS2 show a spreading pattern, which is caused by the complex helical pattern at the bend apex. The flow adapts to the channel curvature well at CS_3 and CS_4. In comparison to the open-surface condition as seen in Figure 4.6(b), the flow patterns at the corresponding cross-sections do not change significantly. While the flow velocity is higher under the open-surface condition, the direction of the velocity vectors indicates a consistent flow planform. In brief, the presence of the ice cover did not substantially alter the flow planform in the bend.

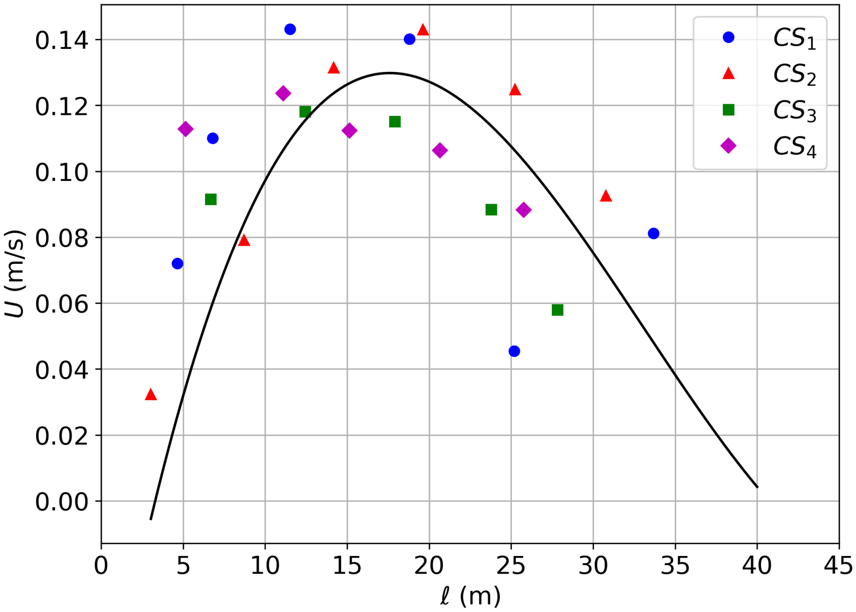

Figure 4.5. The depth-averaged velocity profile $U(x)$ in the river reach of Feb/2022 measurement. The symbols represent the actual measurements at CS_1, CS_2, CS_3, and CS_4. The line denotes the assembled profile from the measured data as the guide for the eye. The assembled profile shows a slight asymmetry toward the outer bank. The distance to the outer bank ℓ is used as the cross-stream direction x (see also the diagram in Figure 4.3).

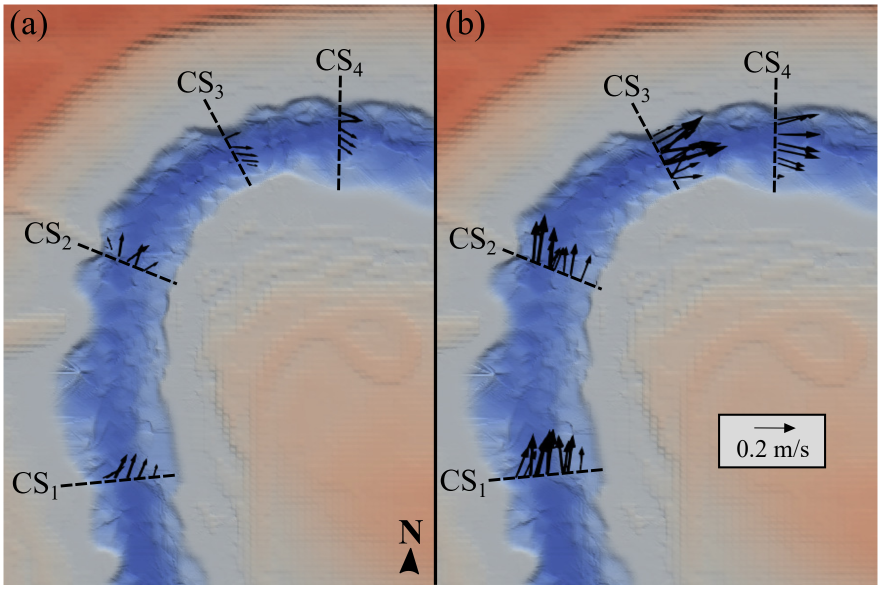

Figure 4.6. Depth-averaged velocity (U) direction (a) under ice-covered condition (February/08/2022), and (b) under open surface condition (October/10/2020). The value of U is computed using the Equation 4.2 from the measured time series. There exists a significant impact of the local bathymetry on the depth-averaged velocity distribution in addition to the channel curvature effect.

The presence of the ice cover, however, alters the vertical flow profile completely. Figure 4.7 shows the measured vertical velocity profiles close to the outer bank ($l < 10$ m) under open surface and ice-covered conditions. As shown in Figure 4.7a, the presence of a logarithmic layer can be found up to 1 m from the river bed under the open-surface condition (OS_2). As displayed at vertical $CS_2 - 2$ (Figure 4.7b), ice cover changes the velocity profile into a nearly symmetrical shape due to its additional resistance at the top. Moreover, the flow velocity under the ice cover is remarkably slower in comparison to the case under the open surface condition (OS_2 - Figure 4.7a). On contrary to the open-surface condition, the logarithmic layer is not guaranteed to be found under the ice-covered condition. According to our logarithmic fitting methodology, the presence of the logarithmic layer is confirmed near the river bed for $CS_2 - 2$ as shown in Figure 4.7(b) ($R^2_{bed} = 0.96 > 0.7$). However, the logarithmic layer is not confirmed for the ice layer ($R^2_{ice} = 0.68 < 0.7$). The two-layer hypothesis is not considered valid for this case.

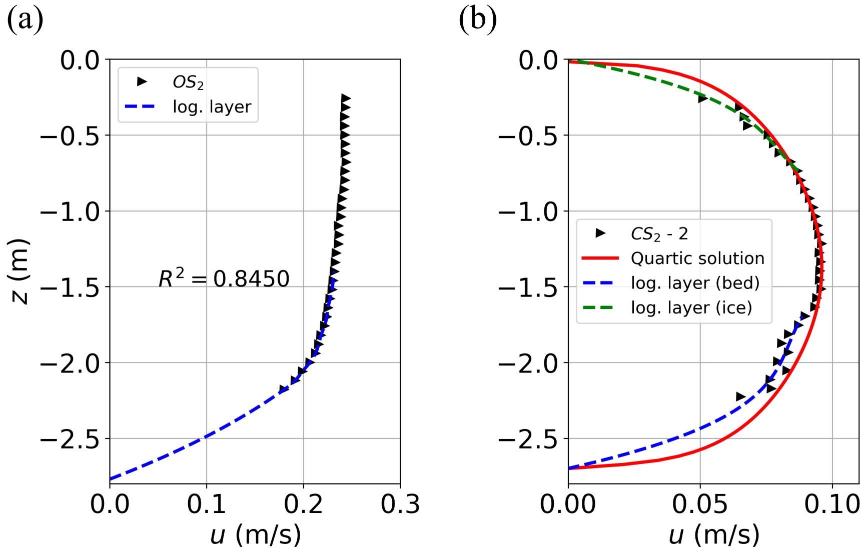

Figure 4.7. The measured vertical velocity profiles near the outer bank at (a) the station OS_2 ($\ell = 9.85m$) on October/02/2020 (open surface condition), and (b) station $CS_2 - 2$ ($\ell = 8.75m$) on February/08/2022 (ice-covered condition). Two separate values of R^2 were obtained during the fitting for the logarithmic layers: (i) near the ice (green dashed line) $R^2_{ice} = 0.68$; and (ii) near the bed (blue dashed line) $R^2_{bed} = 0.96$. The quartic solution (solid red line) is shown ($R^2 = 0.85$) to demonstrate its difference from the logarithmic profiles.

To evaluate the changes of the vertical profiles along the river reach, the vertical profiles along the thalweg are plotted as seen in Figure 4.9. The presence of the ice cover shifts the position of the maximum time-averaged velocity (u_{max}) toward the river bed. As shown in Figure 4.9, the location of u_{max} is not close to the ice layer. In most cases, u_{max} locates near one-half of the depth. The flow profiles do vary from CS_1 to CS_4 along the thalweg. The value of $u_{max} \approx 0.15\ m/s$ and approximately 0.12 m/s at $CS_1 - 3/CS_2 - 4$ and $CS_3 - 2/CS_4 - 1$, respectively. The position of the u_{max} at $CS_1 - 3$ is around the mid-depth ($z = -1.5\ m$); however, it is closer to the ice cover at the other three stations. Therefore, the channel curvature does have an effect in altering the maximum core velocity of the vertical velocity profile.

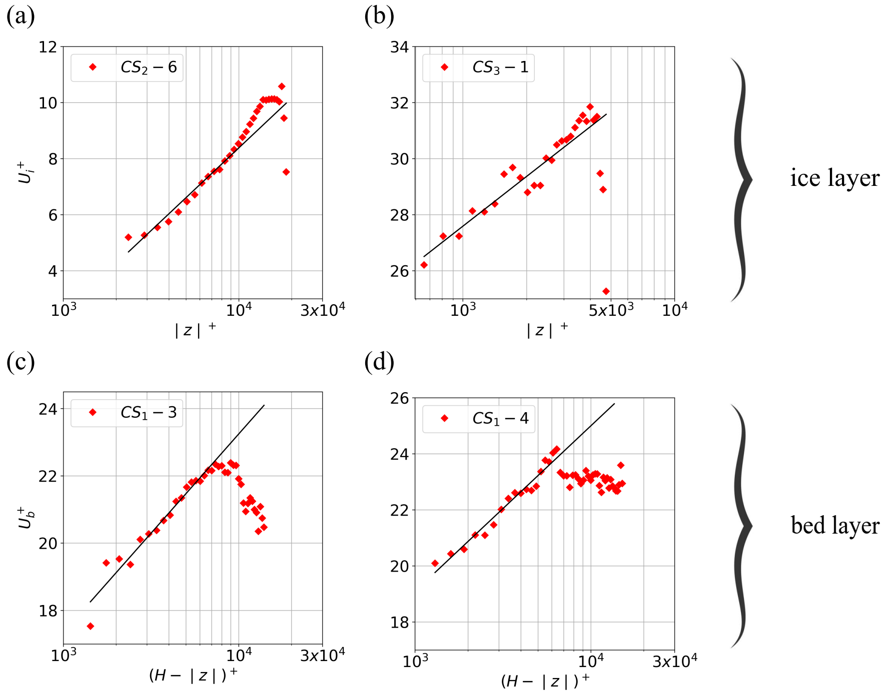

Figure 4.8. The logarithmic fitting for the flow profiles near the ice (top row - a, b) and river bed (bottom row - c, d) surfaces. The absolute value of z ($|z|$) denotes the distance to the ice/water interface as shown in Figure 4.3. H is the total depth at the vertical. The cross-sections CS_1, CS_2, CS_3, and CS_4 are shown in Figure 4.1. The solid line denotes the logarithmic law of the Equation 4.3. The detailed parameters for the fitting in each ice hole are shown in the Table 4.2.

4.4.2. The logarithmic velocity profile

Logarithmic fitting is employed to determine the shear velocities for the 2022 dataset as summarized in Table 4.2. The logarithmic layer is found only in deeper verticals. In general, the logarithmic layer is evident if the flow depth is greater than $2m$. Two vertical profiles ($CS_2 - 6$ and $CS_3 - 1$) from winter 2022 measurements are presented in Figure 4.8a and Figure 4.8b to demonstrate the extension of the logarithmic law in the ice layer. In the bed layer, the fitting is successful for 14 out of 28 and 14 out of 22 verticals in 2021 and 2022, respectively. It is important to note that the logarithmic layer can extend far (approximately one meter) from the ice and bed surface as shown in Figure 4.7. The details of the fitting are as follows.

Table 4.2. Derivation of the shear velocity $u_i^\star$ and $u_b^\star$ using the logarithmic fitting for the case CS_1, CS_2, CS_3, and CS_4 (see Table 3.1). The notation $-$ denotes an unsuccessful fitting in that vertical. H and ℓ are the flow depth and the distance to the outer bank, respectively. The value of R^2 denotes the degree of fit.

Case	H (m)	ℓ (m)	R^2 (bed)	$u_b^\star$	R^2 (ice)	$u_i^\star$
$CS_1 - 1$	1.10	4.66	-	-	-	-
$CS_1 - 2$	2.35	6.83	0.7523	0.0075	-	-
$CS_1 - 3$	3.21	11.58	0.9575	0.0066	-	-
$CS_1 - 4$	3.55	18.90	0.9660	0.0062	-	-
$CS_1 - 5$	3.23	25.30	0.8778	0.0060	0.7938	0.0021
$CS_1 - 6$	1.05	33.83	-	-	-	-
$CS_2 - 1$	0.80	3.05	-	-	-	-
$CS_2 - 2$	2.70	8.75	0.9683	0.0121	-	-
$CS_2 - 3$	3.80	14.23	0.9202	0.0129	-	-
$CS_2 - 4$	3.93	19.72	0.9000	0.0060	0.7831	0.0028
$CS_2 - 5$	3.38	25.36	0.9526	0.0112	-	-
$CS_2 - 6$	2.40	30.91	-	-	0.9713	0.0112
$CS_3 - 1$	2.40	6.70	0.9420	0.0135	0.8865	0.0031
$CS_3 - 2$	4.50	12.50	0.7443	0.0035	-	-
$CS_3 - 3$	4.41	17.98	-	-	-	-
$CS_3 - 4$	3.95	23.59	-	-	-	-
$CS_3 - 5$	3.23	27.71	0.9310	0.0107	-	-
$CS_4 - 1$	2.21	5.18	0.8841	0.0163	0.9622	0.0034
$CS_4 - 2$	3.64	11.16	0.8477	0.0060	-	-
$CS_4 - 3$	4.24	15.21	-	-	-	-
$CS_4 - 4$	3.90	20.76	0.7495	0.0063	-	-
$CS_4 - 5$	3.34	25.88	-	-	-	-

The extension of the logarithmic layer in the bed layer is illustrated in Figure 4.8c ($CS_1 - 3$) and Figure 4.8d ($CS_1 - 4$). Here, $(H- \mid z \mid)^+$ is the dimensionless length representing the vertical distance from the channel bed. The separation from logarithmic layer starts at $(H- \mid z \mid)^{+} \approx 7000$ for the case $CS_1 - 3$, and $(H- \mid z \mid)^{+} \approx 6500$ for the case $CS_1 - 4$. Thus, the extension of the logarithmic layer varies from one vertical to another.

The cross-stream distribution of $u_b^{\star}$ in CS_1, CS_2, CS_3, and CS_4 shows an increase of $u_b^{\star}$ near banks as seen in Table 4.2 (see also Figure 4.12). The maximum $u_b^{\star}$ value around the channel center is found to be 0.0129 m/s ($CS_2 - 3$). A higher value of $u_b^{\star} \approx 0.0163$ m/s is found near the outer bank ($CS_4 - 1$). The value of $u_b^{\star}$ is approximately 0.0112 m/s near the inner bank ($CS_2 - 5$). In brief, the bed shear stress is found to be higher near both banks in comparison to the channel center.

4.4.3. The quartic profiles

The application of the quartic profile on ice-covered data sets suggests that it is applicable to most of the observed vertical profiles. Figure 4.9 illustrates the velocity distribution function (Equation 4.11) of $CS_1 - 3$, $CS_2 - 4$, $CS_3 - 2$, and $CS_4 - 1$. The quartic solution is highly robust when the flow depth is sufficient ($H > 2$ m) as shown in Table 4.3. The R^2 value is mostly higher than 0.9 as shown in Table 4.3. Here, the position of the u_{max} does not usually correspond to the symmetry plane ($\eta_{max} \neq 1$). Our results confirm that the value of λ is generally less than 1 as shown in Table 4.3 in most verticals. These results imply that the location of u_{max} in most of the stations is closer to the ice surface (see Equation 4.8). Exceptions are found in the vertical $CS_1 - 2$ and $CS_4 - 5$ (near banks) in which u_{max} is closer to the channel bed. In brief, the quartic is robust in replicating the vertical profiles under ice cover.

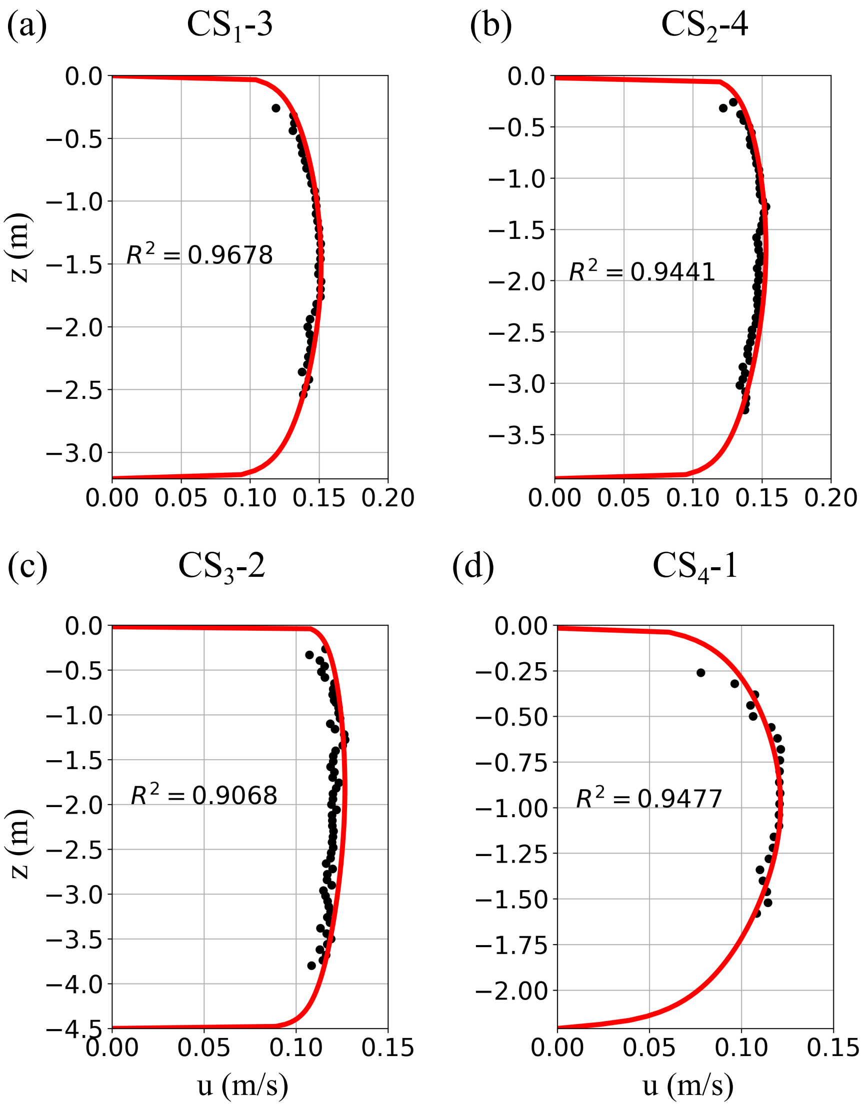

Figure 4.9. The performance of the quartic solution in replicating the measured profiles along the vertical direction z. The measured vertical profiles (points) in ice holes of cross-section CS_1-3, CS_2-4, CS_3-2, and CS_4-1 (see Figure 4.6). The profiles are selected along the thalweg CS_1-3, CS_2-4, CS_3-2, and CS_4-1. The quartic profile (thick red line) is found by fitting the Equation 4.11 with the measured data. The parameters for the fitting of each ice hole are shown in the Table 4.3.

The ability of the quartic profile to determine values of $u_b^\star$ using the velocity distribution function ($\phi(\eta, \lambda)$) in Equation 4.12 is shown in Table 4.3. Comparing Table 4.2 and Table 4.3, it is evident that the quartic velocity distribution provides significantly lower values for $u_b^\star$. For example, the logarithmic method predicted $u_b^\star = 0.0060\ m/s$ (Table 4.2) at $CS_1 - 5$. On the contrary, the quartic method gave $u_b^\star = 0.0037\ m/s$ (Table 4.3) at the same vertical. In conclusion, the quartic method provides a lower value for $u_b^\star$.

Table 4.3. Derivation of the shear velocity on the bed layer ($u_b^\star$) and on the ice layer ($u_i^\star$) using the quartic solution for CS_1, CS_2, CS_3, and CS_4. The position of η_{max} and the value of u_{max} is determined by optimizing the R^2 of the velocity distribution function. The details of the mathematical notations are explained in Equation 4.8 to Equation 4.12.

Case	H (m)	u_{max}	R^2	$u_b^\star$	$u_i^\star$	λ	η_{max}
$CS_1 - 2$	2.35	0.1242	0.7663	0.0031	0.0047	1.5226	0.6027
$CS_1 - 3$	3.21	0.1514	0.9678	0.0049	0.0050	1.0232	0.9771
$CS_1 - 4$	3.55	0.1488	0.9409	0.0031	0.0023	0.7434	1.2881
$CS_1 - 5$	3.23	0.1266	0.9563	0.0037	0.0031	0.8479	1.1635
$CS_2 - 2$	2.70	0.0960	0.8470	0.0075	0.0067	0.9035	1.1011
$CS_2 - 3$	3.80	0.1402	0.9061	0.0067	0.0049	0.7391	1.2935
$CS_2 - 4$	3.93	0.1528	0.9441	0.0051	0.0036	0.6991	1.3434
$CS_3 - 1$	2.40	0.0991	0.9150	0.0044	0.0024	0.5482	1.5379
$CS_3 - 2$	4.50	0.1265	0.9068	0.0031	0.0019	0.6256	1.4374
$CS_4 - 1$	2.21	0.1211	0.9477	0.0087	0.0058	0.6714	1.3786
$CS_4 - 4$	3.90	0.1098	0.9372	0.0017	0.0008	0.4586	1.6525
$CS_4 - 5$	3.34	0.0956	0.9099	0.0008	0.0016	1.9778	0.4072

4.4.4. Secondary flow patterns

The secondary flow pattern along the river reach is illustrated in Figure 4.10 using the classical rotation-based Rozovskii method. The overall pattern is convoluted indicating the significant impact of the local bathymetry. At the first cross-section CS_1, there exists a strong return flow from the outer bank toward the thalweg at vertical 1. This return flow persists till the secondary cross-section CS_2. Additionally, two circulations are found near verticals 3 and 5, which are closer to banks. These single circulations are also present in other cross-sections CS_2, CS_3, CS_4. Strikingly, the double helical cells are observed in the second, CS_3 and third cross-sections (CS_2 and CS_3). At the vertical $CS_2 - 4$ and $CS_3 - 4$, counter-clockwise circulations are found both near the ice cover and the channel bed.

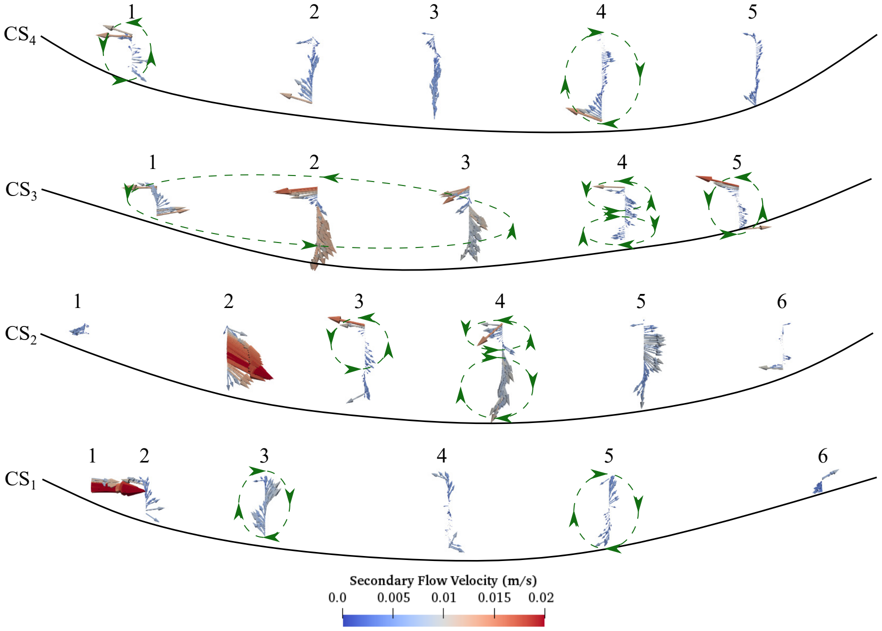

Figure 4.10. The secondary flow pattern is visualized by the classical Rozovskii's method (Lane et al., 2000). The secondary flow velocity pattern changes from one cross-section to another as the helical cells emerge. The double-stacked cells are found at the cross-sections CS_2 and CS_3. Flow direction follows the North direction (from bottom to top).

4.4.5. Modeling the lateral momentum transfer

The Equation 4.22 provides a reasonable estimation of lateral momentum transfer but it requires the evaluation of cross-stream derivatives. As shown in Table 4.1, the flow depth and velocities are obtained only in several verticals. Therefore, there is insufficient data to generate estimations of these derivatives. Thus, a polynomial least square method using a quadratic function ($f(x) = c_0 + c_1\, x + c_2\, x^2$) is used to develop the fitting curve for the available datasets of $H(x)$ and $U_2H(x)$. As an example, the cross-section profile of CS_2 is represented in Figure 4.11a. Our fitting results show excellent agreements between the measured data and the quadratic curves with $R^2 > 0.75$. The shape of the cross-section can be described reasonably well with the fitted curve. However, the precise location of the thalweg is slightly shifted towards the inner bank. The unit flow rate $(U_2H(x))$ is also well captured by the fitting process as depicted in Figure 4.11b. The values of $(\frac{\partial H(x)}{\partial x})$ and $\frac{\partial^2(U_2 H(x))}{\partial x^2}$ are derived from the coefficients c_0, c_1 and c_2 of the fitted curve.

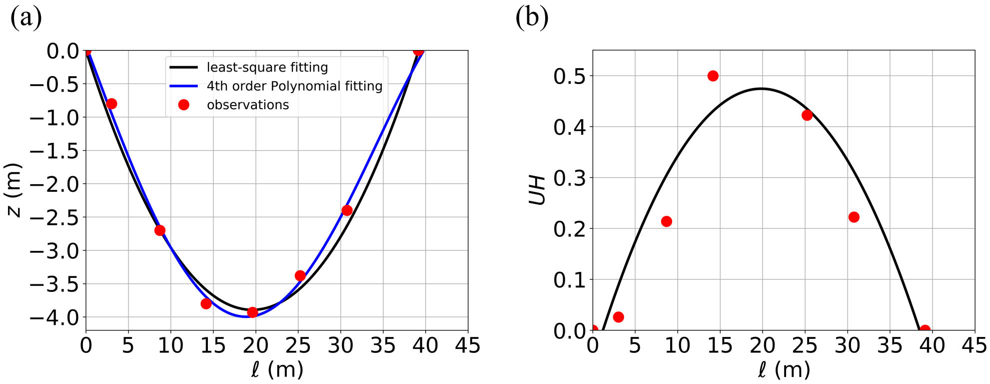

Figure 4.11. Procedures to compute the cross-stream derivatives. The least-square fitting is performed for: (a) the water depth ($H(x)$ - the cross-sectional shape); and (b) the unit flow rate $q(x) = U(x)H(x)$. The depth and the unit flow rate of the cross-section CS_2 are shown as an illustration of the procedure. The quadratic polynomial $f(x) = c_0 + c_1\,x + c_2\,x^2$ is used as the trend line. The fitting procedure is carried out using the least-square fitting to determine c_0, c_1, and c_2. The derivatives $\frac{\partial H}{\partial x}$ and $\frac{\partial^2(UH)}{\partial x^2}$ are evaluated by differentiating the function $f(x)$. Note that the measured distance to the outer bank ℓ is used as the cross-stream direction x.

Manning's formula is used to estimate the energy slope (S_f) from the mean velocity $V = Q/A$ with the flow discharge Q and the cross-sectional area A as:

$$S_f = \frac{(Vn)^2}{R_h^{4/3}} \tag{4.23}$$

Here the hydraulic radius (R_h) and the roughness coefficient n are computed as follows.

A one-dimensional HEC-RAS model is developed for the river reach to determine R_h and n using the DTM. The rating curve (Q, H) at the United States Geological Survey (USGS) at the Fargo (05054000) station is used to calibrate the value of Manning's n under the open-surface condition. The roughness coefficient is estimated for the bankfull condition as $n \approx 0.0166$. Accordingly, the average energy slope for the entire river reach is estimated as $S_f = 6.9 \times 10^{-6}$. The depth-averaged eddy viscosity ν_t is estimated ((Vionnet et al., 2004)) as $\nu_t = 10^{-6}\ m^2/s$.

The validity of the theoretical model is tested in the cross-sections CS_1, CS_2, CS_3, and CS_4 as shown in Figure 4.12. The theoretical value of $u_b^\star$ is calculated using the Equation 4.22 using the guided value of λ in the range from 0.45 to 2.0, which is observed in Table 4.3. At the channel center from (CS_1 to CS_4), the theoretical model predicts well the variation of $u_b^\star$ given the bounds of λ. The model captures well the upper and lower bounds of $u_b^\star$ and their trends as evidently in Figure 4.12. In particular, the proposed theory is able to capture the elevated values of $u_b^\star$, which is at the level of ($0.0150\ m/s$) and the lowest values ($\approx 0.005\ m/s$). The impact of the channel curvature can be seen as the magnitude of the measured shear velocity is significantly larger near the outer bank. The theoretical model fails to capture this feature. The model underpredicts $u_b^\star$ near the outer bank ($CS_3 - 1$ and $CS_4 - 1$) significantly.

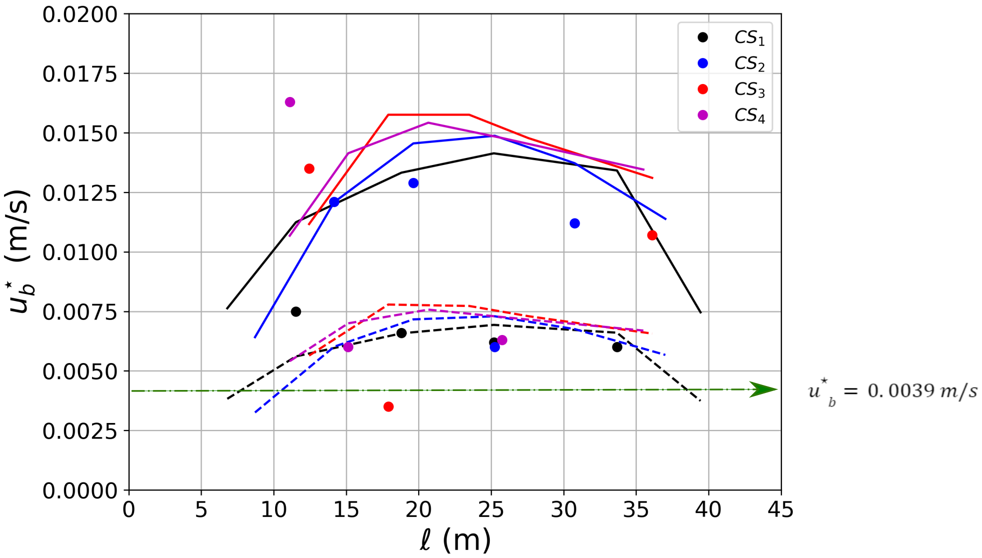

Figure 4.12. The comparison between the cross-stream momentum model (Equation 4.22) and the measured cross-stream shear velocity profile in the river reach. The bed shear velocity ($u_b^\star$) is computed from the logarithmic fitting for the cross-sections CS_1, CS_2, CS_3, and CS_4 (see Table 4.2). The predicted values are generated using two different values of λ (Equation 4.22 and $u_b^\star = \sqrt{\frac{\tau_b}{\rho}}$) for each cross-section: (i) $\lambda_{min} = 0.45$ (solid lines); and (ii) $\lambda_{max} = 2.0$ (dashed lines). The range of λ is selected from the quartic solution fitting of the measurements (Table 4.3). The value of $u_b^\star$ (green dash-dotted line) is calculated with $u_b^\star = V\sqrt{\frac{f}{8}}$ (see Equation 4.24).

4.5. Discussion

Cross-stream momentum transfer plays an important role in regulating the river width via the modulation of the sediment flux (Abramian et al., 2020). The sediment transport is balanced out in the bank region under the equilibrium condition where the gravity force and the bed shear stress equate to each other (Phillips & Jerolmack, 2016; Popović et al., 2021). In ice-covered rivers, the roughness of the ice layer adds further complexities by introducing the shear stress in the ice layer (τ_i) and altering one in the bed layer (τ_b) (Guo et al., 2017). Most previous works have not considered the impact of ice cover on the cross-stream momentum transfer. Our work develops a framework to investigate the cross-stream distribution of τ_i and τ_b, which is important in regulating the morphology of rivers in cold regions (Gautier et al., 2021).

4.5.1. The impacts of ice cover on the vertical profiles

The two-layer hypothesis (see also Figure 4.3) assumes the presence of two logarithmic profiles near the bed and ice layers concurrently (A. Sukhodolov et al., 1999). This has been the main approach to describe the velocity distribution along the depth in many studies (Attar & Li, 2012, 2013; Urroz & Ettema, 1994a). Since the applicability of the logarithmic method is based on the availability of the data near the surface, the problem of signal interference is critically important. As our previous work indicated, obtaining flow data under the ice-covered condition is challenging due to the signal interference near both boundaries (see also Figure 4.4) (Koyuncu et al., 2021). This challenge dictates the logarithmic fitting for both the ice and the bed layers at the same vertical. As illustrated in Table 4.2, there are only few verticals where both logarithmic layers exist ($CS_1 - 5$, $CS_2 - 4$, $CS_2 - 6$, $CS_3 - 1$, and $CS_4 - 1$). The reason for this challenge can be further investigated in the wall units (z^+, u^+). As shown in Figure 4.8a and b, the first available point is located for logarithmic fitting around $\mid z \mid^+ = 1,100$ in wall units. The last available point is typically less than $z^+ < 5,000$, which is approximately less than 20% of the total depth (H). The logarithmic fitting requires a sufficient number of data points to fall into this range of $1,100 < \mid z \mid^+ < 5,000$ (Petrie & Diplas, 2016). In practice, this requirement prohibits an acceptable fitting in many verticals as demonstrated in Table 4.2. Therefore, the logarithmic fitting is not a robust method to determine $u_i^\star$ and $u_b^\star$.

In addition to the data requirement, the main limitation of the two-layer hypothesis is that it introduces a discontinuous velocity gradient at the location of u_{max}. As shown in

Figure 4.7, the two-layer hypothesis cannot capture the profile because the two logarithmic profiles do not intersect at the maximum velocity location. The quartic profile is introduced to alleviate this shortcoming via the use of all velocity data in the mixing core (mid-depth) as depicted in Figure 4.7(b) (Guo et al., 2017). The quartic profile provides an excellent model for the ice-covered flows as shown in Figure 4.9 at all ice holes. Despite the missing data near the river bed layer (approximately 0.5 m), the quartic profile can follow the measured data closely with $R^2 > 0.9$ in most cases (see Table 4.3). This is remarkable given that the quartic profile needs a minimal number of fitting parameters such as λ and α.

The impact of banks on the vertical profile is evident as shown in Figure 4.9. Field measurement has demonstrated the impact of banks on altering the vertical profiles under the open-surface condition (Chauvet et al., 2014). A similar phenomenon is observed in this study since the profiles are altered as they are closer to the banks. Near the thalweg ($CS_1 - 3, CS_2 - 4$), the profiles are nearly symmetrical. Near banks, the location of u_{max} is closer to the ice layer. As shown in the Table 4.3, the value of $\lambda = \frac{u_i^\star}{u_b^\star}$ varies significantly from one vertical to another. As shown in Table 4.3, the value of λ is typically less than 1.0 in the thalweg region but it can reach 2.0 in the bank region. Hence the bank has a critical role in regulating the vertical profile and the shear stresses.

4.5.2. The three-dimensional structures of flow in the ice-covered bend

To date, our understanding of ice-covered flows in rivers is limited (Lotsari et al., 2017). Most of the previous works are carried out in laboratory conditions (Ettema, 2002; Urroz & Ettema, 1994a; F. Wang et al., 2020). There are a limited number of field measurements for small ice-covered rivers (Demers et al., 2011; Lotsari et al., 2017; A. Sukhodolov et al., 1999). The most prominent feature of ice-covered flows in bends is found in laboratory conditions in which the vertical profiles possess two points of inflections (Tsai & Ettema, 1996; Urroz & Ettema, 1994a). Field measurement of Urroz and Ettema, 1994a confirms that this feature indeed exists in a natural bend as "double-stacked vortices" (Demers et al., 2011). The laboratory experiment of (Urroz & Ettema, 1994a) suggests that the flow structures consist of two counter-rotating circulations as opposed to a single one in the open-surface condition. The field measurement of Demers et al., 2011 further clarifies that the spatial extent of these double-stacked vortices is limited in the bend apex. Field data of (Lotsari et al., 2017) confirms that the presence of the double-stacked vortices is sensitive to the water depth since these vortices disappear under low flow conditions. Similar field measurements have not been carried out for medium-sized and large rivers to investigate the structure of these vortices.

From the measurements of secondary flows in Figure 4.10, it is possible to reconstruct the three-dimensional structure of the ice-covered flow in the studied bend as shown in Figure 4.13. In general, the flow consists of longitudinal circulations that rotate in the opposite direction to each other. Two helical circulations are found near the banks in addition to a counter-clockwise rotation in the thalweg. Near the bend apex, the double-stacked vortices appear intermittently between CS_2 and CS_3. The double-stacked vortices seem to merge at CS_4 as the flow exits the bend. In brief, the three-dimensional flow structures are organized as separate helical flows and they interact with each other along the bend.

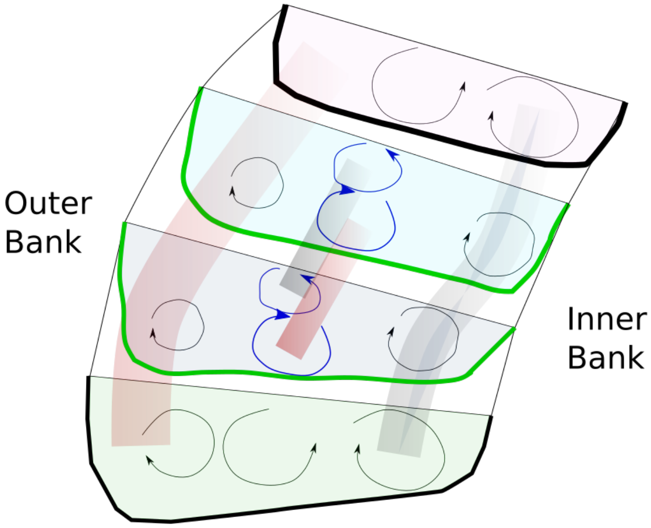

Figure 4.13. The hypothesized three-dimensional structure of the flow in the ice-covered bend. Two clockwise rotations are located near the outer and inner banks, respectively. The double-stacked vortices appear near the bend apex.

In general, our three-dimensional flow model agrees well with the field observations of Demers et al., 2011 and Lotsari et al., 2017. As shown in Figure 4.6, Figure 4.7, and Figure 4.9, the ice cover directs the high-velocity core toward the outer bend and the mid-depth at the same time as reported in Demers et al., 2011. In addition, the intermittent presence of the double-stacked vortices near the bend apex is almost identical to one in the observation of (Demers et al., 2011; Lotsari et al., 2017). Interestingly, our results also confirm the transition of the double-stacked vortices toward a single vortex structure at the bend exit (Demers et al., 2011).

Our field data further indicates that the three-dimensional flow structures are more complicated than the model of (Lotsari et al., 2017). In addition to the main circulation in the thalweg, there exist two additional circulations near banks. Note that the presence of multiple circulations in one cross-section has been reported in previous field measurements

(Chauvet et al., 2014). Here the thalweg circulation is the classical secondary flow, which is driven by the channel curvature. However, the other circulations are driven by turbulence anisotropy (Kang & Sotiropoulos, 2011). Due to the three-dimensional structure of the flow, it is challenging to capture the dynamics of these vortices at all cross-sections as shown in Figure 4.10 as it requires the period of measurement (T) to be sufficiently large. In previous works, the presence of the bank vortices is not reported (Demers et al., 2011; Lotsari et al., 2017). The absence of the bank vortices in these studies might be due to the difference in the stream depth. The measurements of Lotsari et al., 2017 and Demers et al., 2011 are carried out for shallow bends (approximately $1.5 - 2\ m$) whereas the maximum depth of the current bend is approximately $4\ m$, which is significantly deeper. Thus, both the flow depth and the bend curvature could play important roles in regulating the emergence of helical motions in ice-covered bends (Lotsari et al., 2017). We hypothesize that the double-stacked vortices only appear in the region where the flow depth reaches a critical threshold.

4.5.3. The cross-stream momentum equation

The traditional approach in river hydraulics considers only the ice-free condition and ignores the bank effects (e.g. $u_b^\star \approx \sqrt{gHS}$) (Phillips & Jerolmack, 2016). To provide a similar method to estimate the numerical value of $u_b^\star$ under ice cover, we propose the use of Haaland's equation (friction method) for a closed duct as:

$$\frac{1}{\sqrt{f}} = -1.8log\left[\left(\frac{(2.95d_{84})/(4R_h)}{3.7}\right)^{1.11} + \frac{6.9}{Re}\right] \tag{4.24}$$

where Re, R_h, and f are the Reynolds number ($Re = \frac{V(4R_h)}{\mu}$), the hydraulic radius, and the friction coefficient, respectively. Here $d_{84} = 0.00288m$ is the sediment particle size of the Red River in Fargo (Galloway & Nustad, 2012). Following the computation of f, the shear velocity near the channel bed is calculated ($u_b^\star = V\sqrt{\frac{f}{8}}$) (Finnemore & Franzini, 2002) and represented in Figure 4.12. Using this formula, the estimated $u_b^\star$ value is computed as 0.0039 m/s. As seen in Figure 4.12, this value is in the range of our field observation (lower bound), which generally agrees with the estimated values from the quartic solution (see Table 4.3). However, this is a single value for the entire cross-section and thus the cross-stream distribution of the bed shear stress cannot be generated.

In contrast to the above-mentioned approach, the equation 4.22 shows that the presence of the ice cover complicates the bed shear stress distribution by introducing the effect of bank slope, the local flow turbulence, and the distortion of the vertical profile (λ). Thus, the Equation 4.22 can be used to estimate the bed shear stress under the ice-covered condition in any location in the cross-section.

The significant contribution of the Equation 4.22 is that it also establishes the linkage between τ_i and τ_b. It is an alternative method to compute the τ_i if the value of τ_b is available via either the logarithmic or quartic method. In addition, the roles of the cross-section shape $H(x)$ and the unit flow rate profile $U_2H(x)$ are evident in bed shear stress distribution (see Figure 4.11). The presence of the bank slope dictates the bed shear stress via the term $\frac{\partial H}{\partial x}$. The cross-sectional flow profile ($U_2(x)$) plays a role in distributing the momentum via turbulent stress. Therefore, these terms become significant in regulating the bed shear stress near banks where their gradients are large. These effects can be observed as the value of $u_b^\star$ is elevated near banks as evident in Table 4.3.

To test the sensitivity of the $u_b^\star$ calculation to the choice of the representation of $H(x)$, a 4^{th} degree polynomial is also used to fit the geometrical form of $H(x)$ (see Figure 4.11a).

Our results show that the 4^{th} degree polynomial does not provide significant improvements in terms of capturing the location of the thalweg. Therefore, our results indicate that a 2^{nd} order polynomial is sufficient to capture the geometrical shape of the cross-sections in the current study.

Note that the cross-stream momentum equation A.10 is a model that relates the shear stresses on the bed and the ice cover layers. Therefore, our model for lateral momentum transfer has several limitations. First, we assume that the channel curvature has no effect since the variation of the streamwise component of the velocity has been ignored $\frac{\partial u}{\partial y} = 0$. Natural rivers often follow a meandering path that changes the flow structure by shifting the position of the main flow and thalweg towards the outer bank. This pattern generates a high-shear stress region near the outer bank (Koyuncu et al., 2021). Indeed, the skewed distribution of depth-averaged velocity $U(x)$ is observed in the cross-sections CS_1, CS_2, CS_3, and CS_4 (Figure 4.6). This skewed distribution affects the ability of the model to capture the bed shear stress near the outer bank in cross-sections CS_3 and CS_4 (see Figure 4.12). Here, the model fails to capture the large bed shear stress near the outer bank at stations $CS_3 - 1$ and $CS_4 - 1$ due to the sharp curvature of the channel. Furthermore, our model assumes that the ice layer is completely flat across one cross-section ($\frac{\partial z_{ice}}{\partial x} = 0$ at $z = 0$). However, there could be a cross-stream slope between the surface elevation of the inner and outer banks (super-elevation effect in a meander bend). Thus, our Equation 4.22 must be modified to account for such an effect. In addition, the number of ice holes in a cross-section must be increased to increase the accuracy of the fitting procedure for $H(x)$ and $UH(x)$ as seen in Figure 4.11. Nevertheless, the proposed model can provide a reasonable estimation in the range of $u_b^\star$ in the ice-covered reach using available inputs such as the energy slope

S_f and the range of λ. Our future efforts will be made to refine the assumptions to improve the estimation for τ_b.

4.6. Conclusion

We study the three-dimensional structure of flows in an ice-covered bend of the Red River, North Dakota, in the United States. Field measurements were carried out to obtain flow velocity data in a river reach of the Red River. Our study revealed the importance of ice coverage on the bed shear stress by regulating the velocity profile. Based on field data, we developed a mathematical model for the cross-stream momentum transfer in ice-covered rivers in general. Our model also emphasizes the importance of flow dynamics near banks as the flow profiles are altered significantly in shallow areas under ice coverage. As a result, the cross-sectional distribution of the bed shear stress is highly dependent on the distance to banks. Our theoretical model and field data show a significant increase in bed shear stress near both banks.

Our main conclusions are:

- It is challenging to apply the two-layer hypothesis to the study area. In most cases, the logarithmic layers are not observed at the same vertical using our fitting methodology.
- The quartic profile provides a robust method to estimate the bed shear stress under the ice-covered condition. However, the quartic profile underestimates the bed shear stress.
- We propose a simple formula to compute the cross-stream distribution of bed shear stress under the ice-covered condition. Using this formula and our field measurement data, we show that the bed shear stress is significantly affected by the ice cover, especially in the bank regions.

- Our field data shows that the secondary flow pattern under the ice-covered condition might be more complicated than previously thought. The double-stacked vortices are observed at the bend apex. Their locations agree with the previous works (Demers et al., 2011; Lotsari et al., 2017). However, additional helical cells also exist as separate longitudinal structures along the river reach.

5. SUMMARY AND FUTURE WORK

The main contribution of this dissertation is to represent a significant advancement in our understanding of the complex interactions between ice cover and flow dynamics in channel flows. Through a multidisciplinary approach encompassing theoretical modeling, numerical simulations, and field observations, this research has unraveled detailed insights into the behavior of ice-covered flows and their implications for hydraulic processes. As we reflect on the findings from each chapter, it becomes evident that the interplay between ice cover and flow dynamics is both complex and diverse, presenting challenges and opportunities for further exploration and practical application.

In the first chapter, the complex phenomenon of river ice, including its formation processes, societal and financial impacts, effects on flow dynamics, and challenges in measurement techniques are explored. Understanding the complexities of river ice formation, its interactions with flow dynamics, and implementing effective measurement methodologies are essential for predicting and mitigating adverse impacts. Furthermore, this chapter delves into the complex mechanics of freeze-up and breakup stages, as well as the effects of river ice on three-dimensional flow structures such as secondary flow and shear velocity. This chapter underscores the critical importance of comprehensively understanding river ice dynamics to address the associated environmental, societal, and economic consequences.

In the second chapter, a pioneering SKM-based method for computing depth-averaged velocity profiles in ice-covered flows is introduced, differentiated, and thoroughly validated in a straight trapezoidal channel and a meandering natural channel. Utilizing a combination of numerical simulations, field data, and previously performed laboratory experiments, this method demonstrates remarkable adaptability in its applicability to natural channels with irregular cross-sections. However, as demonstrated by the research findings, the method's efficacy is most pronounced in straight river reaches, with potential inaccuracies arising in complex river bends. This finding underscores the need for continued refinement and adaptation of computational techniques to accommodate the diverse hydraulic regimes encountered in riverine environments.

Building upon the foundation laid in the second chapter, the third chapter delves deeper into the impacts of ice coverage on velocity profiles in river bends. Through meticulous analysis of ADCP data, supplemented by theoretical investigations, a nuanced understanding of the vertical flow structure and bed shear velocity alterations under ice cover emerges. While the classical logarithmic law for velocity profiles near the river bed proves to be inadequate under ice-covered conditions, the exploration of alternative methodologies, such as the quartic solution, offers promising avenues for accurate estimation of bed shear stresses. Furthermore, the spatial redistribution of bed shear stress, characterized by elevated values near both banks under ice cover, underscores the intricate interplay between ice-induced alterations in flow dynamics and sediment transport processes.

In the fourth chapter, the research shifts focus to field measurements conducted in an ice-covered bend of the Red River, North Dakota, offering valuable insights into how ice cover affects flow dynamics in real-world settings. By examining the complex three-dimensional structure of flows and cross-stream momentum transfer, this chapter contributes to our understanding of ice-covered river systems from a comprehensive perspective. The observed increase in bed shear stress near both riverbanks emphasizes the importance of flow dynamics in shallow areas, where ice cover significantly influences hydraulic processes. Additionally, the discovery of double-stacked vortices and additional helical cells along the river reach challenges traditional ideas about secondary flow patterns under ice-covered conditions, highlighting the need for further investigation into the complexities of flow behavior in cold regions.

In summary, this dissertation makes a significant contribution to the study of ice-covered flows, introducing innovative methodologies, deep insights, and practical implications for hydraulic engineering and environmental management in cold regions. By clarifying the intricate relationship between ice cover and flow dynamics in river bends, this research sets the stage for informed decision-making and adaptive strategies to mitigate the effects of ice cover on river ecosystems and infrastructure. Looking ahead, the findings presented here stimulate further exploration and innovation, aiming for sustainable solutions to manage ice-covered river systems in a changing climate. To delve deeper into these topics, we outline several potential research directions that can expand upon the work presented in this thesis. These areas of interest include:

- Modifying the SKM-based method to consider the meandering impact in natural channels under ice cover. This approach will increase the applicability of the method and contribute to the understanding of the meandering formation in riverine systems during winter seasons.
- Integration of LES to model meandering river flow over complex topography. A comprehensive numerical simulation of ice-covered river flow tends to increase the knowledge of three-dimensional flow structures to address larger consequences such as ice-jam-related spring floods and erosion risks.

- Outer bank focused lateral shear stress and secondary flow pattern analysis is promising a valuable insight to address sediment movement in the vicinity of the HVC at the bend apex.
- Investigating the shear velocity distribution in shallow waters (i.e., inner bank of the Red River, Buffalo River) by employing the ADV to confirm the increase in the lateral shear velocity profile our observations displayed. Hence, the unexpected scour and erosion risks could be identified.

REFERENCES

Abad, J. D., & Garcia, M. H. (2009). Experiments in a high-amplitude kinoshita meandering channel: 1. implications of bend orientation on mean and turbulent flow structure. *Water Resources Research*, *45*(2).

Abramian, A., Devauchelle, O., & Lajeunesse, E. (2020). Laboratory rivers adjust their shape to sediment transport. *Physical Review E*, *102*(5), 053101.

Ackers, P. (1991). Hydraulic design of straight compound channels. volume 1-summary and design method, volume 2-appendices.

Afzalimehr, H., & Rennie, C. (2009). Determination of bed shear stress using boundary layer parameters in a gravel-bed river. *Hydrological Sciences Journal*, *54*(1), 147–159.

Albayrak, I., & Lemmin, U. (2011). Secondary currents and corresponding surface velocity patterns in a turbulent open-channel flow over a rough bed. *Journal of Hydraulic Engineering*, *137*(11), 1318–1334.

Anisimov, O. (2007). Potential feedback of thawing permafrost to the global climate system through methane emission. *Environmental Research Letters*, *2*(4), 045016.

Anisimov, O., Fitzharris, B., Hagen, J., Jefferies, R., Marchant, H., Nelson, F., Prowse, T., & Vaughan, D. (2001). Polar regions (arctic and antarctic). *Climate change*, 801–841.

Anwar, H. O. (1986). Turbulent structure in a river bend. *Journal of hydraulic engineering*, *112*(8), 657–669.

Arnell, N. W. (1999). The effect of climate change on hydrological regimes in europe: A continental perspective. *Global environmental change*, *9*(1), 5–23.

Ashton, G. D. (1986). *River and lake ice engineering*. Water Resources Publication.

Ashworth, P., & Ferguson, R. (1986). Interrelationships of channel processes, changes and sediments in a proglacial braided river. *Geografiska Annaler: Series A, Physical Geography*, *68*(4), 361–371.

Attar, S., & Li, S. (2012). Data-fitted velocity profiles for ice-covered rivers. *Canadian Journal of Civil Engineering*, *39*(3), 334–338.

Attar, S., & Li, S. (2013). Momentum, energy and drag coefficients for ice-covered rivers. *River Research and Applications*, *29*(10), 1267–1276.

Bagherimiyab, F., & Lemmin, U. (2013). Shear velocity estimates in rough-bed open-channel flow. *Earth surface processes and landforms*, *38*(14), 1714–1724.

Barnes, H. H. (1967). *Roughness characteristics of natural channels*. US Government Printing Office.

Bathurst, J. C., Hey, R. D., & Thorne, C. R. (1979). Secondary flow and shear stress at river bends. *Journal of the Hydraulics Division*, *105*(10), 1277–1295.

Beltaos, S. (2000). Advances in river ice hydrology. *Hydrological processes*, *14*(9), 1613–1625.

Beltaos, S., & Prowse, T. (2009). River-ice hydrology in a shrinking cryosphere. *Hydrological Processes: An International Journal*, *23*(1), 122–144.

Beltaos, S., & Prowse, T. D. (2001). Climate impacts on extreme ice-jam events in canadian rivers. *Hydrological Sciences Journal*, *46*(1), 157–181.

Bennett, K., & Prowse, T. (2010). Northern hemisphere geography of ice-covered rivers. *Hydrological Processes: An International Journal*, *24*(2), 235–240.

Biron, P., De Serres, B., Roy, A., & Best, J. L. (1993). Shear layer turbulence at an unequal depth channel confluence. In *Turbulence: Perspectives on flow and sediment transfer* (pp. 197–213). John Wiley & Sons, Ltd.

Biron, P. M., Buffin-Bélanger, T., & Martel, N. (2019). Three-dimensional turbulent structures at a medium-sized confluence with and without an ice cover. *Earth Surface Processes and Landforms*, *44*(15), 3042–3056.

Biron, P. M., Lane, S. N., Roy, A. G., Bradbrook, K. F., & Richards, K. S. (1998). Sensitivity of bed shear stress estimated from vertical velocity profiles: The problem of sampling resolution. *Earth Surface Processes and Landforms: The Journal of the British Geomorphological Group*, *23*(2), 133–139.

Biron, P. M., Robson, C., Lapointe, M. F., & Gaskin, S. J. (2004). Comparing different methods of bed shear stress estimates in simple and complex flow fields. *Earth Surface Processes and Landforms: The Journal of the British Geomorphological Research Group*, *29*(11), 1403–1415.

Blanchard, R. A., Ellison, C. A., Galloway, J. M., & Evans, D. A. (2011). *Sediment concentrations, loads, and particle-size distributions in the red river of the north and selected tributaries near fargo, north dakota, during the 2010 spring high-flow event* (tech. rep.). U. S. Geological Survey.

Blanckaert, K., & De Vriend, H. J. (2005). Turbulence characteristics in sharp open-channel bends. *Physics of Fluids*, *17*(5), 055102.

Blanckaert, K., Duarte, A., & Schleiss, A. J. (2010). Influence of shallowness, bank inclination and bank roughness on the variability of flow patterns and boundary shear stress due to secondary currents in straight open-channels. *Advances in Water Resources*, *33*(9), 1062–1074.

Blanckaert, K., & Graf, W. H. (2001). Mean flow and turbulence in open-channel bend. *Journal of Hydraulic Engineering*, *127*(10), 835–847.

Brayall, M., & Hicks, F. (2012). Applicability of 2-d modeling for forecasting ice jam flood levels in the hay river delta, canada. *Canadian Journal of Civil Engineering*, *39*(6), 701–712.

Bridge, J. S., & Jarvis, J. (1976). Flow and sedimentary processes in the meandering river south esk, glen clova, scotland. *Earth surface processes*, *1*(4), 303–336.

Bridge, J. S., & Jarvis, J. (1977). Velocity profiles and bed shear stress over various bed configurations in a river bend. *Earth Surface Processes*, *2*(4), 281–294.

Bridge, J., & Jarvis, J. (1982). The dynamics of a river bend: A study in flow and sedimentary processes. *Sedimentology*, *29*(4), 499–541.

Buffin-Bélanger, T., & Roy, A. G. (2005). 1 min in the life of a river: Selecting the optimal record length for the measurement of turbulence in fluvial boundary layers. *Geomorphology*, *68*(1-2), 77–94.

Bushuk, M., Holland, D. M., Stanton, T. P., Stern, A., & Gray, C. (2019). Ice scallops: A laboratory investigation of the ice–water interface. *Journal of fluid mechanics*, *873*, 942–976.

Calderer, A., Yang, X., Angelidis, D., Khosronejad, A., Le, T., Kang, S., Gilmanov, A., Ge, L., & Borazjani, I. (2015). *Virtual flow simulator* (tech. rep.). Univ. of Minnesota, Minneapolis, MN (United States).

Chassiot, L., Lajeunesse, P., & Bernier, J.-F. (2020). Riverbank erosion in cold environments: Review and outlook. *Earth-Science Reviews*, *207*, 103231.

Chaudhry, M. H. (2007). *Open-channel flow*. Springer Science & Business Media.

Chauvet, H., Devauchelle, O., Métivier, F., Lajeunesse, E., & Limare, A. (2014). Recirculation cells in a wide channel. *Physics of Fluids*, *26*(1), 016604.

Chen, G., Gu, S., Li, B., Zhou, M., & Huai, W. (2018). Physically based coefficient for streamflow estimation in ice-covered channels. *Journal of hydrology*, *563*, 470–479.

Constantinescu, G., Kashyap, S., Tokyay, T., Rennie, C., & Townsend, R. (2013). Hydrodynamic processes and sediment erosion mechanisms in an open channel bend of strong curvature with deformed bathymetry. *Journal of Geophysical Research: Earth Surface*, *118*(2), 480–496.

Constantinescu, G., Koken, M., & Zeng, J. (2011). The structure of turbulent flow in an open channel bend of strong curvature with deformed bed: Insight provided by detached eddy simulation. *Water Resources Research*, *47*(5).

Demers, S., Buffin-Bélanger, T., & Roy, A. (2011). Helical cell motions in a small ice-covered meander river reach. *River research and applications*, *27*(9), 1118–1125.

Demers, S., Buffin-Bélanger, T., & Roy, A. G. (2013). Macroturbulent coherent structures in an ice-covered river flow using a pulse-coherent acoustic doppler profiler. *Earth Surface Processes and Landforms*, *38*(9), 937–946.

Devauchelle, O., Popović, P., & Lajeunesse, E. (2022). Viscous transfer of momentum across a shallow laminar flow. *Journal of Fluid Mechanics*, *932*.

Devi, K., Das, B. S., Khuntia, J. R., & Khatua, K. K. (2021). Analytical solution for depth-averaged velocity and boundary shear in a compound channel. *Proceedings of the institution of civil engineers-water management*, *174*(3), 143–158.

Devi, K., & Khatua, K. K. (2020). Boundary shear distribution in a compound channel with differential roughness. *Proceedings of the institution of civil engineers-water management*, *173*(6), 274–292.

Dietrich, W. E., & Smith, J. D. (1984). Bed load transport in a river meander. *Water Resources Research*, *20*(10), 1355–1380.

Einstein, H. A. (1942). Formulas for the transportation of bed load. *Transactions of the American Society of Civil Engineers*, *107*(1), 561–577.

Engel, F. L., & Rhoads, B. L. (2016). Three-dimensional flow structure and patterns of bed shear stress in an evolving compound meander bend. *Earth Surface Processes and Landforms*, *41*(9), 1211–1226.

Ervine, D. A., Babaeyan-Koopaei, K., & Sellin, R. H. (2000). Two-dimensional solution for straight and meandering overbank flows. *Journal of Hydraulic Engineering*, *126*(9), 653–669.

Ettema, R. (2002). Review of alluvial-channel responses to river ice. *Journal of Cold Regions Engineering*, *16*(4), 191–217.

Ettema, R., & Daly, S. F. (2004). Sediment transport under ice.

Ferguson, R., & Ashworth, P. (1992). Spatial patterns of bedload transport and channel change in braided and near-braided rivers. *Dynamics of Gravel-Bed Rivers; Billi, P., Hey, RD, Thorne, CR, Tacconi, P., Eds.*

Ferreira da Silva, A. M., & Ebrahimi, M. (2017). Meandering morphodynamics: Insights from laboratory and numerical experiments and beyond. *Journal of Hydraulic Engineering*, *143*(9), 03117005.

Finnemore, E. J., & Franzini, J. B. (2002). *Fluid mechanics with engineering applications*. McGraw-Hill Education.

Flack, K. A., & Schultz, M. P. (2010). Review of hydraulic roughness scales in the fully rough regime. *Journal of Fluids Engineering*, *132*(4).

Galloway, J. M., & Nustad, R. A. (2012). *Sediment loads in the red river of the north and selected tributaries near fargo, north dakota, 2010—2011* (tech. rep.). US Geological Survey.

Gao, W., Cheng, W., & Samtaney, R. (2020). Large-eddy simulations of turbulent flow in a channel with streamwise periodic constrictions. *Journal of Fluid Mechanics*, *900*.

Gautier, E., Dépret, T., Cavero, J., Costard, F., Virmoux, C., Fedorov, A., Konstantinov, P., Jammet, M., & Brunstein, D. (2021). Fifty-year dynamics of the lena river islands (russia): Spatio-temporal pattern of large periglacial anabranching river and influence of climate change. *Science of The Total Environment*, *783*, 147020. https://doi.org/https://doi.org/10.1016/j.scitotenv.2021.147020

Ge, L., & Sotiropoulos, F. (2007). A numerical method for solving the 3d unsteady incompressible navier–stokes equations in curvilinear domains with complex immersed boundaries. *Journal of computational physics*, *225*(2), 1782–1809.

Ghareh Aghaji Zare, S., Moore, S. A., Rennie, C. D., Seidou, O., Ahmari, H., & Malenchak, J. (2016). Estimation of composite hydraulic resistance in ice-covered alluvial streams. *Water Resources Research*, *52*(2), 1306–1327.

Guo, J. (2017). Eddy viscosity and complete log-law for turbulent pipe flow at high reynolds numbers. *Journal of Hydraulic Research*, *55*(1), 27–39.

Guo, J., Shan, H., Xu, H., Bai, Y., & Zhang, J. (2017). Exact solution for asymmetric turbulent channel flow with applications in ice-covered rivers. *Journal of Hydraulic Engineering*, *143*(10), 04017041.

Hanjalić, K., & Launder, B. (1972). Fully developed asymmetric flow in a plane channel. *Journal of Fluid Mechanics*, *51*(2), 301–335.

Heathershaw, A. (1979). The turbulent structure of the bottom boundary layer in a tidal current. *Geophysical Journal International*, *58*(2), 395–430.

Hicks, F. (2009). An overview of river ice problems: Cripe07 guest editorial. *Cold Regions Science and Technology*, *55*(2), 175–185.

Hurther, D., & Lemmin, U. (2000). Shear stress statistics and wall similarity analysis in turbulent boundary layers using a high-resolution 3-d advp. *IEEE journal of oceanic engineering*, *25*(4), 446–457.

Jones, J. (1999). Climate change and sustainable water resources: Placing the threat of global warming in perspective. *Hydrological Sciences Journal*, *44*(4), 541–557.

Kämäri, M., Alho, P., Veijalainen, N., Aaltonen, J., Huokuna, M., & Lotsari, E. (2015). River ice cover influence on sediment transportation at present and under projected hydroclimatic conditions. *Hydrological Processes*, *29*(22), 4738–4755.

Kang, S., Hill, C., & Sotiropoulos, F. (2016). On the turbulent flow structure around an instream structure with realistic geometry. *Water Resources Research*, *52*(10), 7869–7891.

Kang, S., Lightbody, A., Hill, C., & Sotiropoulos, F. (2011). High-resolution numerical simulation of turbulence in natural waterways. *Advances in Water Resources*, *34*(1), 98–113.

Kang, S., & Sotiropoulos, F. (2011). Flow phenomena and mechanisms in a field-scale experimental meandering channel with a pool-riffle sequence: Insights gained via numerical simulation. *Journal of Geophysical Research: Earth Surface*, *116*(F3).

Kang, S., & Sotiropoulos, F. (2012a). Assessing the predictive capabilities of isotropic, eddy viscosity reynolds-averaged turbulence models in a natural-like meandering channel. *Water Resources Research*, *48*(6).

Kang, S., & Sotiropoulos, F. (2012b). Numerical modeling of 3d turbulent free surface flow in natural waterways. *Advances in water resources*, *40*, 23–36.

Kempema, E. W., Reimnitz, E., & Barnes, P. W. (2001). Anchor-ice formation and ice rafting in southwestern lake michigan, usa. *Journal of Sedimentary Research*, *71*(3), 346–354.

Kempema, E., Reimnitz, E., Clayton Jr, J., & Payne, J. (1993). Interactions of frazil and anchor ice with sedimentary particles in a flume. *Cold Regions Science and Technology*, *21*(2), 137–149.

Khosronejad, A., Hill, C., Kang, S., & Sotiropoulos, F. (2013). Computational and experimental investigation of scour past laboratory models of stream restoration rock structures. *Advances in water resources*, *54*, 191–207.

Khosronejad, A., Kang, S., Borazjani, I., & Sotiropoulos, F. (2011). Curvilinear immersed boundary method for simulating coupled flow and bed morphodynamic interactions due to sediment transport phenomena. *Advances in water resources*, *34*(7), 829–843.

Khosronejad, A., Kang, S., & Sotiropoulos, F. (2012). Experimental and computational investigation of local scour around bridge piers. *Advances in Water Resources*, *37*, 73–85.

Khosronejad, A., Kozarek, J. L., Palmsten, M. L., & Sotiropoulos, F. (2015). Numerical simulation of large dunes in meandering streams and rivers with in-stream rock structures. *Advances in water resources*, *81*, 45–61.

Khosronejad, A., Le, T., DeWall, P., Bartelt, N., Woldeamlak, S., Yang, X., & Sotiropoulos, F. (2016). High-fidelity numerical modeling of the upper mississippi river under extreme flood condition. *Advances in Water Resources*, *98*, 97–113. https://doi.org/https://doi.org/10.1016/j.advwatres.2016.10.018

Khosronejad, A., & Sotiropoulos, F. (2014). Numerical simulation of sand waves in a turbulent open channel flow. *Journal of Fluid Mechanics*, *753*, 150–216.

Kirillin, G., Leppäranta, M., Terzhevik, A., Granin, N., Bernhardt, J., Engelhardt, C., Efremova, T., Golosov, S., Palshin, N., Sherstyankin, P., et al. (2012). Physics of seasonally ice-covered lakes: A review. *Aquatic sciences*, *74*(4), 659–682.

Knoll, L. B., Sharma, S., Denfeld, B. A., Flaim, G., Hori, Y., Magnuson, J. J., Straile, D., & Weyhenmeyer, G. A. (2019). Consequences of lake and river ice loss on cultural ecosystem services. *Limnology and Oceanography Letters*, *4*(5), 119–131.

Koken, M., Constantinescu, G., & Blanckaert, K. (2013). Hydrodynamic processes, sediment erosion mechanisms, and reynolds-number-induced scale effects in an open channel bend of strong curvature with flat bathymetry. *Journal of Geophysical Research: Earth Surface*, *118*(4), 2308–2324.

Kolerski, T. (2014). Modeling of ice phenomena in the mouth of the vistula river. *Acta Geophysica*, *62*(4), 893–914.

Koyuncu, B., & Le, T. (2020). Secondary flow structures in natural channels under open and ice-coverage conditions. *APS Division of Fluid Dynamics Meeting Abstracts*, P16–001.

Koyuncu, B., & Le, T. (2021). Impacts of ice coverage on velocity profiles in a bend. *AGU Fall Meeting Abstracts*, *2021*, EP15E–1362.

Koyuncu, B., Le, T., Team, B. K., & Le Team, T. B. (2021). On the structures of the ice-covered flows in a bend. *APS Division of Fluid Dynamics Meeting Abstracts*, T29–002.

Koyuncu, B., & Le, T. B. (2022). On the impacts of ice cover on flow profiles in a bend. *Water Resources Research*, *58*(9), e2021WR031742.

Koyuncu, B., & Le, T. B. (2024). Modeling shear stress distribution in ice-covered streams. *Geological Society, London, Special Publications*, *540*(1), SP540–2022.

Krishnappan, B. G. (1984). Laboratory verification of turbulent flow model. *Journal of hydraulic engineering*, *110*(4), 500–514.

Lane, S. N., Bradbrook, K., Richards, K., Biron, P., & Roy, A. (2000). Secondary circulation cells in river channel confluences: Measurement artefacts or coherent flow structures? *Hydrological processes*, *14*(11-12), 2047–2071.

Larsen, P. (1973). Hydraulic roughness of ice covers. *Journal of the Hydraulics Division*, *99*(1), 111–119.

Larsen, P. A. (1969). *Head losses caused by an ice cover on open channels*. Boston Society of Civil Engineers.

Lau, Y. L., & Krishnappan, B. G. (1981). Ice cover effects on stream flows and mixing. *Journal of the Hydraulics Division*, *107*(10), 1225–1242.

Lau, Y. L., & Krishnappan, B. G. (1985). Sediment transport under ice cover. *Journal of Hydraulic Engineering*, *111*(6), 934–950.

Lauzon, R., Piliouras, A., & Rowland, J. C. (2019a). Ice and permafrost effects on delta morphology and channel dynamics. *Geophysical Research Letters*, *46*(12), 6574–6582. https://doi.org/https://doi.org/10.1029/2019GL082792

Lauzon, R., Piliouras, A., & Rowland, J. C. (2019b). Ice and permafrost effects on delta morphology and channel dynamics. *Geophysical Research Letters*, *46*(12), 6574–6582.

Le, T. B., Khosronejad, A., Sotiropoulos, F., Bartelt, N., Woldeamlak, S., & Dewall, P. (2018). Large-eddy simulation of the mississippi river under base-flow condition: Hydrodynamics of a natural diffluence-confluence region. *Journal of Hydraulic Research*.

Le, T. B., Khosronejad, A., Sotiropoulos, F., Bartelt, N., Woldeamlak, S., & Dewall, P. (2019). Large-eddy simulation of the mississippi river under base-flow condition: Hydrodynamics of a natural diffluence-confluence region. *Journal of Hydraulic Research*, *57*(6), 836–851.

Lindenschmidt, K.-E. (2017). Rivice—a non-proprietary, open-source, one-dimensional river-ice model. *Water*, *9*(5), 314.

Longo, S., Liang, D., Chiapponi, L., & Jiménez, L. A. (2012). Turbulent flow structure in experimental laboratory wind-generated gravity waves. *Coastal Engineering*, *64*, 1–15.

López, F., & García, M. H. (1999). Wall similarity in turbulent open-channel flow. *Journal of engineering mechanics*, *125*(7), 789–796.

Lotsari, E., Dietze, M., Kämäri, M., Alho, P., & Kasvi, E. (2020). Macro-turbulent flow and its impacts on sediment transport potential of a subarctic river during ice-covered and open-channel conditions. *Water*, *12*(7), 1874.

Lotsari, E., Kasvi, E., Kämäri, M., & Alho, P. (2017). The effects of ice cover on flow characteristics in a subarctic meandering river. *Earth Surface Processes and Landforms*, *42*(8), 1195–1212.

Lotsari, E., Lintunen, K., Kasvi, E., Alho, P., & Blåfield, L. (2022). The impacts of near-bed flow characteristics on river bed sediment transport under ice-covered conditions in 2016–2021. *Journal of Hydrology*, *615*, 128610.

Lotsari, E., Tarsa, T., Kämäri, M., Alho, P., & Kasvi, E. (2019). Spatial variation of flow characteristics in a subarctic meandering river in ice-covered and open-channel conditions: A 2d hydrodynamic modelling approach. *Earth Surface Processes and Landforms*, *44*(8), 1509–1529.

Ma, R., Alamé, K., & Mahesh, K. (2021). Direct numerical simulation of turbulent channel flow over random rough surfaces. *Journal of Fluid Mechanics*, *908*.

Magnuson, J. J., Robertson, D. M., Benson, B. J., Wynne, R. H., Livingstone, D. M., Arai, T., Assel, R. A., Barry, R. G., Card, V., Kuusisto, E., et al. (2000). Historical trends in lake and river ice cover in the northern hemisphere. *Science*, *289*(5485), 1743–1746.

Marian, M., Kim, J., & Kim, D. (2021). Impact of the sampling duration on the uncertainty of averaged velocity measurements with acoustic instruments. *Hydrological Processes*, *35*(4), e14125.

Marusic, I., Monty, J. P., Hultmark, M., & Smits, A. J. (2013). On the logarithmic region in wall turbulence. *Journal of Fluid Mechanics*, *716*.

Métivier, F., Lajeunesse, E., & Devauchelle, O. (2017). Laboratory rivers: Lacey's law, threshold theory, and channel stability. *Earth Surface Dynamics*, *5*(1), 187–198.

Moradi, G., Vermeulen, B., Rennie, C. D., Cardot, R., & Lane, S. N. (2019). Evaluation of adcp processing options for secondary flow identification at river junctions. *Earth Surface Processes and Landforms*, *44*(14), 2903–2921.

Muste, M., Yu, K., Pratt, T., & Abraham, D. (2004). Practical aspects of adcp data use for quantification of mean river flow characteristics; part ii: Fixed-vessel measurements. *Flow measurement and instrumentation*, *15*(1), 17–28.

Muste, M., Yu, K., & Spasojevic, M. (2004). Practical aspects of adcp data use for quantification of mean river flow characteristics; part i: Moving-vessel measurements. *Flow measurement and instrumentation*, *15*(1), 1–16.

Nanson, G. C., & Huang, H. Q. (2017). Self-adjustment in rivers: Evidence for least action as the primary control of alluvial-channel form and process. *Earth Surface Processes and Landforms*, *42*(4), 575–594. https://doi.org/https://doi.org/10.1002/esp.3999

Neill, S. P., & Hashemi, M. R. (2018). *Fundamentals of ocean renewable energy: Generating electricity from the sea*. Academic Press.

Němec, J., & Schaake, J. (1982). Sensitivity of water resource systems to climate variation. *Hydrological Sciences Journal*, *27*(3), 327–343.

Nezu, I., Tominaga, A., & Nakagawa, H. (1993). Field measurements of secondary currents in straight rivers. *Journal of Hydraulic Engineering*, *119*(5), 598–614.

Nikora, V., Stoesser, T., Cameron, S. M., Stewart, M., Papadopoulos, K., Ouro, P., McSherry, R., Zampiron, A., Marusic, I., & Falconer, R. A. (2019). Friction factor decomposition for rough-wall flows: Theoretical background and application to open-channel flows. *Journal of Fluid Mechanics*, *872*, 626–664.

Nikora, V., & Roy, A. G. (2012). Secondary flows in rivers: Theoretical framework, recent advances, and current challenges. *Gravel bed rivers: Processes, tools, environments*, 3–22.

Parker, G. (1978). Self-formed straight rivers with equilibrium banks and mobile bed. part 1. the sand-silt river. *Journal of Fluid Mechanics*, *89*(1), 109–125.

Parker, G. (1991). Selective sorting and abrasion of river gravel. ii: Applications. *Journal of Hydraulic Engineering*, *117*(2), 150–171.

Parthasarathy, R., & Muste, M. (1994). Velocity measurements in asymmetric turbulent channel flows. *Journal of Hydraulic Engineering*, *120*(9), 1000–1020.

Peng, X., Zhang, T., Frauenfeld, O. W., Du, R., Jin, H., & Mu, C. (n.d.). A holistic assessment of 1979–2016 global cryospheric extent. *Earth's Future*, e2020EF001969.

Petit, F. (1990). Evaluation of grain shear stresses required to initiate movement of particles in natural rivers. *Earth Surface Processes and Landforms*, *15*(2), 135–148.

Petrie, J., & Diplas, P. (2016). Evaluation of the logarithmic law of the wall for river flows. *River Research and Applications*, *32*(5), 1082–1093.

Petrie, J., Diplas, P., Gutierrez, M., & Nam, S. (2013). Data evaluation for acoustic doppler current profiler measurements obtained at fixed locations in a natural river. *Water Resources Research*, *49*(2), 1003–1016.

Phillips, C. B., & Jerolmack, D. J. (2016). Self-organization of river channels as a critical filter on climate signals. *Science*, *352*(6286), 694–697. https://doi.org/10.1126/science.aad3348

PIELKE JR, R. (1999). Who decides? forecasts and responsibilities. *Applied Behavioral Science Review*, *7*(2), 83–101.

Popović, P., Devauchelle, O., Abramian, A., & Lajeunesse, E. (2021). Sediment load determines the shape of rivers. *Proceedings of the National Academy of Sciences*, *118*(49).

Prowse, T. D. (2001a). River-ice ecology. i: Hydrologic, geomorphic, and water-quality aspects. *Journal of Cold Regions Engineering*, *15*(1), 1–16.

Prowse, T. D. (2001b). River-ice ecology. ii: Biological aspects. *Journal of Cold Regions Engineering*, *15*(1), 17–33.

Prowse, T. D. (2001c). River-ice ecology. ii: Biological aspects. *Journal of Cold Regions Engineering*, *15*(1), 17–33.

Pu, J. H. (2019). Turbulent rectangular compound open channel flow study using multi-zonal approach. *Environmental Fluid Mechanics*, *19*(3), 785–800.

Robert, A., Roy, A. G., & DE SERRES, B. (1992). Changes in velocity profiles at roughness transitions in coarse grained channels. *Sedimentology*, *39*(5), 725–735.

Rodríguez, J. F., & García, M. H. (2008). Laboratory measurements of 3-d flow patterns and turbulence in straight open channel with rough bed. *Journal of Hydraulic Research*, *46*(4), 454–465.

Salinger, M. J., Basher, R., Fitzharris, B., Hay, J., Jones, P., Macveigh, J., & Schmidely-Leleu, I. (1995). Climate trends in the south-west pacific. *International Journal of Climatology*, *15*(3), 285–302.

Seizilles, G., Devauchelle, O., Lajeunesse, E., & Métivier, F. (2013). Width of laminar laboratory rivers. *Physical Review E*, *87*(5), 052204.

Seizilles, G., Lajeunesse, E., Devauchelle, O., & Bak, M. (2014). Cross-stream diffusion in bedload transport. *Physics of Fluids*, *26*(1), 013302.

Serinaldi, F., & Kilsby, C. G. (2015). Stationarity is undead: Uncertainty dominates the distribution of extremes. *Advances in Water Resources*, *77*, 17–36.

Shen, C., & Lemmin, U. (1997). A two-dimensional acoustic sediment flux profiler. *Measurement Science and Technology*, *8*(8), 880.

Shen, H. T. (2010). Mathematical modeling of river ice processes. *Cold Regions Science and Technology*, *62*(1), 3–13.

Shen, H. T., Su, J., & Liu, L. (2000). Sph simulation of river ice dynamics. *Journal of Computational Physics*, *165*(2), 752–770.

Shen, H. T., Wang, D. S., & Lal, A. W. (1995). Numerical simulation of river ice processes. *Journal of Cold Regions Engineering*, *9*(3), 107–118.

Shen, H. T., & Yapa, P. D. (1986). Flow resistance of river ice cover. *Journal of hydraulic engineering*, *112*(2), 142–156.

Shiono, K., & Knight, D. (1988). Two-dimensional analytical solution for a compound channel. *Proceedings of 3rd international symposium on refined flow modelling and turbulence measurements*, 503–510.

Shiono, K., & Knight, D. W. (1991). Turbulent open-channel flows with variable depth across the channel. *Journal of fluid mechanics*, *222*, 617–646.

Smith, B. T., & Ettema, R. (1995). *Ice-cover influence on flow and bedload transport in dune-bed channels*. Iowa Institute of Hydraulic Research, the University of Iowa.

Smith, K., Cockburn, J. M., & Villard, P. V. (2023). Rivers under ice: Evaluating simulated morphodynamics through a riffle-pool sequence. *Water*, *15*(8), 1604.

Soulsby, R. (1981). Measurements of the reynolds stress components close to a marine sand bank. *Marine Geology*, *42*(1-4), 35–47.

Stoesser, T., Ruether, N., & Olsen, N. R. B. (2010). Calculation of primary and secondary flow and boundary shear stresses in a meandering channel. *Advances in Water Resources*, *33*(2), 158–170.

Stone, M. C., & Hotchkiss, R. H. (2007). Evaluating velocity measurement techniques in shallow streams. *Journal of Hydraulic Research*, *45*(6), 752–762.

Sukhodolov, A., Thiele, M., Bungartz, H., & Engelhardt, C. (1999). Turbulence structure in an ice-covered, sand-bed river. *Water resources research*, *35*(3), 889–894.

Sukhodolov, A. N. (2012). Structure of turbulent flow in a meander bend of a lowland river. *Water Resources Research*, *48*(1).

Sun, X., & Shiono, K. (2009). Flow resistance of one-line emergent vegetation along the floodplain edge of a compound open channel. *Advances in Water Resources*, *32*(3), 430–438.

Tang, X., & Knight, D. W. (2015). The lateral distribution of depth-averaged velocity in a channel flow bend. *Journal of Hydro-Environment Research*, *9*(4), 532–541.

Tatinclaux, J.-C., & Gogus, M. (1983). Asymmetric plane flow with application to ice jams. *Journal of Hydraulic Engineering*, *109*(11), 1540–1554.

Teal, M. J., Ettema, R., & Walker, J. F. (1994). Estimation of mean flow velocity in ice-covered channels. *Journal of Hydraulic Engineering*, *120*(12), 1385–1400.

Thellman, A., Jankowski, K. J., Hayden, B., Yang, X., Dolan, W., Smits, A. P., & O'Sullivan, A. M. (2021). The ecology of river ice. *Journal of Geophysical Research: Biogeosciences*, *126*(9), e2021JG006275.

Tian, H., Yu, M., Liu, Y., Huang, Y., & Hu, P. (2021). Analytical model for lateral depth-averaged velocity distributions in curved channels. *Proceedings of the Institution of Civil Engineers-Water Management*, *174*(2), 99–108.

Tsai, W.-F., & Ettema, R. (1994a). Ice cover influence on transverse bed slopes in a curved alluvial channel. *Journal of Hydraulic Research*, *32*(4), 561–581.

Tsai, W.-F., & Ettema, R. (1996). *A study of ice-covered flow in an alluvial bend*. Iowa Institute of Hydraulic Research, College of Engineering, the University ...

Tsai, W.-F., & Ettema, R. (1994b). Modified eddy viscosity model in fully developed asymmetric channel flows. *Journal of engineering mechanics*, *120*(4), 720–732.

Turcotte, B., Morse, B., Bergeron, N. E., & Roy, A. G. (2011). Sediment transport in ice-affected rivers. *Journal of hydrology*, *409*(1-2), 561–577.

Urroz, G. E., & Ettema, R. (1994a). Application of two-layer hypothesis to fully developed flow in ice-covered curved channels. *Canadian journal of civil engineering*, *21*(1), 101–110.

Urroz, G. E., & Ettema, R. (1994b). Small-scale experiments on ice-jam initiation in a curved channel. *Canadian Journal of Civil Engineering*, *21*(5), 719–727.

Van Balen, W., Blanckaert, K., & Uijttewaal, W. S. (2010). Analysis of the role of turbulence in curved open-channel flow at different water depths by means of experiments, les and rans. *Journal of Turbulence*, (11), N12.

Van Balen, W., Uijttewaal, W. S., & Blanckaert, K. (2010). Large-eddy simulation of a curved open-channel flow over topography. *Physics of Fluids*, *22*(7), 075108.

Vionnet, C., Tassi, P., & Martín Vide, J. (2004). Estimates of flow resistance and eddy viscosity coefficients for 2d modelling on vegetated floodplains. *Hydrological processes*, *18*(15), 2907–2926.

Volino, R. J., & Schultz, M. P. (2018). Determination of wall shear stress from mean velocity and reynolds shear stress profiles. *Physical Review Fluids*, *3*(3), 034606.

Vyas, J. K., Perumal, M., & Moramarco, T. (2021). Entropy based river discharge estimation using one-point velocity measurement at 0.6 d. *Water Resources Research*, *57*(8), e2021WR029825.

Walsh, J. E., Overland, J. E., Groisman, P. Y., & Rudolf, B. (2011). Ongoing climate change in the arctic. *Ambio*, *40*(1), 6–16.

Wang, F., Huai, W., & Guo, Y. (2021). Analytical model for the suspended sediment concentration in the ice-covered alluvial channels. *Journal of Hydrology*, *597*, 126338.

Wang, F., Huai, W., Guo, Y., & Liu, M. (2021). Turbulence structure and momentum exchange in compound channel flows with shore ice covered on the floodplains. *Water Resources Research*, *57*(4), e2020WR028621.

Wang, F., Huai, W., Liu, M., & Fu, X. (2020). Modeling depth-averaged streamwise velocity in straight trapezoidal compound channels with ice cover. *Journal of Hydrology*, *585*, 124336.

Wang, J., Sui, J.-y., & Karney, B. W. (2008). Incipient motion of non-cohesive sediment under ice cover—an experimental study. *Journal of Hydrodynamics*, *20*(1), 117–124.

Wazney, L. (2019). Investigation of river ice cover formation processes at freeze-up.

Weiss, A., Clark, S. P., Rennie, C. D., Moore, S. A., & Ahmari, H. (2015). Estimation of total suspended solids concentration from adcp backscatter and hydraulic measurements. *Journal of Hydraulic Research*, *53*(5), 670–677.

Whiting, P. J., & Dietrich, W. E. (1990). Boundary shear stress and roughness over mobile alluvial beds. *Journal of Hydraulic Engineering*, *116*(12), 1495–1511.

Wilcock, P. R. (1996). Estimating local bed shear stress from velocity observations. *Water Resources Research*, *32*(11), 3361–3366.

Williams, J. J., Thorne, P. D., & Heathershaw, A. D. (1989). Measurements of turbulence in the benthic boundary layer over a gravel bed. *Sedimentology*, *36*(6), 959–971.

Wrona, F. J., Prowse, T. D., Reist, J. D., Hobbie, J. E., Lévesque, L. M., & Vincent, W. F. (2006). Climate impacts on arctic freshwater ecosystems and fisheries: Background, rationale and approach of the arctic climate impact assessment (acia). *AMBIO: A Journal of the Human Environment*, *35*(7), 326–329.

Yan, J., Tang, H.-w., Xiao, Y., Li, K.-j., & Tian, Z.-J. (2011). Experimental study on influence of boundary on location of maximum velocity in open channel flows. *Water Science and Engineering*, *4*(2), 185–191.

Yang, X., Pavelsky, T. M., & Allen, G. H. (2020). The past and future of global river ice. *Nature*, *577*(7788), 69–73.

Zhang, J., Wang, W., Li, Z., Li, Q., Zhong, Y., Xia, Z., & Qiu, H. (2021). Analytical models of velocity, reynolds stress and turbulence intensity in ice-covered channels. *Water*, *13*(8), 1107.

Zhong, Q., Chen, Q., Wang, H., Li, D., & Wang, X. (2016). Statistical analysis of turbulent super-streamwise vortices based on observations of streaky structures near the free surface in the smooth open channel flow. *Water Resources Research*, *52*(5), 3563–3578.

Zhong, Y., Huai, W., & Chen, G. (2019). Analytical model for lateral depth-averaged velocity distributions in rectangular ice-covered channels. *Journal of Hydraulic Engineering*, *145*(1), 04018080.

APPENDIX

Our theoretical model is based on the lubrication approximation (Devauchelle et al., 2022). The following assumptions were made:

- The flow is steady. Unsteady effects are not accounted for.
- No curvature effect of the channel planform is considered (e.g. straight channel only).
- The top surface is completely covered by ice. No open-surface zones are observed on the top surface.
- The effects of bedform and ice scallops are not considered in the current model. The ice surface is considered to be flat $z_{ice} = const$ and it has a grain-size roughness height of k_s (rough wall).
- The turbulent viscosity ν_t is constant along the vertical direction.
- In the case of ice-covered flow, the situation is like flow in a pipe or a closed duct. Note that there are three different pressure gradients along three directions $\frac{\partial p}{\partial x}$ (cross-stream direction), $\frac{\partial p}{\partial y}$ (stream direction), and $\frac{\partial p}{\partial z}$ (vertical direction). We ignore the cross-stream pressure gradient $\frac{\partial p}{\partial x} = 0$ as the river width ($B \approx 40\ m$) is much smaller than the river reach $L \approx 1\ km$. The pressure gradient along the y direction $\frac{\partial p}{\partial y}$ drives the flow and it is implicitly included in the flow momentum balance (Equation A.10). We assume that the pressure gradient along the vertical direction $\frac{\partial p}{\partial z}$ follows a hydrostatic pressure law since it is a valid assumption for gravity-driven flows in closed ducts and pipes (Finnemore & Franzini, 2002).

The details of the transformation for the momentum are as follows:

First, the momentum equation is written as:

$$\nu_t \left(\frac{\partial^2 u_2}{\partial^2 x} + \frac{\partial^2 u_2}{\partial^2 z} \right) + gS_f = 0 \tag{A.1}$$

The no-slip conditions on the ice-water interface and the river bed can be written as:

$$\begin{aligned} u_2 = 0 \;\; for \;\; z = 0 \;\; (ice - water \;\; interface) \\ u_2 = 0 \;\; for \;\; z = -H(x) \;\; (river\ bed) \end{aligned} \tag{A.2}$$

Ignoring the channel curvature ($\frac{\partial(.)}{\partial y} = 0$) and revoking the condition, the turbulent stresses become:

$$\tau_x = \tau_{xy} = \mu_t \left(\frac{\partial u_2}{\partial x} + \frac{\partial u_1}{\partial y} \right) = \mu_t \left(\frac{\partial u_2}{\partial x} \right)$$

$$\tau_{yy} = 0 \tag{A.3}$$

$$\tau_z = \tau_{yz} = \mu_t \left(\frac{\partial u_2}{\partial z} + \frac{\partial u_3}{\partial y} \right) = \mu_t \left(\frac{\partial u_2}{\partial z} \right)$$

Here $\mu_t = \rho \nu_t$ with ρ is water density. Now the momentum equation can be integrated along the depth in each vertical ($z = -H \rightarrow z = 0$) assuming that ν_t is invariant across the depth:

$$\nu_t \int_{z=-H}^{z=0} \frac{\partial^2 u_2}{\partial^2 x} dz + \nu_t \int_{z=-H}^{z=0} \frac{\partial^2 u_2}{\partial^2 z} dz + \int_{z=-H}^{z=0} gS_f dz = 0 \tag{A.4}$$

Note that we can calculate the first integral using the Leibniz's rule:

$$\frac{\partial}{\partial x}\left(\int_{z=-H}^{z=0}\frac{\partial u_2}{\partial x}dz\right)=\frac{\partial u_2}{\partial x}\Big|_{z=0}\frac{\partial z}{\partial x}\Big|_{z=0}+\frac{\partial u}{\partial x}\Big|_{z=-H}\left(\frac{\partial H}{\partial x}\right)_{z=-H}+\int_{z=-H}^{z=0}\frac{\partial^2 u_2}{\partial^2 x}dz$$

Here we assume that the ice-water interface is flat $\frac{\partial z_{ice}}{\partial x}\Big|_{z=0}=0$, this results in the relation:

$$\int_{z=-H}^{z=0}\frac{\partial^2 u_2}{\partial^2 x}dz=\frac{\partial}{\partial x}\left(\int_{z=-H}^{z=0}\frac{\partial u_2}{\partial x}dz\right)-\frac{\partial u_2}{\partial x}\Big|_{z=-H}\frac{\partial H}{\partial x}$$

By chain rule:

$$\frac{\partial u_2}{\partial x}\Big|_{z=-H}=\frac{\partial u_2}{\partial z}\frac{\partial z}{\partial x}\Big|_{z=-H}=-\frac{\partial u_2}{\partial z}\Big|_{z=-H}\frac{\partial H}{\partial x}$$

Therefore, the momentum equation (Equation A.4) now becomes:

$$\nu_t\left(\frac{\partial}{\partial x}\left(\int_{z=-H}^{z=0}\frac{\partial u_2}{\partial x}\right)dz-\frac{\partial u_2}{\partial z}\Big|_{z=-H}\left(\frac{\partial H}{\partial x}\right)^2\right)+\nu_t\frac{\partial u_2}{\partial z}\Big|_{z=-H}^{z=0}+gS_fH=0 \tag{A.5}$$

The depth-averaged streamwise velocity (U_2) can be computed as:

$$\int_{z=-H}^{z=0}u_2dz=U_2H$$

Now the Leibniz's rule gives:

$$\frac{\partial}{\partial x}\left(\int_{z=-H}^{z=0}u_2dz\right)=\frac{\partial}{\partial x}\left(U_2H\right)=u_2\Big|_{z=0}\frac{\partial z}{\partial x}\Big|_{z=0}+u_2\Big|_{z=-H}\frac{\partial H}{\partial x}+\int_{z=-H}^{z=0}\frac{\partial u_2}{\partial x}dz \tag{A.6}$$

Note that we invoke the flat surface condition again, $\frac{\partial z_{ice}}{\partial x}\Big|_{z=0} = 0$ and the no-slip condition $u\Big|_{z=-H} = 0$, we finally have:

$$\frac{\partial}{\partial x}\left(\int_{z=-H}^{z=0} u_2 dz\right) = \int_{z=-H}^{z=0} \frac{\partial u_2}{\partial x} dz \tag{A.7}$$

Now substitute Equation A.7 into the Equation A.5:

$$\nu_t \left(\frac{\partial}{\partial x}\left(\frac{\partial(U_2 H)}{\partial x}\right) - \frac{\partial u_2}{\partial x}\Big|_{z=-H}\left(\frac{\partial H}{\partial x}\right)^2\right) - \tau_i - \tau_b + g S_f H = 0 \tag{A.8}$$

Here we use the definition of the shear stresses on the ice (τ_i) and the bed (τ_b) surfaces:

$$\begin{aligned} \tau_i &= -\mu_t \frac{\partial u_2}{\partial z}\Big|_{z=0} \\ \tau_b &= \mu_t \frac{\partial u_2}{\partial z}\Big|_{z=-H} \end{aligned} \tag{A.9}$$

or we can write:

$$\rho \nu_t \frac{\partial^2}{\partial x^2}(U_2 H) - \tau_i - \tau_b \left(1 + \left(\frac{\partial H}{\partial x}\right)^2\right) + \rho g S_f H = 0 \tag{A.10}$$